Spring 4-21-2018

Design and Characterization of Systems for Direct Spatial Imaging of Low-Energy Gamma-Radiation Sources

Phoenix Baldez
Doctoral Student, Nuclear Engineering

Recommended Citation

Phoenix Baldez

Candidate

Nuclear Engineering

Department

This thesis is approved, and it is acceptable in quality and form for publication:

Approved by the Thesis Committee:

Adam Hecht, Chairperson

Cassiano de Oliveira

Paul DeRego

Design and Characterization of Systems for Direct Spatial Imaging of Low-Energy Gamma-Radiation Sources

By

Phoenix Baldez

Bachelor of Science – Nuclear Engineering 2015

University of New Mexico

Submitted in Partial Fulfillment of the
Requirements for the Degree of

Master of Science

Nuclear Engineering

The University of New Mexico
Albuquerque, New Mexico

May 2018

Acknowledgements

I would like to first thank my mom and dad for everything they have taught me about life and how it works. You gave me the tools and habits that I use every day. My significant other Maya, has always been loving, supportive and helpful throughout my journey, she teaches me new things and helps me become a better person every day. My roommates have been my closest friends for more years then I remember, I am thankful to have their world views and constant cynicism in my life. My work mates have all been there for me to answer my questions and offer me sound advice while helping me complete my tasks. My advisor, Dr. Hecht, always has ideas on something new to be done and willing to discuss, talk and help me when I hit a road block. A final thank you to all those not mentioned who I have met along the way for being a part of my life.

Design and Characterization of Systems for Direct Spatial Imaging of Low-Energy Gamma-Radiation Sources

By

Phoenix Baldez

B.S., Nuclear Engineering, University of New Mexico, 2015

M.S., Nuclear Engineering, University of New Mexico, 2018

Abstract

This work describes the development of radiation detection systems to identify and image special nuclear material (SNM) using low energy gamma rays. The imaging of these materials is crucial for timely, in the field responses to potential threats to national security. Using a spectroscopy system, the sources can be identified while images can be produced concurrently for the sources which are present. Two systems were designed and characterized in this study, a collimated imager which used collimation in front of a small CdTe detector, and a pixelated pinhole imager, using a pinhole mask in front of a

pixelated CZT detector. Low energy gamma rays are notoriously hard to detect and image, so differing collimation or masking schemes as well as varying imaging techniques were applied to each system. The systems were modeled using geometric and mathematical approximations, then simulated using Monte Carlo methods before finally being implemented in laboratory experiments. Varying the collimator or pinhole mask materials as well as the distance and type of radiation source, over energy ranges applicable to that of SNM, provided experimental setups that could mimic field interdiction work.

The results for both systems were images with a spatial resolution of better than 1 cm as well as energy spectra that could be used to identify the radiation source present. The collimated imager is able to detect material up to one meter distant while in a self-contained, portable enclosure. For the pinhole mask in front of the pixelated detector, using a single pinhole optimized for the pixelated detector geometry gave a high-resolution image, though poor geometric efficiency. Using the multiple pinhole mask rather than a single pinhole created several sub-images per detection run which can then be used to synthesize detailed reconstructions of the original source, with increased resolution over that of the individual sub-images. The single and multiple mask pinhole designs were compared. The multiple pinhole design had two benefits over the single pinhole, this design greatly increased the geometric efficiency and thus the total intensity on the detector, and the information contained in the full array of sub-images was also used to extract depth of field information about the radiation sources.

Table of Contents

i. List of Figures

ii. List of Tables

iii. Nomenclature

Am	Americium
Ba	Barium
CdTe	Cadmium-tellurium
Ci	Curie
Co	Colbalt
CP1	Chicago Pile-1
CZT	Cadmium-zinc-tellurium
Eu	Europium
eV	Electronvolt
FWHM	Full Width at Half Maximum
HPGe	High Purity Germanium
HEU	Highly Enriched Uranium
IAEA	International Atomic Energy Agency
MD	Mask-to-Detector Distance
MCNP	Monte Carlo N-Particle code
MLEM	Maximum Likelihood Expectation Maximization
NPT	Treaty on Non-Proliferation of Nuclear Weapons
PRF	Point Response Function
SM	Source-to-Mask Distance
SNM	Special Nuclear Material
U	Uranium
WWII	World War II

1. Introduction

1.1 History of Imaging

Imaging techniques using visible light are suspected to have been in use since 30,000BCE. The first known imager was the camera obscura, used to project images from outside onto a wall inside a dark room. A small pinhole would be created in an opaque material, allowing a very small amount of light from the outside into a darkened room. The result would be an inverted image projected on to an interior wall which could be viewed by those inside. It is proposed that some cave paintings of animals are tracings done using a camera obscura [1].

The first documented instance of a camera obscura use comes from Chinese philosopher Mo Di in the 5th century BCE [2]. However, the first documentation of the mathematical theory of a camera obscura comes from Leonardo da Vinci in 1502 in "Codex Atlanticus" where he studies the optics and function of the human eye [3]. Figure 1 shows Leonardo da Vinci's original sketches which are similar to modern day ray tracing technique used in optics.
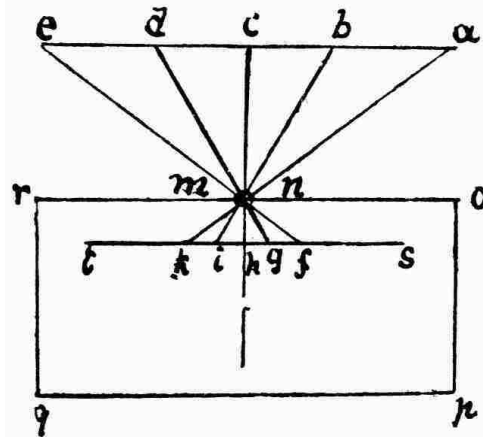
Figure 1: Leonardo da Vinci's notes on a camera obscura. [3]

Then in 1544 Gemma Frisius published the first known reference of the camera obscura in "De Radio Astronomica et Geometrica." Using a camera obscura, shown in Figure 2, he can view a solar eclipse and study it without risking damage to his eyes [4].
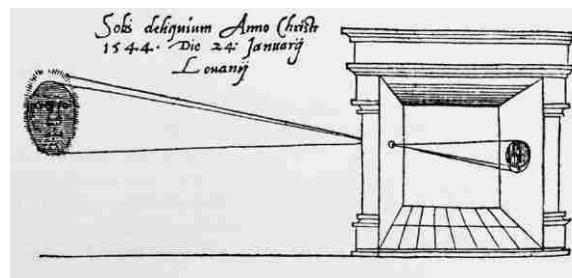
Figure 2: Gemma Frisius' use of a camera obscura to study a solar eclipse. [4]

In modern times school children often build camera obscuras out of cardboard so that they can safely view solar eclipses. Images can now be captured on a film that is the developed to produce a picture or, more commonly, it is captured digitally. A digital camera is made of up of millions of pixels which are sensitive to visible light and when exposed, capture the energy and location of the light projected onto the imaging plane to create an image [5]. This is the same concept that is used in this research, but for gamma ray imaging.

1.2 History of Non-Proliferation Efforts

We have performed research in direct gamma ray imaging in support of nuclear nonproliferation, with special emphasis on low energy gamma rays from special nuclear materials - a subset of actinides that can fission from neutron interactions. The need for this work is set in historical context in the sections that follow.

In 1938 the first artificial fission reaction was sustained by Otto Hahn and Fritz Strassmann at the Kaiser Wilhelm Institute for chemistry. They noticed that when Uranium was exposed to neutrons that it would transmute to lighter elements. The data was sent to Lise Meitner and Otto Frisch who interpreted the results and created a model for the fission process [6]. Over the next four years some of the most intelligent physicists in the world work on fission theory and experimentation, culminating in 1942 when Chicago Pile-1 (CP1) is brought online as the world's first nuclear reactor. Directly after the proof of concept which CP1 provided, the United States government began the Manhattan Project to develop the first atomic bomb [7].

The use of the atomic bomb by the United States against Japan at the end of World War II on both August 6th and August 9th of 1945 proved the destructive capability of such weapons to the entire world. There were multiple unsuccessful attempts to create an international agency which would control nuclear technologies in years after WWII [8, 9, 10]. A limited attempt at nuclear regulation came in the form of the International Atomic Energy Agency (IAEA) formed in 1957. The IAEA could administer safeguards but only in very limited circumstances [11].

In 1968 the Treaty on Non-Proliferation of Nuclear Weapons (NPT) was created with the purpose of preventing the spread of nuclear weapons and to promote the peaceful use of nuclear energy. The end goal of the NPT is the complete nuclear disarmament of all countries. The NPT made the allowance for five nuclear states: the United States, the United Kingdom, France, the Soviet Union and China. All other countries that signed, in doing so, were forfeiting the right to pursue nuclear weapons technology [12]. Since it's signing in 1970 the NPT has not been signed by four countries and one country has withdrawn. Figure 3 shows the current state of the world in relation to the NPT.
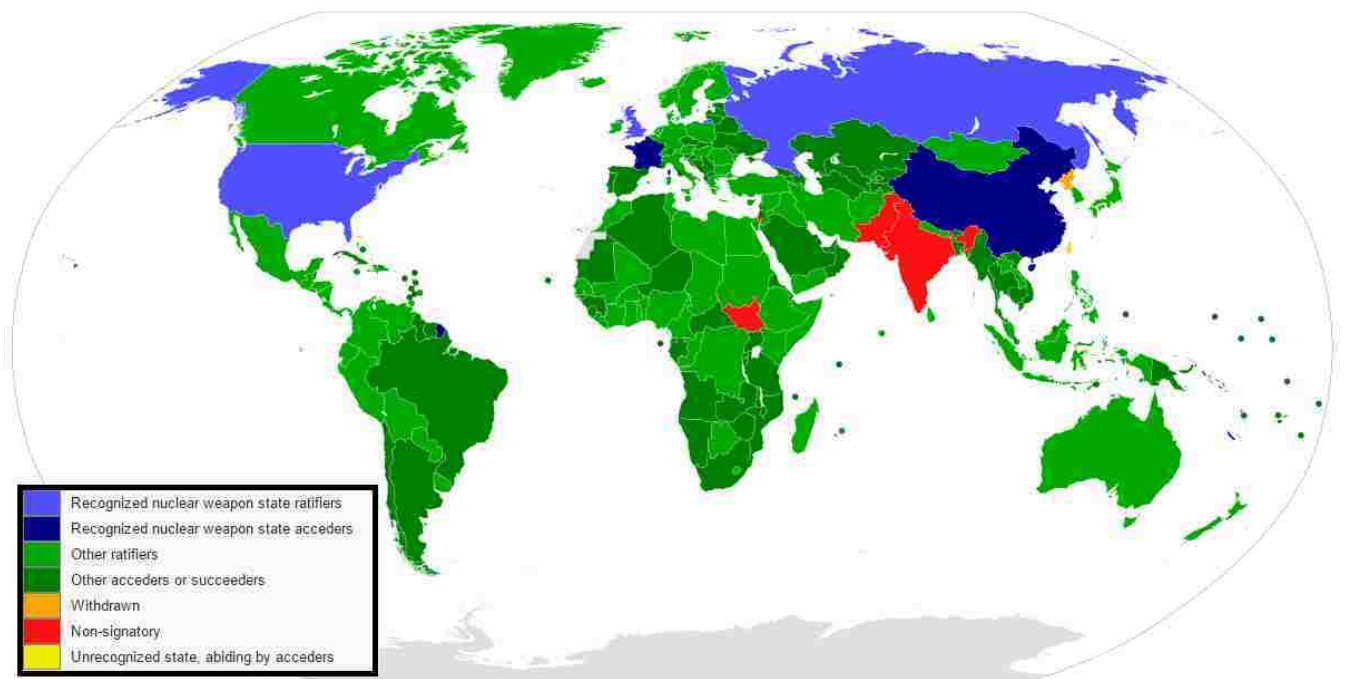
Figure 3: The Current state of the world with regard to participation in the NPT. [13]

1.3 Detection and Imaging of Special Nuclear Material

The Atomic Energy Act of 1954 defined special nuclear material (SNM) as plutonium, uranium-233, or uranium enriched in the isotopes uranium-233 or uranium-

235 [14]. Detecting and apprehending SNM that is might be used for nefarious purposes is of utmost importance for the national security of the United States. This must be able to be done in uncontrolled situations where the smuggling of SNM might take place. However, it was famously stated by Dr. Robert Oppenheimer, one of the lead scientists on the Manhattan Project, that a screwdriver would be the most useful tool in detecting SNM in baggage [15]. This is because SNM gives off very low energy decay radiation which is easily shielded by most materials.

Due to the low energy decay radiation of SNM other means have been implemented to deal with this problem. Active interrogation with neutrons to determine if a material is SNM is a commonly used method. Gamma ray interrogation is used as well but is relatively ineffective when the material is shielded. Gamma ray shielding material often has a small neutron cross section, thus making neutrons useful to probe the material in question. SNM will undergo fission or excitement when exposed to a neutron beam. Both fission and nuclear excitement have very distinctive neutron and gamma ray signatures which can then be detected [16]. Gamma ray signatures are often shielded by the same materials which makes decay radiation hard to detect. With active interrogation imaging using neutron sources, must be used and very precise geometrical measurements of the container and surrounding area must be made to correctly identify the material. Neutron detectors capable of this type of measurement are usually not portable or easy to setup. The use of a neutron source risks dosing those near the interrogation. Overall this method, while accurate, is not a viable method for in the field identification and imaging of SNM [17].

Passive radiation detection of SNM using gamma rays may be the method of choice in field situations with multiple unknowns. Gamma ray detectors can be very small and even battery powered. The problem of gamma ray shielding is still a large factor in the detection and imaging of materials, but it is possible given adequate signal to noise ratios by extended counting time and background characterizations [18]. Perhaps more importantly, if nothing is known about a radioactive package, there is the risk of booby-trapping and triggering from using active interrogation techniques, and so passive detection and imaging techniques are a prudent first step.

The Imaging of SNM in the field gives first responders a better idea of how to react to a situation. SNM that is dispersed evenly throughout a container is most likely in a powder form and must be handled differently than pucks or sphere of SNM. Knowing how to respond to a specific situation involving SNM could be the difference that saves lives.

1.4 Overview of Work

In Chapter 2 of this paper we will cover the theory behind the experiments which are described. Section 2.1 covers gamma ray spectroscopy, radioactive decay and the way that gamma rays interact with matter. The detectors used in our experiments will be described and discussed in Section 2.2. Since background radiation plays a large role in gamma ray detection, specifically in the detection of low energy gamma rays Section 2.3 is a discussion on the sources of background and how they are dealt with in our experiments. The final part of the theory, in Section 2.4, is the theory of imaging. There will be discussion of the various types of imaging and why direct imaging was chosen

6

and then how the images are obtained and reconstructed using a specific method which allows us to obtain reconstructed images of the source with sharper resolution and greater intensity while allowing depth of field analysis on the imaged sources.

The nozzle collimated imager will be covered in Chapter 3 and is the first iteration of the imaging system. It is designed to use a single crystal detector with a nozzle for collimation, with an actuator that is programmable to scan an area and generate an image. In Sections 3.1 and 3.2 we will discuss the design and modeling of the system and how it meets the given requirements. This was done with MATLAB and MCNP as well applying basic geometric models to assess the validity of the results. Then we show the experimental methodology used to characterize the system and produce data in Section 3.3. Varying locations and amounts of shielding along with one-dimensional scans of sources were done. The results of the system, in terms two-dimensional image production and energy discrimination will be shown in Section 3.4. What was learned from the design, experiments and results from this detection system will be reviewed in Section 3.5.

The next iteration of the imaging system is the pixelated detector, used for pinhole imaging. In Chapter 4 the design fundamentals of a pinhole imaging system along with the validation of mathematical predictions as well as detector responses are covered. Section 4.1 discusses the design parameters that are necessary to consider when developing a pinhole imaging system. This section introduces the basic governing equations and how they can be applied to this system to obtain the results we want. The validation of our theories is presented in Section 4.2 while using the previous nozzle collimated imaging system to predict the response of a pixelated detector. The detector is

then characterized in terms of the spectra produced by each pixel, the total detector response and the application of spectral energy discrimination in Section 4.3. The applications of the work done in theory validation and detector characterization are discussed in Section 3.5.

Chapter 5 presents the culmination of the detector system for this work. The masks, as well as the results from the single and multiple pinhole imaging experiments are described. Section 5.1 gives an overview of the masks used and applications of each mask. The first results, shown in section 5.2, were from the single pinhole masks that produced large, highly detailed images but suffered from lack of efficiency and individual pixel responses which varied widely. Section 5.3 covers the wide range of applications of multiple pinhole masks. Pinhole masks with a 2x2 as well as 4x4 layout were used to varying amounts of success. Then the effect of sub-image distance on the resolution of reconstructed images is explored. This finally results in the application of multiple pinhole imaging in depth of field measurements. The results of these experiments are summarized and discussed in section 3.5.

In Chapter 6 a summary of all the results from the development of these systems is presented. The evolution from of a single crystal, moveable, nozzle collimated imager into a large area pixelated pinhole imager with the ability to do depth of field analysis on sources is shown. Then in Chapter 7 ideas for future work is discussed. This covers the ever present need for more data, the automation of certain image reconstruction algorithms, applications of new reconstruction algorithms and the idea to quantify the objects being represented in the images produced.

2. Theory

2.1 Gamma ray Spectroscopy

Gamma rays are electromagnetic radiation with typical wavelengths on the order of tens of picometers (10^{-12} m) and frequencies above exahertz (10^{18} /sec), or an energy range of a few 10s of keV to a few MeV. Gamma rays are distinct from x-rays in that they originate in the atomic nucleus rather than with electrons. This imaging is not meant to exclude x-rays, but the term gamma ray is used here inclusive of all electromagnetic radiation in the relevant energy range.

Gamma ray spectroscopy is the study of the gamma ray energy spectrum of energies of gamma emitting materials [19]. Radiation detectors absorb radiation and in response electrons are freed from atomic bonds in proportion to the energy of the incident radiation. In solid state detectors, these free electrons then induce pulses on an anode due their motion to an electric field applied to the material, and likewise for holes moving towards cathodes. In a good detector, the pulse heights are proportional to the energy deposited from the radiation. The pulses are then binned into channels depending on how large they are. This is the process of producing a spectrum, which can then be used to identify a source based on its characteristic energies. Figure 4 shows a gamma ray spectrum of uranium oxide including some of the peaks of interest for SNM.
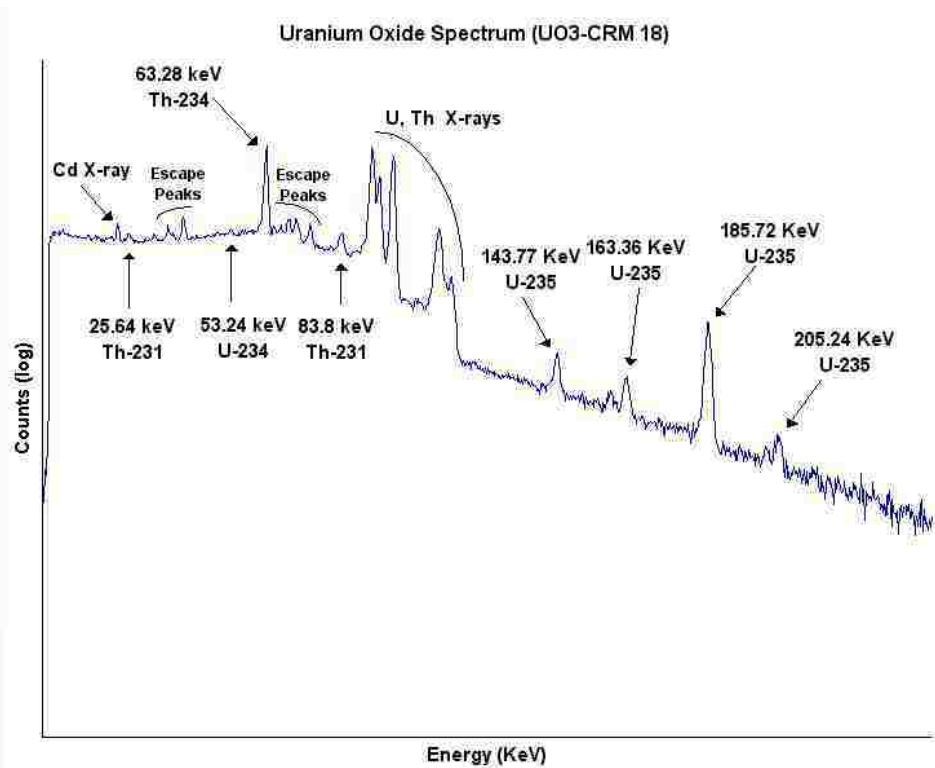
Figure 4: Gamma ray spectrum of uranium oxide showing U-235 and contaminants such as Th-231. [20]

2.1.1 Radioactive Decay

The gamma rays that are used to detect and identify material come from radioactive decay that involves the de-excitation of an atomic nucleus. The energy released is equal to the energy difference between the two energy states [21], which are then characteristic of the levels of different nuclides and can be used to identify those nuclides. The rate at which a nuclide decays is described by its half-life, the amount of time it takes for half of the nuclide to decay away. The shorter the half-life the greater the activity or number of decays that happen per unit time per number of atoms. A common problem with detecting special nuclear material is that they have very long half-lives and there for low specific activity - the activity per gram - associated with it. Specific activity is measured in number of decays from a nuclide per unit time per unit mass. Using uranium for example, U-235 and U-238 have half-lives of about 704 million years (a

specific activity of 79 thousand decays per second per gram) and 4.5 billion years (a

specific activity of 12 thousand decays per second per gram), respectively. Tables 1 and 2

show the excepted number of gamma rays observed at different energies in one gram of

natural uranium (99.3% U-238, 0.7% U-235) and one gram of highly enriched uranium

(HEU)(80% U-238, 20% U-235).

Energy (keV)	γps/gm U	Isotope
63.3	598	^{234}Th
83.3	10	^{234}Th
90.0	21	^{235}U (Th X-ray)
92.4	349	^{234}Th
92.8	349	^{234}Th
93.4	34	^{235}U (Th X-ray)
94.7	18	^{234m}Pa (U X-ray)
98.4	29	^{234m}Pa (U X-ray)
105.0	16	^{235}U (Th X-ray)
109.2	9	^{235}U (Th X-ray)
111.0	13	^{234m}Pa (U X-ray)
112.8	35	^{234}Th
143.8	63	^{235}U
163.3	29	^{235}U
185.7	330	^{235}U
205.3	29	^{235}U

Table 1: Number of gamma rays released per second at most probable energies for one gram of natural uranium. [22]

Energy (keV)	γps/gm ^{235}U	Isotope	Energy	γps/gm ^{238}U	Isotope
90.0	2853	^{235}U	63.3	598	^{234}Th
93.4	4656	^{235}U	83.3	10	^{234}Th
105.0	2156	^{235}U	92.4	349	^{234}Th
109.2	1234	^{235}U	92.8	349	^{234}Th
143.8	8783	^{235}U	94.7	18	^{234m}Pa
163.3	4071	^{235}U	98.4	29	^{234m}Pa
185.7	45,324	^{235}U	111.0	13	^{234m}Pa
205.3	4015	^{235}U	112.8	35	^{234}Th

Table 2: Number of gamma rays released per second at most probable energies for one gram of HEU. [22]

To put those numbers into context a commonly used source for laboratory experiments is Co-57. It has a half-life of 271 days has a specific activity of 311 trillion decays per second per gram [23].
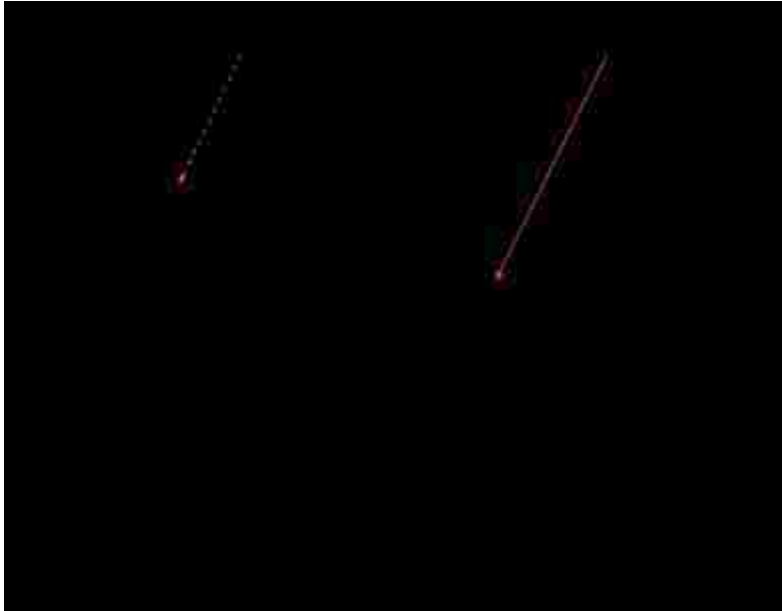
An example decay scheme for Cobalt-57 is shown in Figure 5. This figure shows that Co-57, with a half-life of 271.8 days, decays to Fe-57 by electron capture (*e*) to different energy levels with 99.8% of the decay to the 136 keV level (right) and the other 0.2% to the 707 keV level (left). This results in an excited state of Fe-57 where the most probable outcome, at 85.6% of all decays, is the release of a 122 keV gamma ray, which may be followed by a 14 keV gamma ray (9.16% of all decays) to reach the stable ground state of Fe-57. In about 10.68% of all decays the 136 keV level of Fe-57 will decay directly to the ground state, releasing a 136 keV gamma ray [24].

The two gamma rays of 122 keV and 136 keV can be used to identify Co-57 fairly simply. Even though there are other radionuclides which can emit gamma rays with

12

energy near 122 keV or near 136 keV, both the coexistence and the known ratio of these

two spectral lines is very characteristic of Co-57: While looking at an energy spectrum

that includes Co-57 there should be a large peak at 122 keV and the 136 keV peak should

be about 1/8 the size. Figure 6 shows an example of a Co-57 spectrum with this feature.

Another feature shown in Figure 6 is the characteristic x-ray of Co-57 at 7 keV. A

characteristic x-ray is released when an inner shell electron leaves a vacancy which is

then filled by an outer shell electron. Since electrons in an atom can only exist at specific

energies, the transition from outer shell to inner shell by an electron is accompanied by a

release of energy in the form of an x-ray. The energy difference between each electron

level is characteristic for every element, so the x-ray released is known as a characteristic

x-ray.
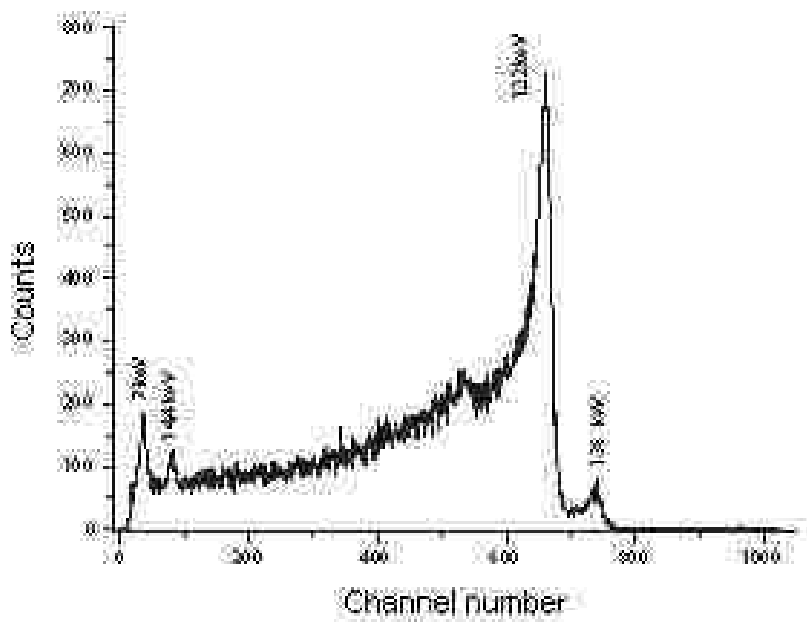
Figure 6: Co-57 spectra. [25]

13

2.1.2 Gamma ray Interactions with Matter

Gamma rays can interact with matter in a variety of ways but only three interaction processes have meaningful impact on gamma ray detection. These are: photoelectric absorption, Compton scattering, and pair production. The energy of the interacting gamma ray as well as the atomic number of the matter it is interacting with determines the probability of each of these modes. The probability of interaction with a certain material can be described by the mass attenuation coefficient which is dependent on the gamma ray energy and material characteristics - predominately electron density, with some effect from the shells the electrons are in. The overall mass attenuation coefficient is made up of attenuation contributions by the different processes by which a gamma ray can interact, for the purpose of this investigation it can be described by Equation 1. Figure 7 shows a graph relating material atomic number (Z), which describes the number of electrons in a neutral atom, with gamma ray energy and the interaction process which dominates.

$$\left(\mu/\rho\right)_{total} = \left(\mu/\rho\right)_{pp} + \left(\mu/\rho\right)_{cs} + \left(\mu/\rho\right)_{pe} \qquad (1)$$
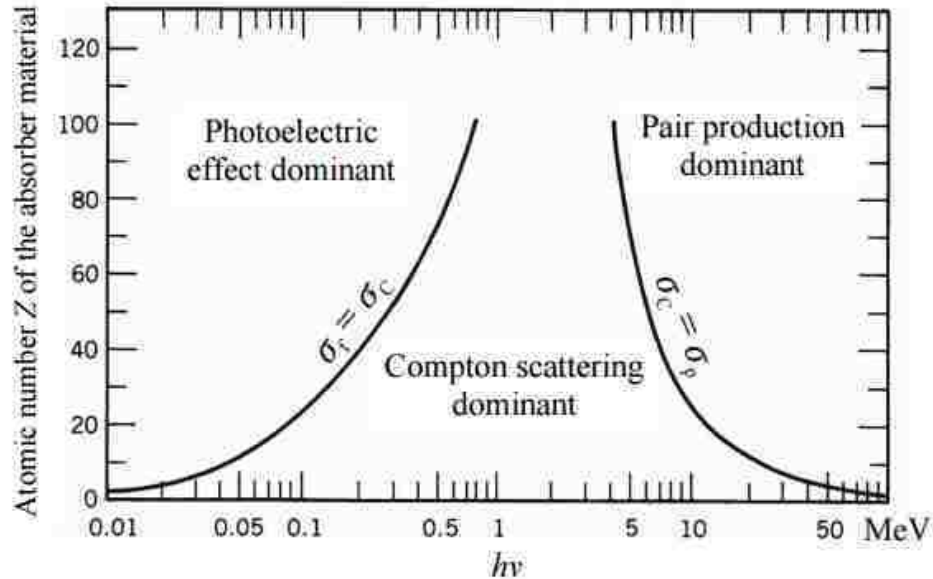
Figure 7: Gamma ray interaction processes as a function of energy and material atomic number. [26]

Pair production requires relatively high energy gamma rays to be the dominant interaction process, this makes it unlikely when using passive detection for SNM due to the low energy gamma rays which are produced by its radioactive decay. However active interrogation of SNM often deals with pair production processes during detection [27]. Pair production is the creation of an electron/positron pair purely from the energy of a gamma ray interacting with the material. There is a threshold energy of 1.022 MeV (or the mass of an electron/positron pair) for pair production to take place, any additional energy that the incident photon provides goes into kinetic energy of the two particles. Pair production can result in certain features during spectroscopic analysis such as single and double escape peaks. These escape peaks occur when the energy of the one or both of the gamma rays, resulting from the annihilation of the positron, escape the detector. A single escape peak will be 0.511 MeV below the incident photon energy peak and a double escape peak will be 1.022 MeV below the incident energy. The functional dependence of gamma ray attenuation that occurs due to pair production on material Z

15

and A as well as gamma ray energy (E) is described in Equation 2, where A is the atomic

mass.

$$({}^{\mu}/_{\rho})_{pp} \propto \frac{Z}{A} * \ln(E) \tag{2}$$

Compton scatter, shown in Figure 8, is when a gamma ray incident on material

interacts with electrons and scatters a photon and the electron. The initial gamma ray (E_γ)

imparts some energy to the photon and scatters off at a new angle (Θ) and energy ($E_\gamma{}'$)

while the electron is ejected with the imparted kinetic energy at another angle (θ).
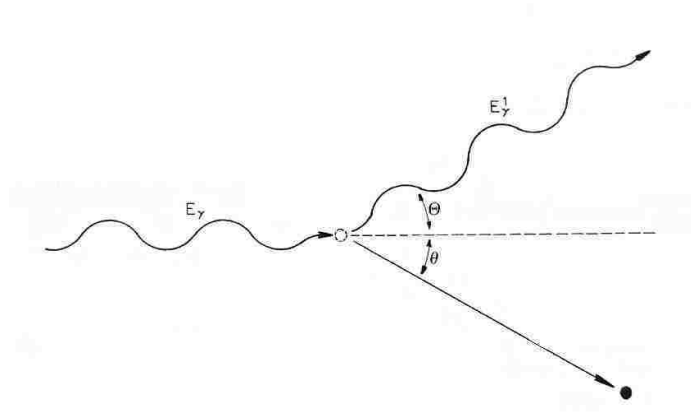
Figure 8: Representation of Compton scattering. [28]

The energy transferred in Compton scatter changes as a function of the scattering angle

and can be described by Equation 3 where mc^2 is the mass of an electron times c^2 (0.511

MeV).

$$E\gamma' = \frac{E\gamma}{1+\frac{E\gamma}{mc^2}(1-cos\Theta)} \tag{3}$$

Since the energy of the resulting scattered photon varies depending on the angle of

scatter, the energy that might be deposited in a detector can vary. The difference between

the incident and the scattered photon energy is the energy deposited in the material, E =

E_γ - E_γ'.   This leads to the Compton continuum which is a distinctive shape in the

recorded energy spectrum, shown in Figure 9. The maximum energy the photon can

deposit in a single Compton scatter - the right-hand side of the Compton continuum,

labeled as the Compton edge, is lower than the energy of the incident photon by a

quantity (labeled E_c) that depends on the incident gamma ray energy. If the gamma ray

energy is large enough this separation trends towards a constant value of 0.256 MeV [28].
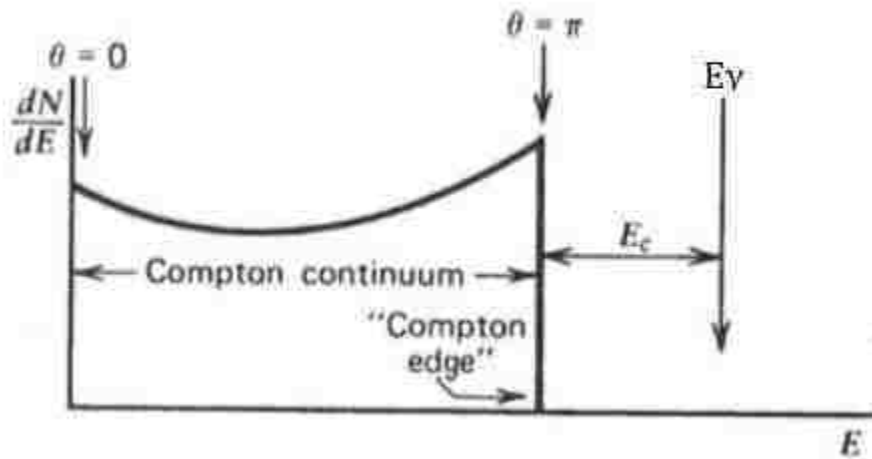
Figure 9: The Compton continuum. [28]

Compton scatter is not a major contributor to low energy gamma ray interactions, as it

dominates on the order of MeV [29]. This is shown in Equation 4 which describes the

how the probability of a gamma ray interaction due to Compton scatter changes with

material Z and A along with gamma ray energy.

$$\left(\mu/\rho\right)_{cs} \propto \frac{Z}{A} * \frac{1}{E} \tag{4}$$

The process that dominates for lower energy gamma rays, and typically x-rays

due to their low energy range, is photoelectric absorption. This is the process of the total

absorption of an incident gamma ray and the ejection of a photoelectron. The energy of

the photoelectron (E_{e^-}) is simply described by Equation 5 where E_b is the binding energy of the electron and E_γ is the energy of the gamma ray.

$$E_{e^-} = E_\gamma - E_b \qquad (5)$$

The binding energy of electrons is on the order of eV, so E_b becomes a negligible value in the spectroscopic analysis of SNM which deals with tens or hundreds of keV. As an electron is ejected, this often leads to the rearrangement of electrons in the atom, characteristic x-rays can be released as well. Apart from the characteristic x-ray release there are no additional spectroscopic peaks or shapes, such as the Compton continuum. Electrons have a very short mean free path in most detector materials the full energy peak is usually seen [30]. Equation 6 shows how photoelectric effect interactions are proportional on material Z while inversely proportional to gamma ray energy (E).

$$({}^\mu/_\rho)_{pe} \propto \frac{Z^4}{E^{3.5}} \qquad (6)$$

2.2 Detectors

There are many types of radiation detectors, each with separate applications. These applications range from detecting different types of radiation, different energy levels and suitable for different detection environments. The applications of this project, as mentioned before are the portable detection systems for low energy gamma rays and the identification of the radionuclides in a material. These constraints lead to the choice of semiconductor radiation detectors.

2.2.1 Semiconductor Radiation Detectors

Semiconductor radiation detectors utilize the crystal lattices and electron and hole pair properties of certain semiconductor materials to detect radiation. Semiconductors operate through electron excitation from a material's valance band to its conduction band. The electrons leave behind holes in the lattice formation of the semiconductor, which allows positive charge to move in the valance band [31].

The energy difference between top of the valance band and the bottom of the conduction band is known as the band gap. Band gap energies in semiconductors are on the order of eV, or fractions of eV, which are often low enough such that room temperature can give electrons sufficient energy to overcome the band gap and transfer from the valence band to the conduction band. Some semiconductors radiation detectors need to be cooled, most notably high purity germanium (HPGe) detectors, so that an excess of electrons are not promoted to the conduction band just due to thermal effects. Other detectors can operate at room temperature, such as CdTe and CdZnTe (CZT) due to their larger band gaps, approximately 1.6 eV. Impinging radiation, such as gamma rays, provides the necessary energy for the electrons to overcome the band gap and excite several electrons into the conduction band. The larger the energy of the incident gamma ray, the more electrons are promoted. The energy absorbed can go to different effects in the material, such as heating, and so the average energy per electron promoted across the band gap is typically about three times the band gap energy. By symmetry this is likewise true for holes as well.

Once in the conduction band, electrons are no longer bound to a single atom and are free to move. If the electrons are under the influence of an electric field, which is how

semiconductor radiation detectors are operated, they will begin to move in a opposite the field direction, and vice versa for holes. These electrons/holes then induce a pulse in the detector electrodes, with the pulse size directly related to the number of electrons/holes transferred to the conduction/valence band as well as the charge carrier mobility and lifetime, and therefore the energy of incident gamma ray. In Figure 10 the process of electron and hole flow in a semiconductor is shown.
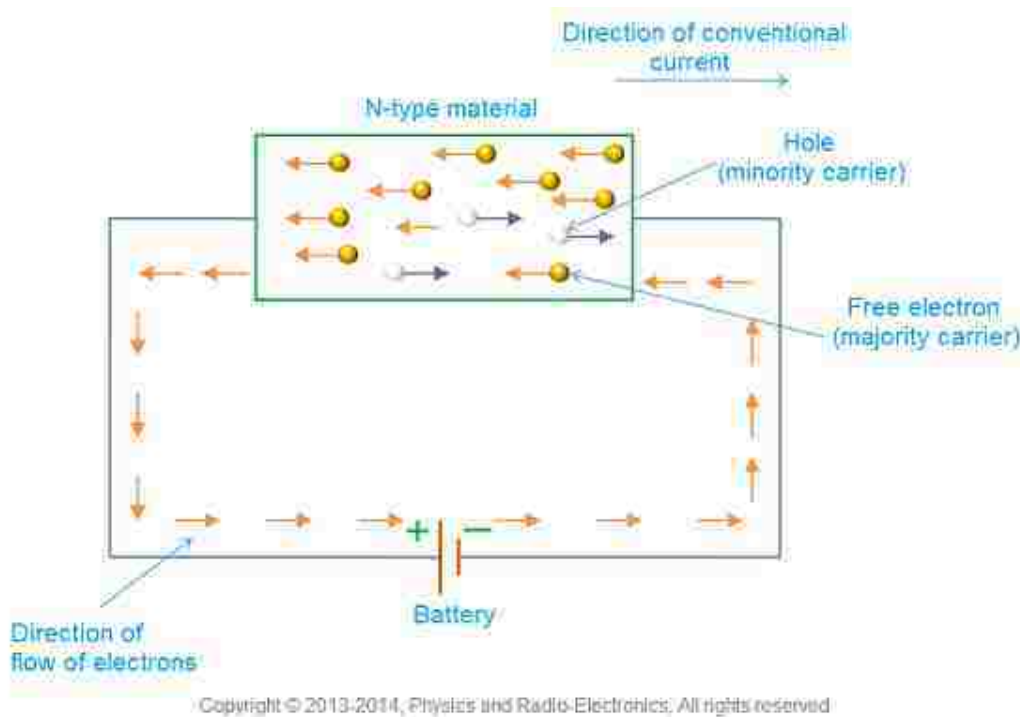
Figure 10: Diagram showing the movement of electrons and hole under the influence of an external current. [32]

2.3 Background Radiation

The gamma rays coming from SNM usually range to about 200 keV, it is rare for there to be large numbers of gamma rays with an energy higher than 600 keV. The most common gamma ray energies are usually near the low end of the energy spectrum [17]. Unfortunately, most naturally occurring background is in the same range, making SNM

even harder to detect. For this reason, the background must be understood, and background subtraction implemented.

2.3.1 Environmental Background

When creating a portable radiation detection system, it is important to recognize the environment in which that detection will take place. Differing environments and locations might pose additional constraints on the detection of SNM due to low activity and energy of emitted radiation.

Background refers to the levels of radiation in the environment at all time as well as radiation which might be present but is not of interest in the study. Sources of background are the ambient environment, building materials, cosmic rays, activation and characteristic x-rays. Figure 11 is a gamma ray spectrum of naturally occurring limestone, note the large number of counts in the lower energies not associated with a particular spectral line.
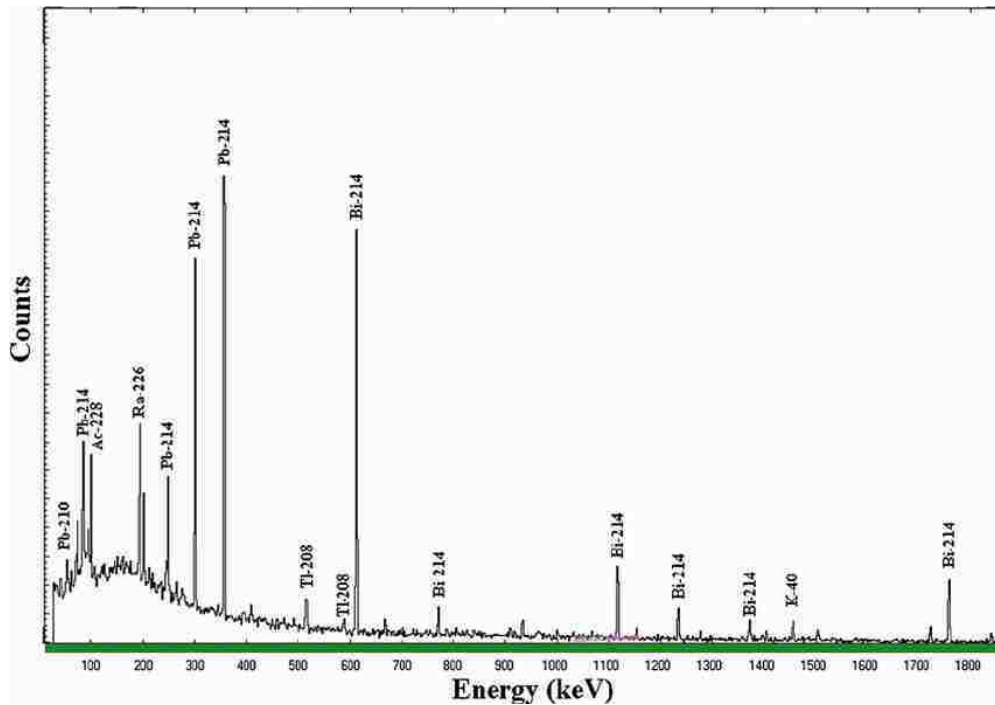
Figure 11: Gamma ray spectrum of naturally occurring limestone [33].

Ambient radiation in the environment can have many sources which change with location. These sources can be broken into terrestrial and space radiation. Terrestrial radiation can come from ultra-long-lived radionuclides, called primordial radionuclides, which were first created billions of years ago along with the Earth. It can also come from human activity such as nuclear weapons testing or nuclear accidents, the majority of which happened many decades ago but still influence increasing environmental radiation. An example of terrestrial radiation levels across North America can be seen in Figure 12.
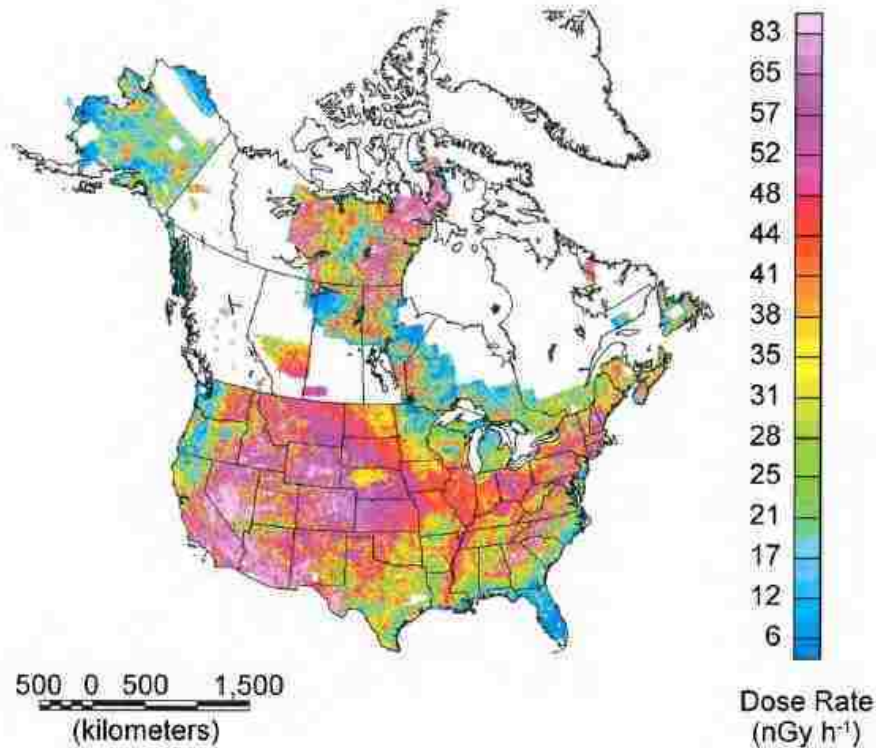
Figure 12: Terrestrial radiation across North America. [39]

The terrestrial radiation dose is highly dependent on the geology of the area due to variation in the presence of primordial radionuclides in the surrounding rocks. Space radiation mostly refers to cosmic rays, which are charged particles accelerated by the magnetic fields of the sun, the earth or possibly cataclysmic galactic events, which then pass into the atmosphere. In the atmosphere they can sometimes be directly detected at high elevations. Oftentimes these particles interact with the atmosphere itself and create a cascade of other particles which can be detected at ground level. This can lead to the activation of naturally occurring elements and result in radionuclides such as the creation of tritium, Be-7, C-14 and Na-22. The amount of radiation seen from space is directly proportional to the elevation of the location, this can be seen in Figure 13.
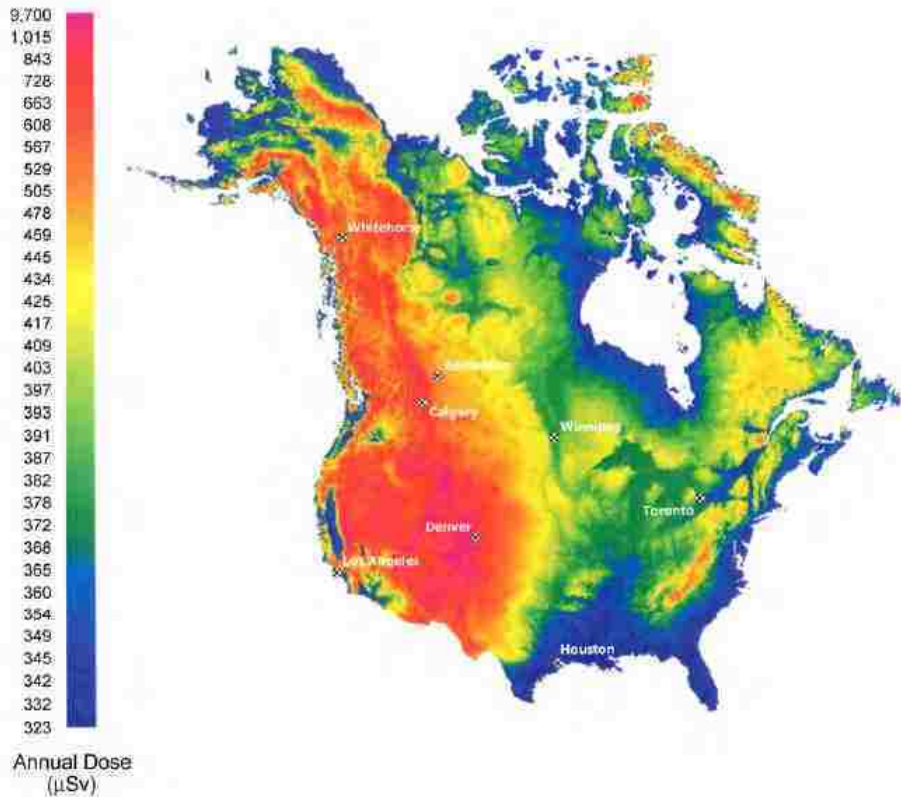
Figure 13: Cosmic ray radiation dose across North America. [39]

Background radiation can also come from materials which are not normally radioactive. When dealing with low energy gamma rays, the most common occurrence of this is the creation of characteristic x-rays. The creation of characteristic x-rays is described previously in the radioactive decay section. The example given was of a common, low energy for a characteristic x-ray. Characteristic x-rays can be created which are higher than the nuclear decay radiation generated by the atom. This is sometimes the case for SNM: Uranium and its decay products have characteristic x-rays that are emitted from 90-110 keV [22]. This is not particularly problematic for the detection and identification of SNM because it gives more spectral lines by which it can be identified. It is problematic when characteristic x-rays from other material are in the energy range of interest. Bismuth, lead, thallium, mercury and gold can all emit x-rays very near energies

24

of interest for the detection of SNM. In this case lead poses the largest problem because lead is a great shield of low energy gamma rays but if it is also producing gamma rays then its usefulness is marginalized. Figure 14 shows a spectrum of lead's characteristic x-rays.
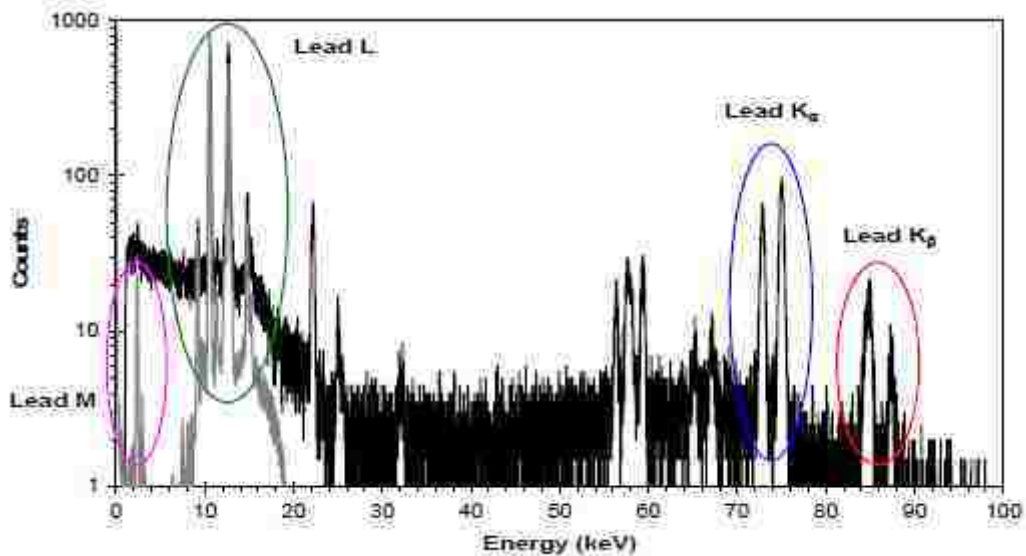
Figure 14: Characteristic x-rays of lead. [40]

However, this effect can be mitigated with shielding. If a layer of copper is placed between any lead and the radiation detector then the lead x-rays will be attenuated and any characteristic x-rays that do appear will be that of copper's. Copper's characteristic x-rays are on the order of 1 to 8 keV, well below the energies of interest for SNM [40].

2.3.2 Signal to Noise

When imaging radioactive material, the background levels must be considered. Sufficiently weak signals from the source of interest can be lost in the background radiation, so there is always some minimum detectable activity (MDA) of a radioactive source. There was no universally accepted MDA calculation until L.A. Currie published

Limits for Qualitative Detection and Quantification Determination, it is now the bench mark for MDA [40]. In his paper Currie chose a probability of detection of 95% to be an acceptable value. This value is still commonly used today in experimental work; however, different application might demand higher probabilities of detection. For every measurement there will be a number of background counts (N_B) taken while not in the presence of the source of interest. When in the presence of the source of interest the number of counts (N_T) will be collected. The difference between these two values (N_s) is defined as the number of counts emitted by the source. Then a value must be defined for that proves that N_s meets the 95% probability of detection. Assuming Gaussian distributions we can summarize this in Equation 7 for the number of counts required for detection (N_D):

$$N_D = 4.65 * \sqrt{N_B} + 2.71 \qquad\qquad (7)$$

For example, if a background of 100 counts is measured then a total number of counts N_T of 150, so a source count N_s of 50, is required for 95% confidence that a source is present.

2.3.3 Background Subtraction

The correct identification of radiation sources is of utmost importance, so therefore the data collected must be processed in way to allow for higher levels of confidence in detection and identification. Background subtraction is the process of removing radiation signals which were not generated by sources of interest. As mentioned before SNM has mostly low energy gamma ray energies where background radiation is high, so subtraction is a useful tool to make signals clearer.

Beyond actual radiation events there are the electronics themselves which introduce a noise in the output signals of every radiation detector. Since detectors are only measuring electronic signals it is possible for extraneous signals to be produced by electronic noise. This can come from the detector or the power source, every component has electronic losses, reflections etc. which can lead to signals being seen which are not actual radiation events, or actual events being lost. Electronic noise also happens to mostly accrue at lower energies simply because smaller electronic jitter is harder to fix than large noise signals. There are multiple methods for subtracting the background radiation signal and only those that were implemented in this project will be discussed here.

Before sources are introduced in the experiments, measurements were taken without the source to get a background level. This provides a baseline for the radiation levels that will be seen in every measurement after, so to the first order it can therefore just be subtracted out of every following experiment. In general, things may change about the experimental parameters such as detector voltage, orientation and materials, and with each change there must be a new background taken. Once a background is obtained for the given experimental parameters that background spectrum can then simply be subtracted out once from the spectrum with actual signal. In the region of the full energy peak, the background counts in each channel are subtracted out of each channel of the experimental results leaving only the peak. In the experiments described in this thesis, this process of background subtraction will be referred to as "method one."

Even after a background subtraction has been performed, there are often still some unwanted signals which might interfere. This is because, of course, the introduction

of a source is a very large experimental parameter that has changed. Signals outside of the energy peak can then appear in a spectrum even after with background subtraction, and these signals may be due to the source. A common feature is the Compton continuum, shown in Figure 9, in which a single high energy line from a source can cause a low energy plateau. The energy range of SNM is outside the energy range where the Compton interaction dominates so it is not a problem in these experiments.

To understand the number of counts in the full energy peak without contributions from noise, an option is peak finding followed by energy discrimination and trapezoidal background subtraction. This process is described in figures 15 and 16, the letters corresponding to step described here: (A) The range to look for certain peaks should be known from energy calibrations and expected source energies. (B) Energy peaks can be identified simply by being the maximum value in a certain range. The maximum value is close to the centroid of the peak, which is sufficient for our algorithm. (C) The energy width of a full energy peak is a constant due to detector material at a particular energy, so once the peak value is known the total number of counts in that peak can be calculated simply by summing all counts in the peak over a given width. (D) Next the background on both the high and low side of the peak needs to be calculated, to be used to subtract the background from the peak region. The background is usually higher on the low energy side of the peak due scatter down and low energy noise, but this inequality makes it so that both low and high background must be calculated differently. In this case the average of a statistically sound number of background channels is calculated. Now with the information from (C) and (D) the information needed to construct a trapezoidal area

of background is known and that background fit (E) is subtracted from the total counts in the peak range to extract the number of counts in the peak.
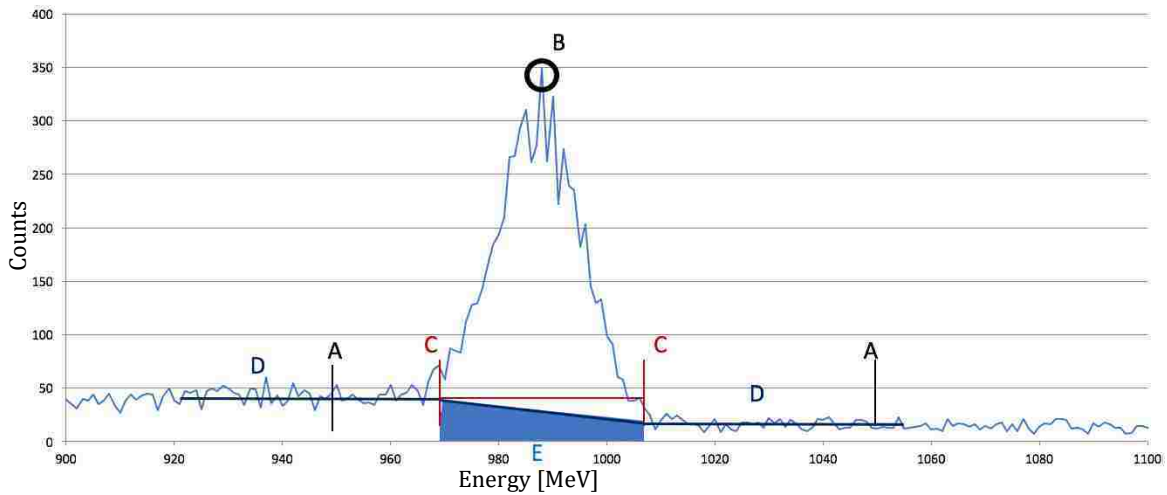
Figure 15: Steps of trapezoidal background subtraction.

When this same process is repeated with no peak present it brings peak counts, the total minus background over the range, down to single digits positive or negative which is within uncertainty, shown in Figure 16.
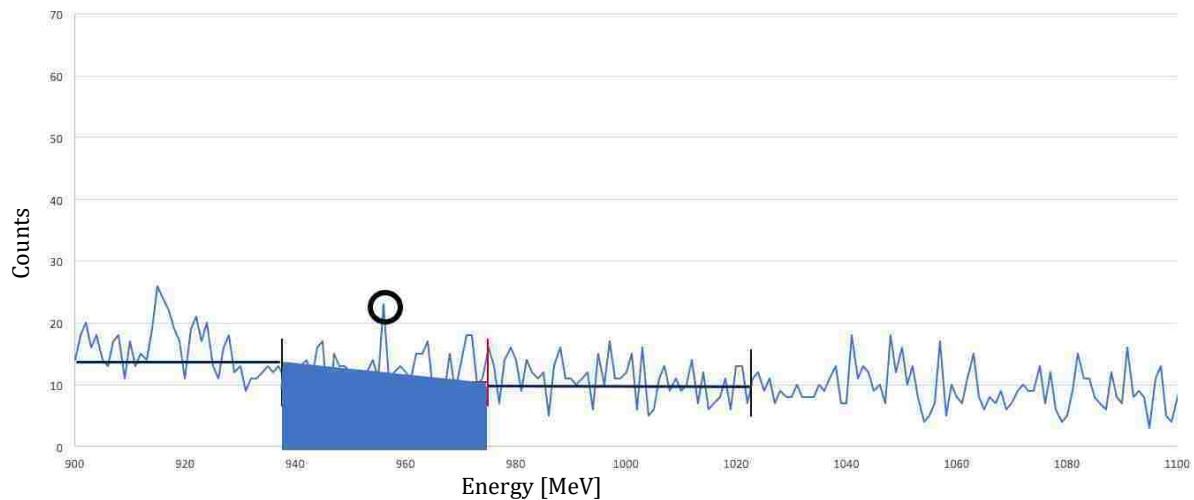
Figure 16: Trapezoidal background subtraction with no peak present.

In the experiments described in this thesis, the trapezoidal process of background subtraction was adopted later in the analysis and is referred to as "method two."

29

2.4 Imaging Theory and Calculations

Radioactive sources vary in their shape and size, as well as the intensity and type of radiation. From knowing the shape of a radioactive source much about its intent can be inferred. For instance, SNM in a sphere may be used for weapons pits. While similar material, in the shape of cylinders, is more than likely fuel for a nuclear plant. While both are highly regulated but if samples of each are found in the field, the response varies drastically.

Imaging radioactive material is thus important to SNM interdiction but has its inherent difficulties we address. Though gamma rays are photons just like light, they are harder to capture due to their high energy so exposing a film like in a photographic camera is not a feasible solution. Instead materials such as scintillators or semiconductors must be employed. If portability is necessary, then most scintillators are not practical due to the large amounts of power and the size needed for photomultiplier tubes. There are solutions such as silicon photomultiplier tubes, but poor energy resolution is a concern where material identification is of importance. There are two different techniques for gamma ray imaging, direct and indirect, both of which will be discussed here.

2.4.1 Indirect vs. Direct Imaging

The most common form of indirect imaging is Compton scatter imaging or, more commonly, known as Compton cameras. For Compton scatter imaging to be effective Compton scatter needs to be a probable form of radiation interaction. Figure 7 showed

that Compton imaging only becomes the dominant mode of interaction for high Z

materials at energies around 1 MeV. This is not ideal for SNM, where most of the gamma

rays are significantly below the Compton interaction region, in the range of 100 keV.

Certain high energy lines are known from SNM daughter products, such as the 1001 keV

line from Pa234m, a daughter of U238, but it is present in an extremely small fraction of

the decay chains. Compton cameras also require post processing of the data to converge

on an image. Source position is inferred from the scatter angle of a gamma ray so there is

significant computational power to do the calculations to image the source.

In contrast, direct imaging records the location of a gamma ray that is incident on

a material and using imaging techniques such as collimation or pinhole imaging mask the

source can be located simply though ray tracing. Collimated imaging involves the

shielding out of gamma rays from all but a small range of angles, called the angle of

acceptance. Smaller angles of acceptance give better spatial resolution to a source but

lowers the efficiency of the detector while larger angles have the opposite effect. The

balance in the trade-off of efficiency and spatial resolution is selected depending on what

the application of the imaging system requires. Finally, collimated imaging can be

performed using a single movable detector or an array of detectors to generate an image.

2.4.2 Direct Imaging Variables

Pinhole imaging is the projection of the radiation generated by a source onto a

detector through a pinhole, producing an image of the source on the detector image plane.

This concept is shown in its most basic form in Figure 17. The magnification of the

image, M, is described by Equation 8 which is the simple ratio of the distances from the

mask to the detector plane and the source to the mask.
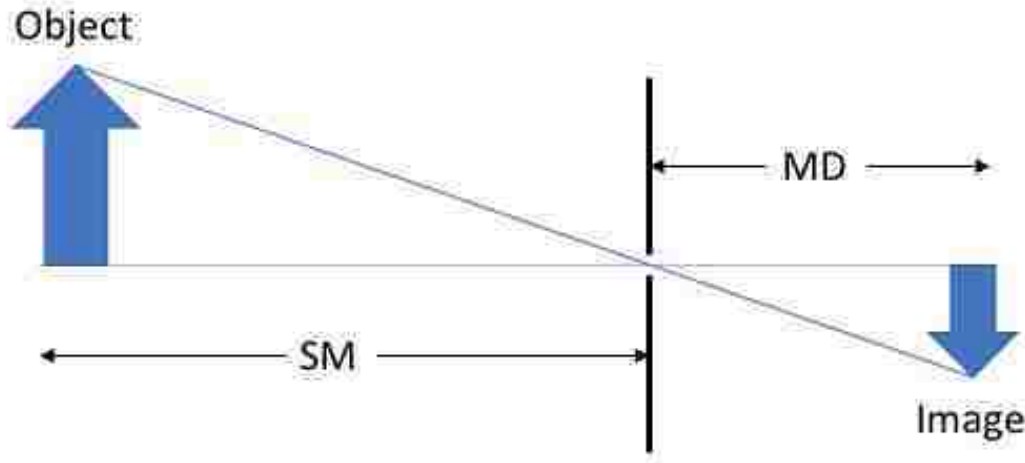
Figure 17: An object, distance SM from a pinhole mask is inversely imaged on a plane, distance MD, from the pinhole.

$$M = \frac{Image\ Size}{Object\ Size} = \frac{MD}{SM} \qquad (8)$$

 Only position sensitive detectors such as pixelated solid-state detectors can

utilize this imaging technique. The resolution of pinhole imaging is highly dependent on

the pixel density of the radiation detector and the pinhole size. Large crystals can be

effectively pixelated using pixelated electrodes. Single pinhole imaging produces an

inverted image of source on the detector which is a very simple and easy to interoperate

the image produced. The size of the pinhole is directly related to the resolution of the

image and the distance from source to pinhole mask and the pinhole mask to the detector

plane.

Pinhole imaging has the problem of relatively low efficiency both in terms of the

number of gamma rays which are allow through the pinhole and in terms of detector

utilization, or the fraction of the total imaging space onto which the image is projected. A

solution to this is multiple pinhole imaging. Multiple pinholes allow for an increased

number of gamma rays to interact with the detector producing many smaller images. This may keep the resolution similar and may utilize more of the detector space, which is part of the subject of the current research.

There are two types of mask which multiple pinhole imaging can use, those which produce overlapping images - also called coded aperture imaging - and those that produce non-overlapping images. Coded aperture is where pinholes are placed densely on the mask so that images overlap in their intensity. If the coded aperture positions are known the data can be analyzed so that the overlapping images can be reconstructed. Coded aperture increases the efficiency of the detector beyond a single pinhole, but the data only converges to an image after processing. Non-overlapping image multiple pinhole imaging produces multiple images of the object. These sub images can then be added in various ways to produce an image of the source. Even if the images are not processed then the shape of the source can be extracted immediately from the sub-images. Regular spacing was used for the pinhole masks in this research for clarity of interpretation and ease of manufacture. For regularly spaced pinholes there are four variables which can be controlled to give optimal images: the number of pinholes, spacing of the pinhole array, diameter of the pinholes and the thickness of the mask. The distances between source and mask, and mask and detector, can also be varied.

As the number of pinholes increases so does the geometric efficiency and the angular information about the source. Higher efficiency allows for more intensity to be gathered in a smaller amount of time. Additionally, angular information can be used for more robust reconstruction of the object being imaged, providing depth information. The more pixels there are the smaller each sub-image will be, and it is more likely that the

pixilation of the detector will begin to limit the resolution of the image. Using fewer pinholes allows the magnification of each sub-image to be increased. With larger magnification the clearer the image for each sub-image. With fewer pinholes, less gamma rays impact on the detector and the overall intensity of the source is decreased.

The multiple sub-images can be added to reconstruct a higher resolution full image. By information theory, if each of the sub-images contains different information - for example by illuminating a slightly different pattern on the pixels - then the N pixels added to the full reconstructed image can increase resolution by up to N times. Thus, the multiple low resolution sub-images using the multiple pinhole mask can give as good a final image resolution as the single hole mask positioned to give a greater single image size.

There are constraints on the pinhole spacing, width, and pinhole mask thickness. The spacing of the pinholes must be within constraints which are dictated by the size of the detector. Pinholes that are spaced to widely where some do not project onto the detector surface makes some pinholes not useful. On the other hand, pinholes which are spaced too close together can cause sub image overlap. This can lead to faulty reconstruction of the object.

The larger the pinhole the larger the projected image, when assuming constant magnification, and thus the worse the image resolution, though larger pinholes also leads to increased efficiency. The thickness of the mask may need to change with the energy of the gamma ray imaged and the necessary angle of acceptance. High energy photons can penetrate the mask material. Thick masks decrease the chance that gamma rays of higher energy might be detected where no image is supposed to be projected and thus muddy the

reconstruction. Thicker masks may limit the angle of acceptance of each pinhole and can lead to significant blind spots in detection of a source if the angle of acceptance is too small.

The effect that these parameters have on a resulting image and its reconstruction must be considered when using a pinhole imager. There are pros and cons to changing each variable and those might change depending on the situation. For this reason, it is important to develop a modular device which can use multiple pinholes that allow adaptation for any situation.

2.4.3 Image Reconstruction

There are multiple methods which can be used to reconstruct an image from multiple sub images. Only two will be discussed in this document, overlap reconstruction and maximum likelihood expectation maximization (MLEM). A MLEM method is discussed in length in, *A model-based multiple-pinhole synthetic imager for stand-off range* (DeRego, 2016). This research used a more straightforward approach, in overlap reconstruction, so in this section the process of overlap reconstruction will be discussed.

The underlying theory behind our overlap reconstruction relies on regularly, spaced pinholes to project images on to the detector surface. Since the pinholes are laterally offset from each other, the images are offset on the pixelated detector and each sub-image produces slightly different information from the others, with the sub-images at regular distances from each other. This information can give information about the shape of the source and its position.

The full image can be reconstructed by overlapping the sub-images with the

correct spatial frequency. Image overlap is a straight-forward reconstruction technique.

Multiple images of an object are generated by a detector. Each sub-image is projected

onto a different location on the detector face. Each sub-image has slightly different

information depending on its position on the detector face and thus its pixelated

representation. The full pattern of sub-images is mapped to a sum pattern, with the

pattern repeated with a spatial offset in each representation that is added determined by

the spatial offset of the sub-images. In the final sum pattern, the image at the center of

these overlaps is then a sum of all of the sub-images. This serves as the full sum

reconstructed image of the object. This method is demonstrated visually in Figure 18.
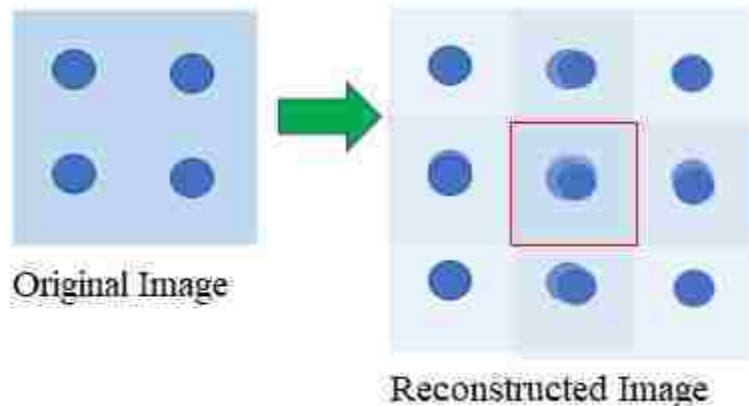
Figure 18: The original image is tiled so that it overlaps the other sub images that were generated. The sum of the overlaps is the reconstructed image, boxed in red.

2.4.3.1 Image Reconstruction Resolution

The resolution of the image that is reconstructed has a direct relation to number of

pixels used in the reconstruction as well as the spacing between the sub-images. The

original image is 22 x 22 pixels each with a size of 2 mm^2 due to the constraints by the

detector. The pixel size is the resolution limit considering only integer spaced pixels and

if the 484 pixels are each overlaid, the reconstruction will have a resolution of 2 mm.

However, the spacing between sub-images is not always an integer number. If the number of pixels between the brightest spot on each sub-image is counted and then averaged (there are 24 such spacing in a 16 sub-image array) it will most likely not be an integer result. If every pixel from the original image is expanded into 100 "reconstruction" pixels in a 10 x 10 array we gain the ability to have a non-integer pixel spacing of the reconstructed image. This allows for sub-images with different information to appear offset from each other and give finer detail in reconstructed image. Figure 19 shows how sub-images can be overlaid with slight offsets to obtain a sharper resolution in the reconstruction then possible with any of the sub-images. The results of how image reconstruction changes as the sub-image spacing changes is shown first in Section 5.3.
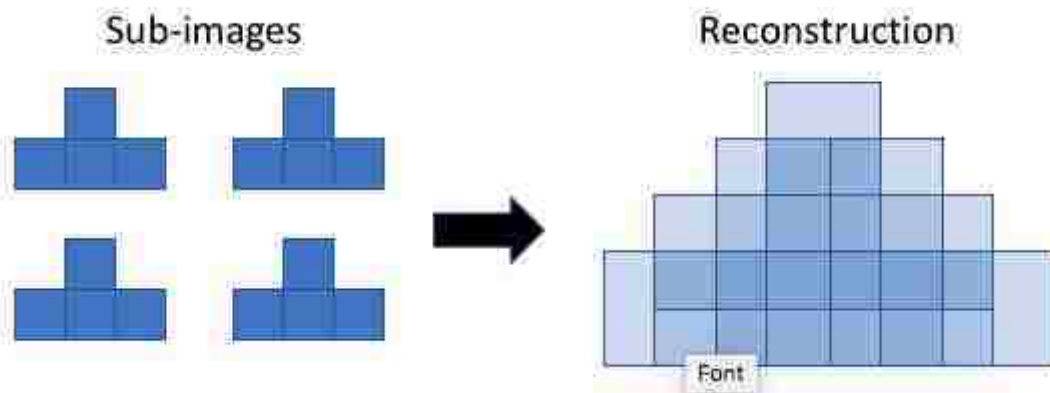
Figure 19: Four sub-images can be expanded and overload to create a reconstruction of the original object with higher resolution.

2.4.3.2 Intensity

The intensity, or number of gamma rays, which impact on the detector is import for imaging speed and accuracy by increasing the amount of information or signal strength compared to the background noise. The number of pinholes used in a mask is the main factor for the intensity of the image. While detector usage is important and should be maximized it is not always directly proportional to the number of gamma rays

37

collected by the detector. Figure 20 shows how a single pinhole image can use

approximately 46% of the detector space while 16 pinholes only use about 30%. Using

the reconstruction techniques mentioned in the previous section it is possible to layer the

sub-images from the multiple pinhole mask and total gamma ray intensity of the

reconstructed image will almost 5 times that of the single pinhole. In theory this allows

for a collection time that is 5 times faster with a signal to noise ratio that is increased by 5

times. There can also be problems with the relative intensity of pixels on a detector. An

image that is comprised of many overlaid sub-images will have a greater uniformity than

an image that relies off of each individual pixel response.
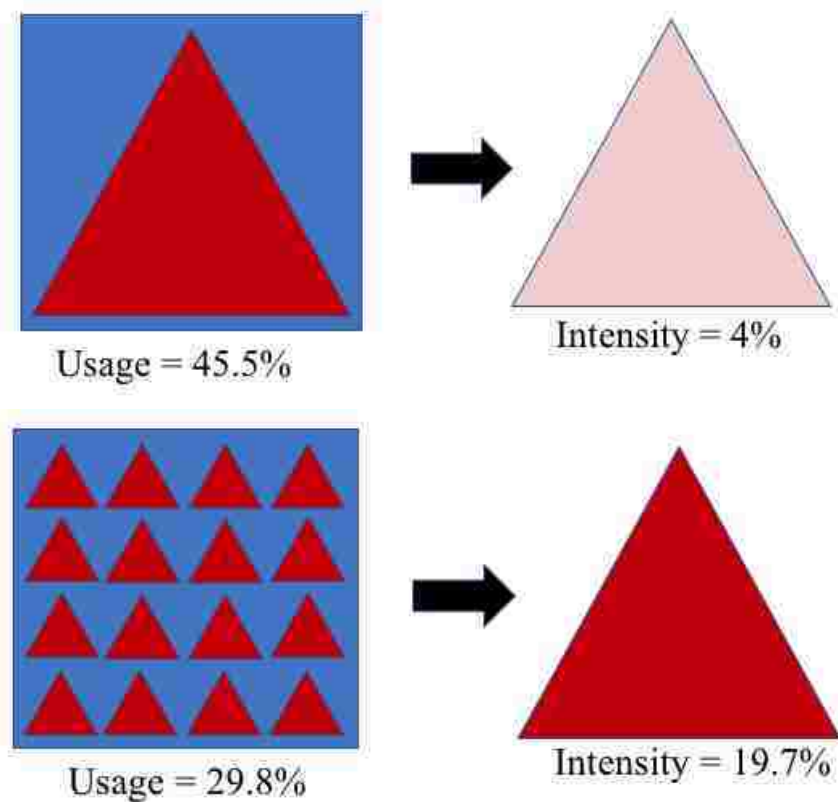
Figure 20: Comparison of single pinhole and multiple pinhole masks with detector usage and gamma ray intensity.

2.4.4 Depth of Field

Depth of field is one of the more intriguing possibilities involving multiple pinhole imaging. As the distance from the source to the pinhole mask changes, the spacing between the sub-images changes. The farther a source is from the collimator to closer the sub-images will become until a certain distance is met where the detector sees the source radiation coming in normal to the mask and detector face and the sub-image center-to-center spacing is the pinhole spacing. The closer a source is to the collimator the farther the sub-images will be separated until, in the real system, the source begins to be cut off from the outer most pinholes due to the thickness of the mask or the image is projected outside the area of the detector surface.

The spacing between images, with a known mask-to-detector distance, can give information about the distance of the source from the detector. For a source along the middle of the normal to the detector imaging plane, the ray between the source point and a chosen pinhole is a like triangle to the ray between the source and the image on the detector plane. Thus, the ratio of source-to-image/source-to-mask distances is the same as the ratio of center-to-pinhole/center-to-image distances. Figure 21 shows how the projections of sources at two different distances (X and Y) from the pinhole mask can create two different sized projections on the detector, im_1 and im_2.
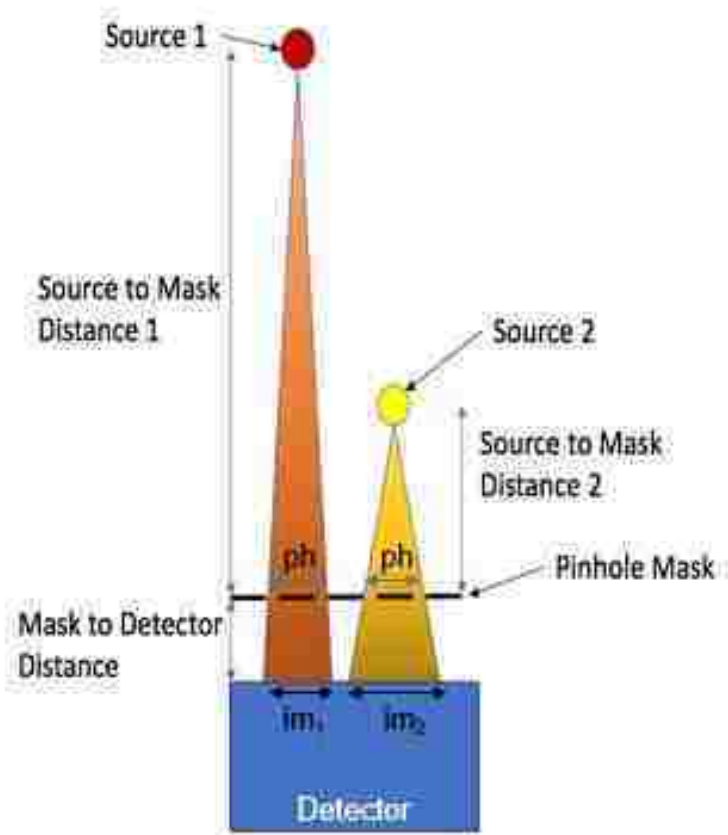
Figure 21: Two source at two different distances create two different sized projections of the detector.

Using like triangles it is easy to generate a geometric relationship between the pinhole spacing (ph), sub-image spacing (im), source-to-mask distance and mask-to-detector distance (MD). This starts by redefining what we call magnification, now referred to as $\mathcal{M}$. Now the object is the spacing between the pinholes and the image is the reserve "shadow" of the pinholes on the imaging plane show in Equation 9.

$$\mathcal{M} = \frac{image}{object} = \frac{(SM+MD)}{SM} = \frac{im}{ph} \tag{9}$$

Solving equation 9 for SM gives Equation 10. This will be applied to depth of field data in section 5.3.4.

$$SM = \frac{MD}{\mathcal{M}-1} \tag{10}$$

3. Nozzle Collimated Imager

3.1 Design

The nozzle collimated imager consisted of X Y and Z. Collimator nozzle tube in front of X size CZT detector. The tube was mounted on a plate to shield the detector from radiation from other directions. This experimental setup is shown in Figure 22.

Figure 22: Nozzle collimated imaging system.

For this project a resolution of 1 cm at 50 cm distance is desired, meaning a point source at 50 cm is imaged as 1 cm FWHM on the detector plane and to achieve that a nozzle collimator must be used. The chosen collimator material is lead due to its gamma attenuation properties and considerable ease to machine and shape vs. tungsten. The thickness of this collimator was 0.1 cm, this is because the low energy gamma rays which

we are imaging are easily attenuated by little material. As the detector is not within the nozzle but behind it, there is a thin lead lining around the detector crystal to shield it from gammas which may enter from the side.

Hand calculations were done to estimate the length of nozzle collimator needed to obtain a lateral source position resolution of 1 cm at a distance of 50 cm. First, Equation 11 was derived to relate the terms in Figure 23 where L is length from source-to-detector, d is height of nozzle, offset is the radial offset of the source at which it can still be seen by half the detector, w is the width of the detector and theta is the angle created. All lengths are in cm. The lateral positions are in x and y, while the distance between the image plane and the source, shown here as L, is the z direction.
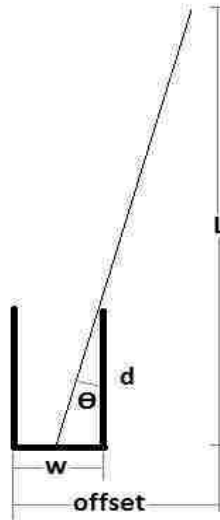
Figure 23: Setup for resolution determination.

$$\tan(\theta) = \frac{W/2}{d} = \frac{offset}{L} \qquad (11)$$

Equating the center and right sides of the equation and then inputting our known values to solve for d we can get Equation 12.

$$d = WL \qquad\qquad\qquad (12)$$

Solving Equation 12 for a detector crystal with a face of 5 mm x 5 mm area and a

source-to-detector distance of 50 cm we get a nozzle collimator minimum length of 15

cm for a 1 cm determination of the source's lateral position.

3.2 Modeling

A simulation in MCNP6 with the dimensions was then tested, see appendix A. This was

done by taking a point source and moving it across the face of the detector in a line at a

distance of 50 cm from the detector plane. The raw counts were then taken at each

position and plotted in Figure 24.
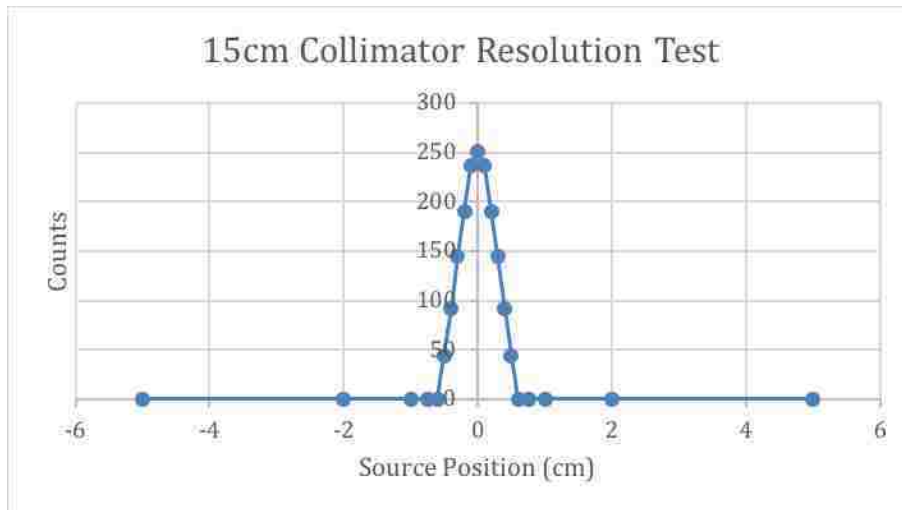
Figure 24: Results from the resolution simulation.

The full width half max of this peak is less than 1 cm so now we have a detector

setup which is then able to test in a full imaging setup. Two imaging tests were done, one

was the full imaging of a 2 cm radius disk source and the other was a quarter image of a 5

cm radius disk source. Each of these images were created by moving the detector in both

x and y by 1 cm increments. The total activity of the source was 20 µCi, this was then

normalized to the total imaging time being 30 minutes. This results in each MCNP6 run

having 5.44 X 10^7 particles. The raw counts which were observed in the detector at each

location were then put into a matrix used to generate spatial distribution images. Figure

25 shows the simulation setup and Figure 26 is the image of the full 2 cm radius disk

source.

Figure 25: Basic schematic of detector (left) and source (right) in simulation. The source is shown in red with the collimator represented to the right of it. Arrows suggest directions of motion.
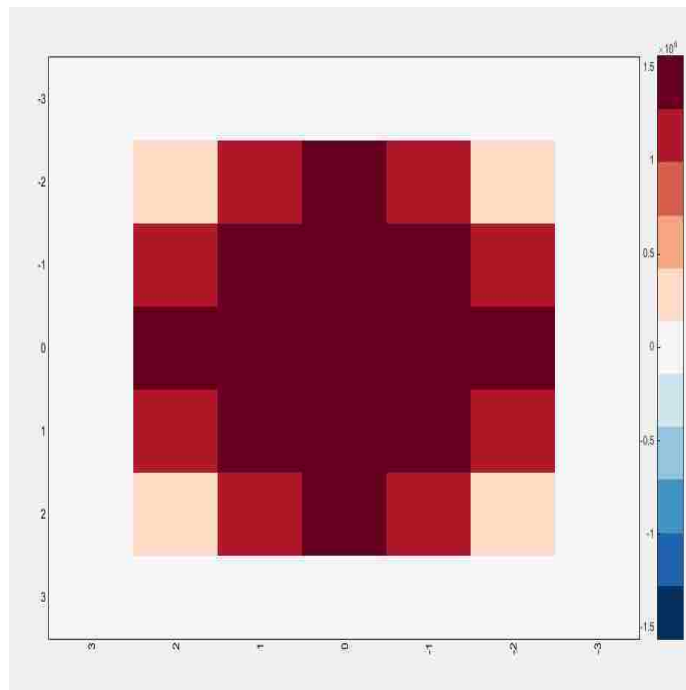
Figure 26: Image of 2 cm radius disk source.

The simulation results presented in Figure 26 shows that at a radial distance of 3

cm from the center of the 2 cm radius source, which is 1 cm beyond the edge, the counts

went to background levels, suggesting better than 1 cm resolution. Figure 27 is then a comparison of the simulated detector response with different level of simulated noise which is statistically generated. There are large fluctuations the higher the noise is, the less noise there is the more the source stands out as the detector images it. Noise is listed relative to the average signal (from -2 cm to +2 cm, collimator line of sight of source) in the detector, with statistical variation of $\sigma = \sqrt{N}$ of noise N for each position. The noise is added post simulation.
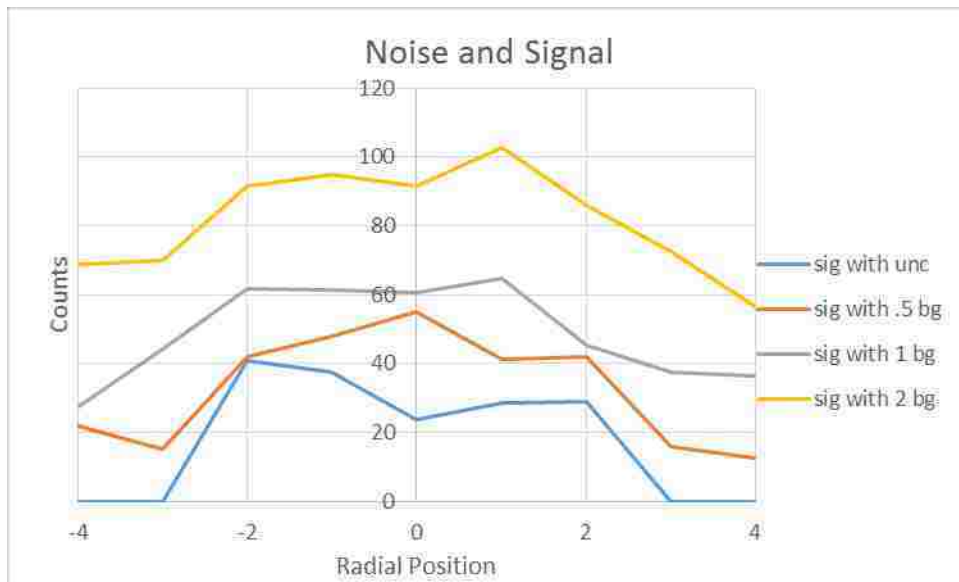
Figure 27: Profile comparison of detector response with different levels of background noise.

Next the 5 cm radius disk source was imaged and the resulting image in Figure 28 was created.
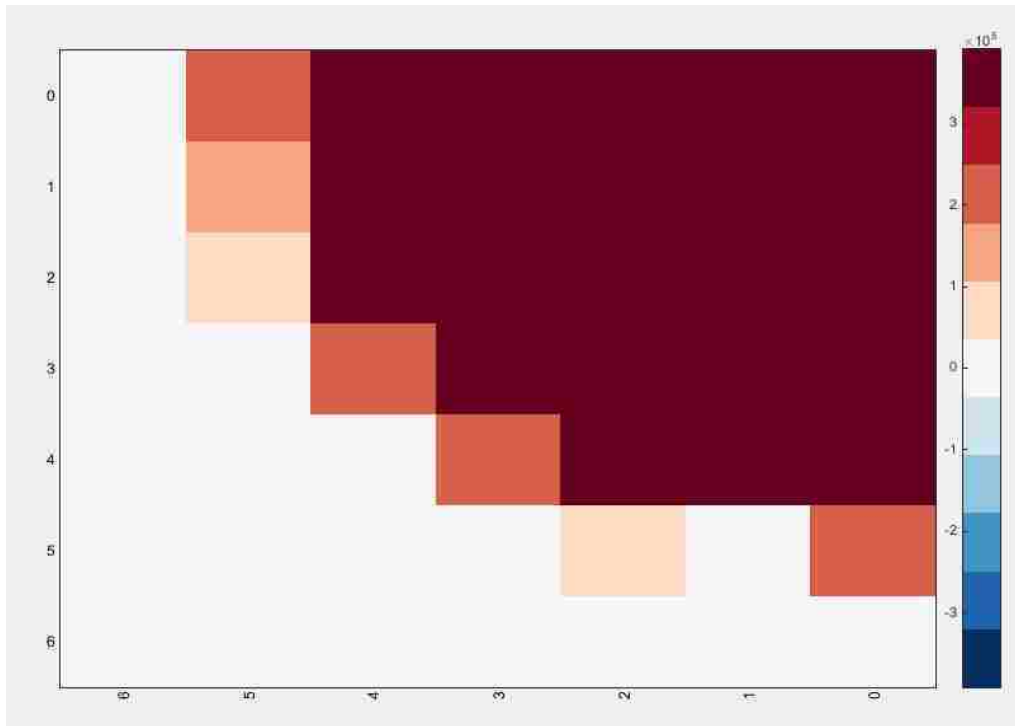
Figure 28: Quarter of 5 cm radius disk image.

The simulated 5 cm radius disk measurement also shows a 1 cm resolution. Once the detector is beyond the scope of the source the counts quickly drop off. The two dimensional plots of detector response as a function of position show the geometries of the disk sources very clearly, with better than 1 cm resolution. As the spatial imaging of the source intensity is dependent on several individual readings, this is not a simple case of a single signal vs. noise in a single reading but a set of signals, and the source image may be resolved from the general pattern even with a very low signal-to-noise ratio. This is demonstrated by the signal profile plots across the face of the 2 cm radius disk source, Figure 27. This appears to be a robust method for detection and spatial discrimination.

46

3.3 Experimental Methodology

3.3.1 Detector

The detector which was chosen to be modeled for these simulations meets all the project requirements for the moveable collimated imager. It is an XR-100CR-CZT detector from Amptek pictured below in Figure 29. The Amptek detector has a 5 mm x 5 mm crystal face with 2 mm thickness. This was the geometry used in the disk imaging simulations.

Figure 29: Amptek detector unit with power supply (right) and internal design of detector and cooler (left). [42]

3.3.2 Background and Source Characterization

Single point imaging was performed with several different sources with two different nuclides, Co-57 and Eu-152. SNM sources on hand are more spatially distributed and so these low energy, gamma ray source stand-ins were used instead of SNM. Eu-152 has a set of close spectral lines near 40.12 keV that were used for photon counting. This is a region of low background and a region of high detection efficiency for the detector. The spectrum is shown in Figure 30, with the 40.12 keV peak around

channel 200 in the spectrum. Co-57 was also used for imaging, and the strongest line is

122.06 keV, shown in Figure 31 as the peak near channel 600.
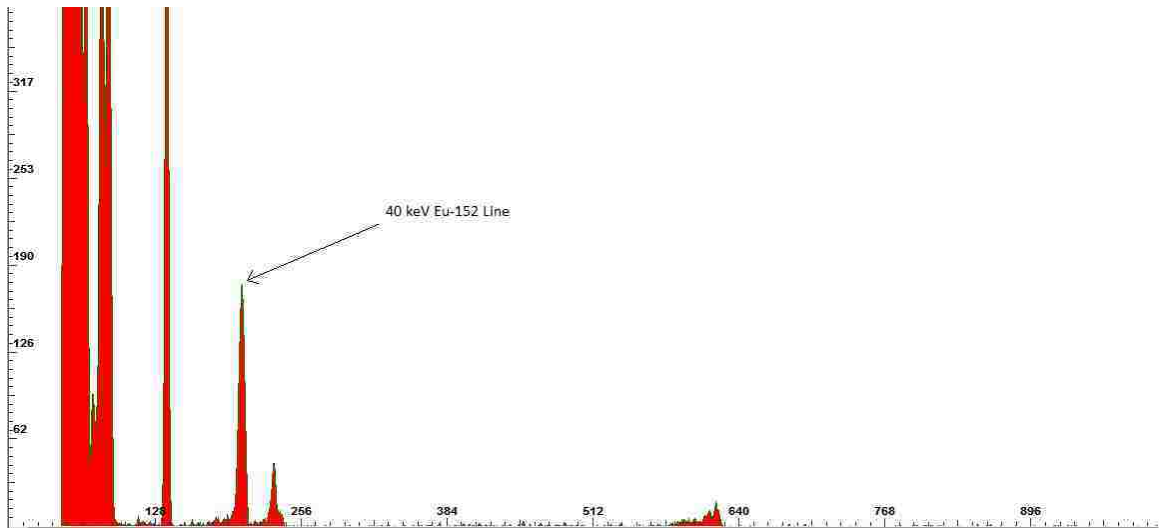
Figure 30: Energy spectrum (uncalibrated) of Eu-152.
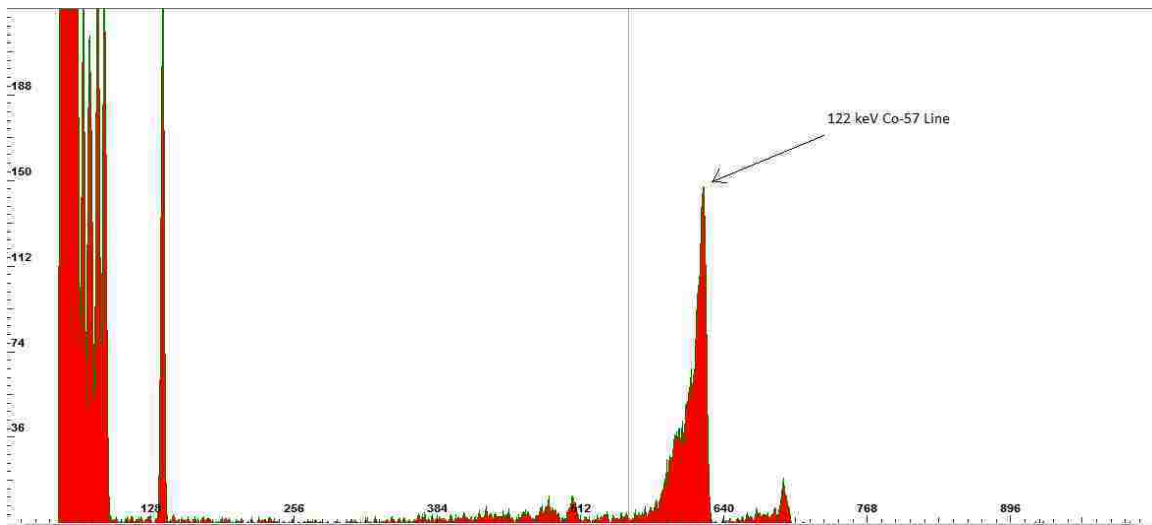
Figure 31: Energy spectrum (uncalibrated) of Co-57.

Next the lab background spectrum was characterized. Over the course of a few

days the background in the lab was measured and is displayed in Figure 32. While there

were no serious deviations in background there was a general decrease in background

over these days.

48
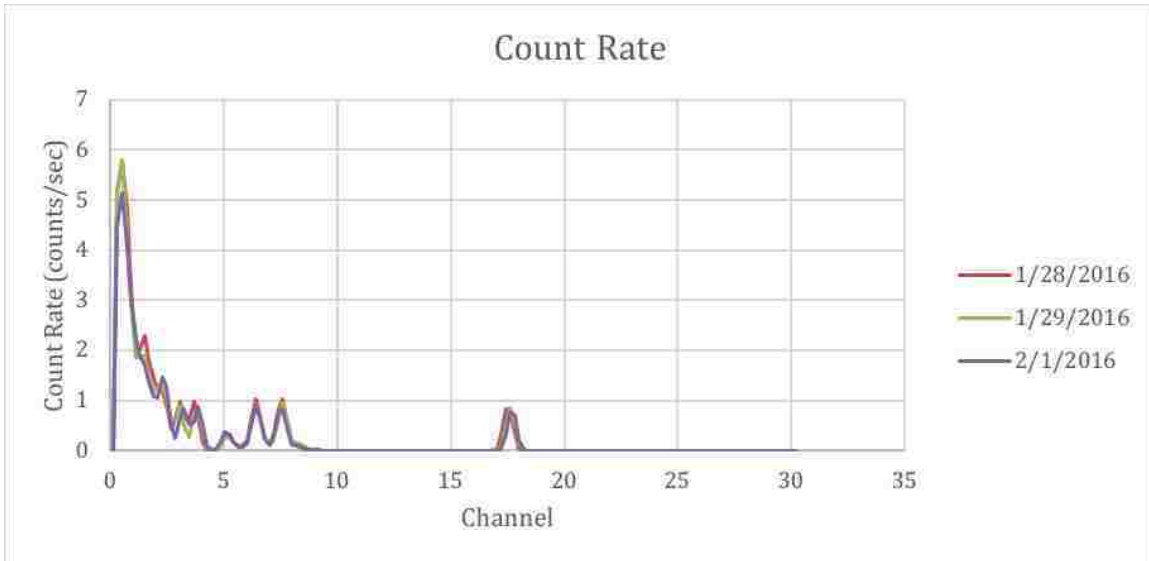
Figure 32: Background count rates in the lab over different days.

Next the background was checked in Dr. Hecht's office compared to the lab to see if location changed the background which is shown in Figure 33. What was saw was, again, no significant change in the background levels in Dr. Hecht's office compared to the lab.
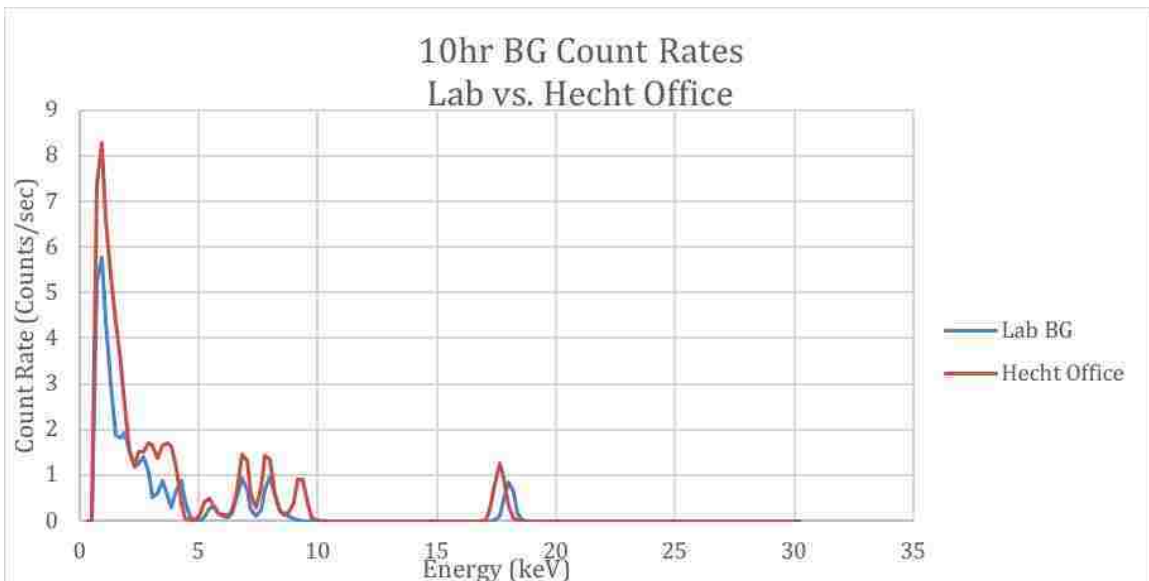
Figure 33: Background count rates in Dr. Hecht's office vs background rates in the lab.

To get background as lows as possible the detector was placed in a lead enclosure with no straight-through gaps to the outside, as well as in a lead collar, to block out all

49

external background radiation. Figure 34 is a photo of the lead enclosure and Figure 35 shows the results from the experiment. It should be mentioned that the results in Figure 35 look slightly different that other background runs because of a change in threshold. This was to better see low energy effects in a reduced noise environment such as the lead enclosure.
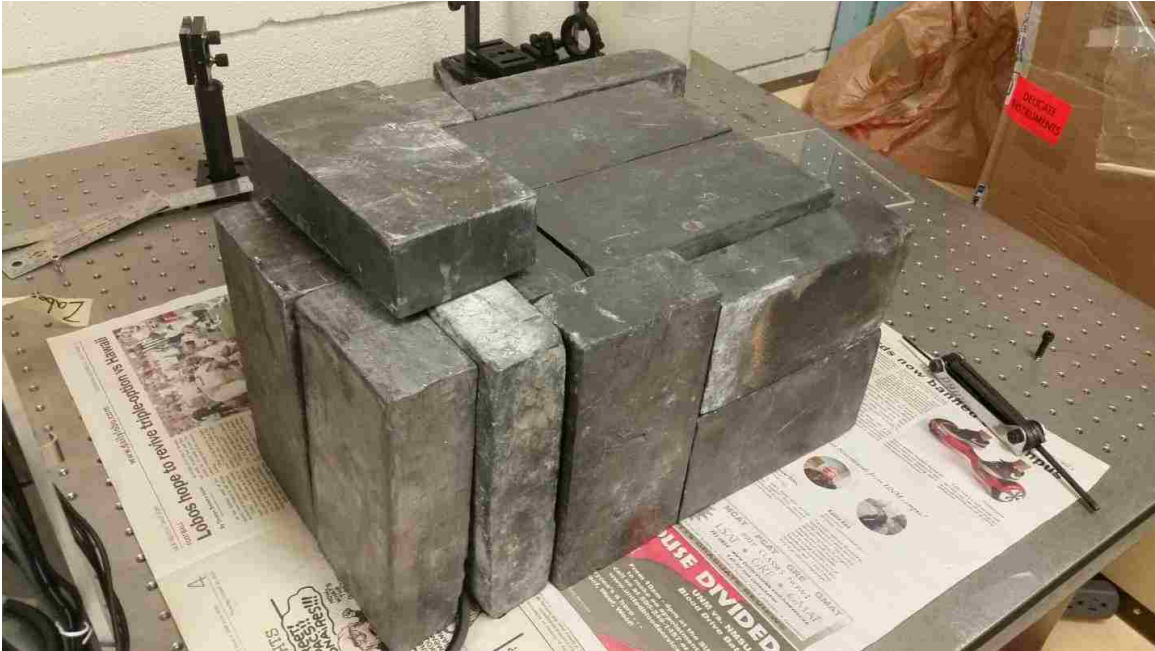
Figure 34: Lead enclosure for detector.
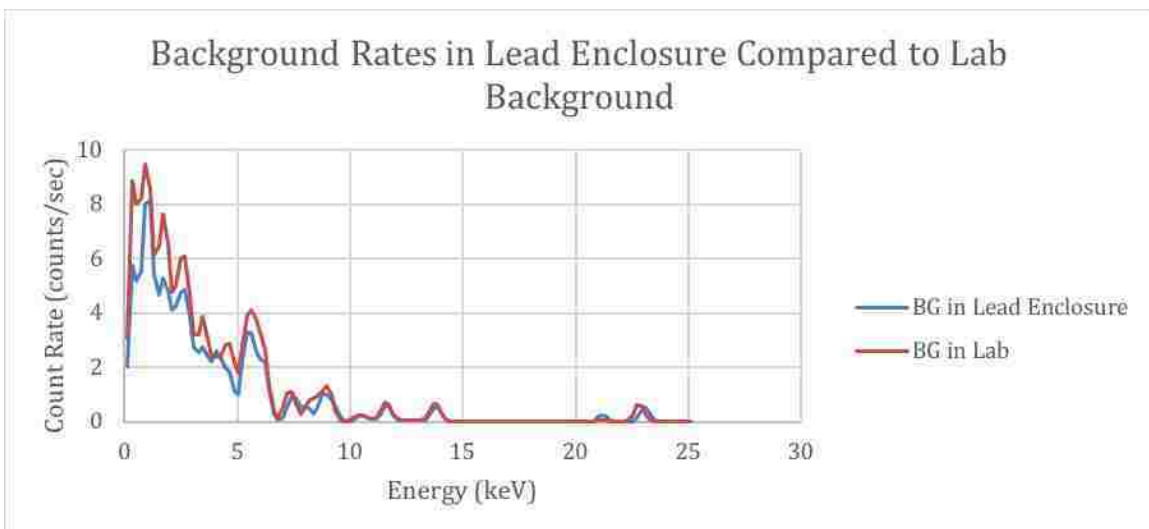
Figure 35: Lead enclosure background vs background found in lab.

This showed a definite decrease compared to the lab background at very low energies and left us confident on what we could classify as lab background vs. internal noise of the system. For this we did a subtraction of the lead shielded background spectrum from the room background spectrum, summarized in Figure 36.
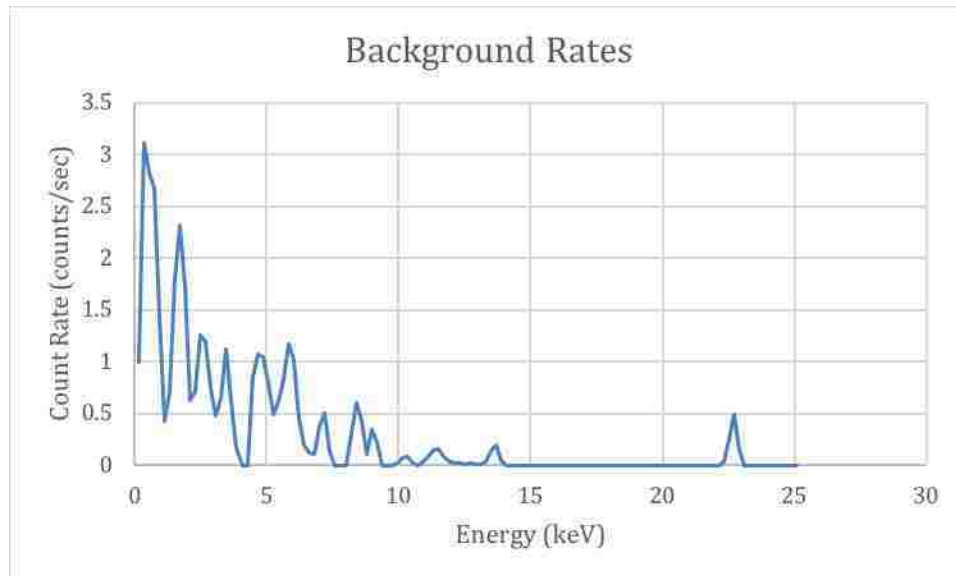
Figure 36: Background rate expected in lab.

3.3.3 One Dimensional Imaging

To perform spatial imaging the collimated detector took measurements over a series of positions, for a selected time over each of the positions. The detector was moved to a different position, automatically controlled by the detector control program, and another count was performed. This was continued over the spatial range selected with the spatial steps selected. The spectra taken at each position were analyzed to determine the number of counts in the peak of interest using background subtraction "method one".

Steps were first taken in only the horizontal (x) direction, with the source directly in front of one of the positions, to examine the lateral response of the detector to a small source. That is, imaging the source as a function of lateral offset (x) of the detector. The

sources used for this are not actually concentrated at a point but have an active area

diameter of approximately 2 mm. These results are shown in Figure 37. The spatial

resolution of these images is defined as the one dimensional full width half maximum

(FWHM).
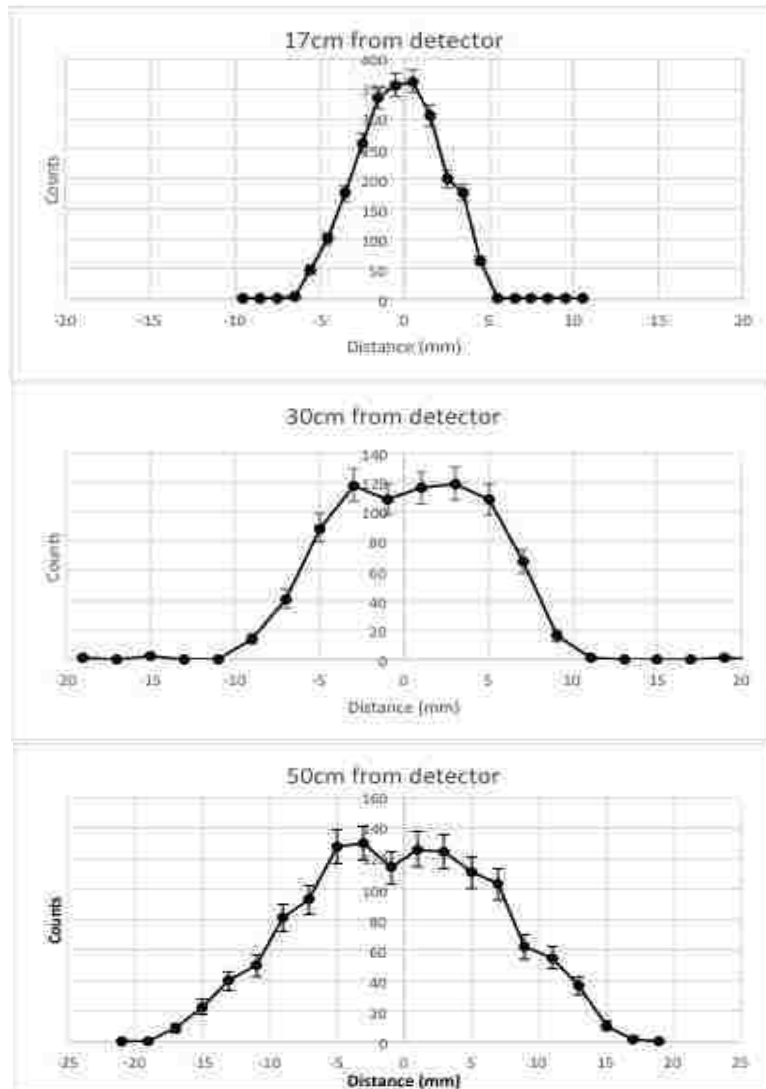
Figure 37: one dimensional imaging of source at different positions, with detector moved laterally (x). Top, source at 17 cm from detector, the closest with the detector collimated and in the box; middle, source at 30 cm; and bottom, source at 50 cm.

The figures show detector intensities at 40 keV, as a function of lateral position of

the collimated detector. The plots are repeated for three different source-to-detector

plane distances, 17 cm (top), 30 cm (middle) and 50 cm (bottom). It's clear from Figure

52

37 that the image using the source close to the detector/collimator setup has a smaller

spatial spread, while the image for the source far from the detector/collimator has a

smaller spatial spread.

The imaging is restricted to that region in front of the collimator such that the

photons can follow a straight path to the detector without striking the shielding of the

collimator. Thus, photons emitted within a given angular range are allowed in, following

the relation in Equation 13.

$$\tan \theta = \frac{x}{z} \qquad\qquad (13)$$

The lateral offset, x, from the source and z being the distance between the source

and the line of motion of the detector. Replotting the one dimensional images as a

function of angle rather than lateral offset, this becomes clear, see Figure 37. The data

from Figure 38 was normalized and re-centered to make comparison easier. The HWHM

of the system is $x/z = 0.0188$, corresponding with 0.0188 radians or 1.077 degrees. That

is, the FWHM of the images of the point sources is 0.04 radians or 2.3 degrees. The

image resolution is found by determining the minimum distance between sources (x)

where the images are still resolvable. This was calculated by choosing the minimum

distance between point sources as being the FWHM of each point source image. Using

the trigonometric relation, we can say the minimum x is $x = 0.0376z$ cm when the sources

are at a distance of z cm. For example, for $z = 25$ cm, the distance below which the point

sources can no longer be resolved as individual sources is 0.0376 x 25 cm = 0.94 cm.
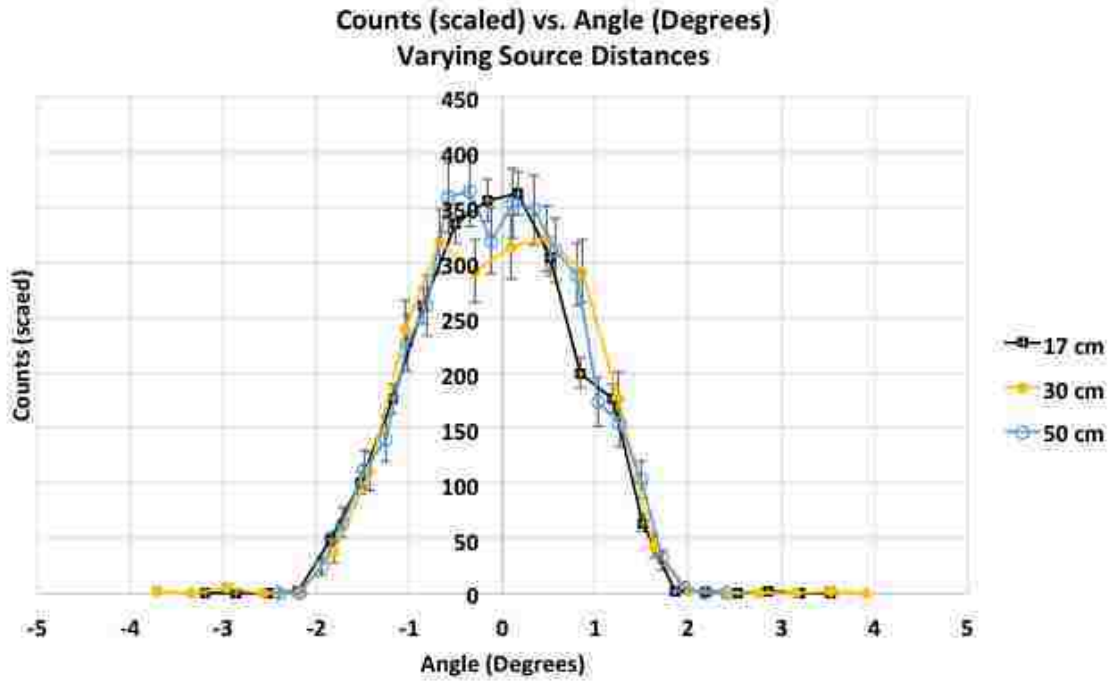
Figure 38: Angular representation of one dimensional imaging of point sources, for sources at several different detector to source (z) distances.

The next task was verification of the experimental calculations, to check experimentally that our geometry was giving us what we expected. For ease of calculation we performed one dimensional scans of sources. Figure 39 displays the basic outline of the experimental setup for the one dimensional scanning tests. The source is shown as moving in that Figure, though the detector was rastered. The relative motion is the important feature.
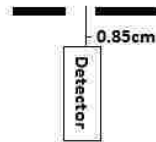
Figure 39: Experimental setup.

These one dimensional scans showed that experiments gave us what we expected. Any deviation shown is because of variation from the experiment from the theoretical calculation such as material getting in the way of the detector face as scanning was conducted. This was done at multiple distances and collimator configurations, each of which supported our initial claims and calculations. The 15 cm nozzle collimator was removed for all but one of the tests so as to test the detector response alone. Figure 40 displays experimental and expected theoretical values for a scan at 5 centimeters with no collimation.
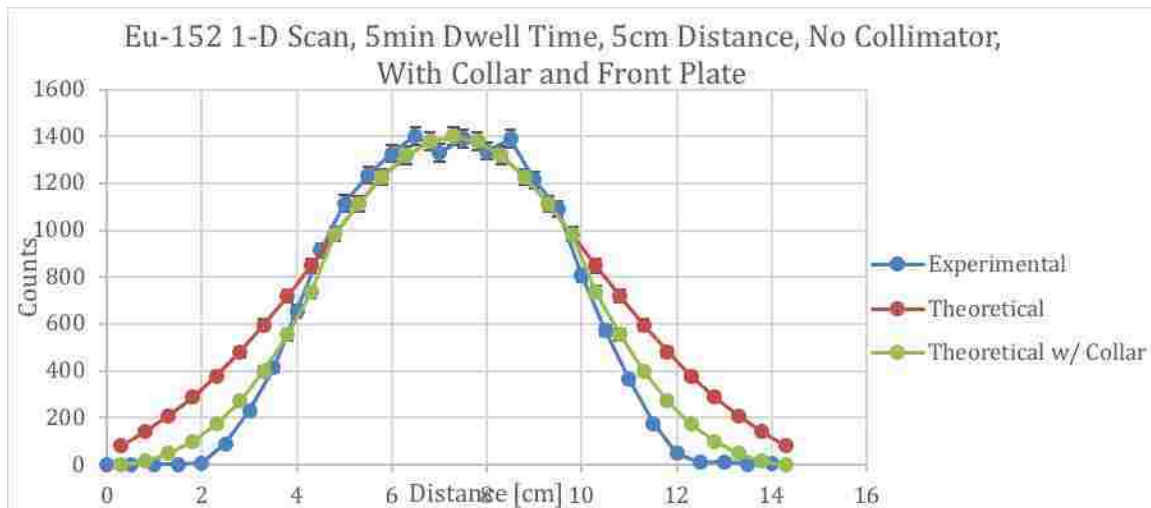
Figure 40: Theoretical vs. experimental results of the 5 cm one dimensional scan.

Figure 41 is experimental and expected theoretical values for a scan at 17 centimeters with no collimation. Only half that distance could be covered due to the wide view of the detector at 17 cm distance.
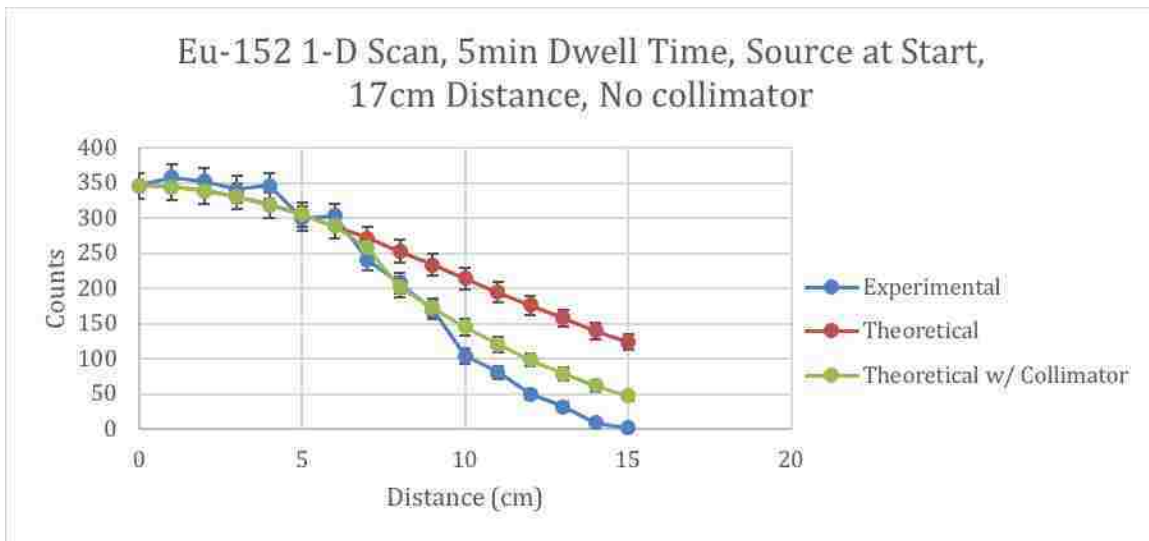
Figure 41: Theoretical vs. experimental results of the 17 cm one dimensional scan.
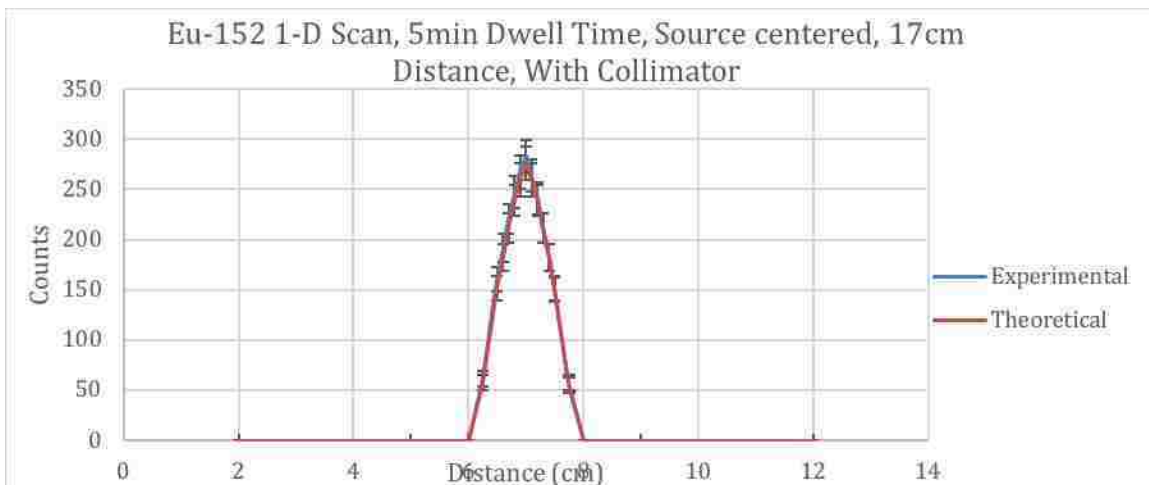
Figure 42: 17 cm one dimensional scan with nozzle collimator.

Figure 42 shows the nozzle collimated one dimensional scan of the detector. As is evident in these graphs the nozzle collimator creates a very well defined spatial resolution of the source. It is also in excellent agreement with the theoretical prediction.

3.4 Results

Two dimensional imaging was performed by the system, with the user input of a starting position, step size in x and in y, and time to take each position's spectral measurement. Spectral information within the energy range is counted for each position and the number of counts is saved in a position dependent array, and the total results are presented automatically in a two dimensional intensity plot. The spectra are presented as they are collected. An example of the computer display is presented in Figure 43.
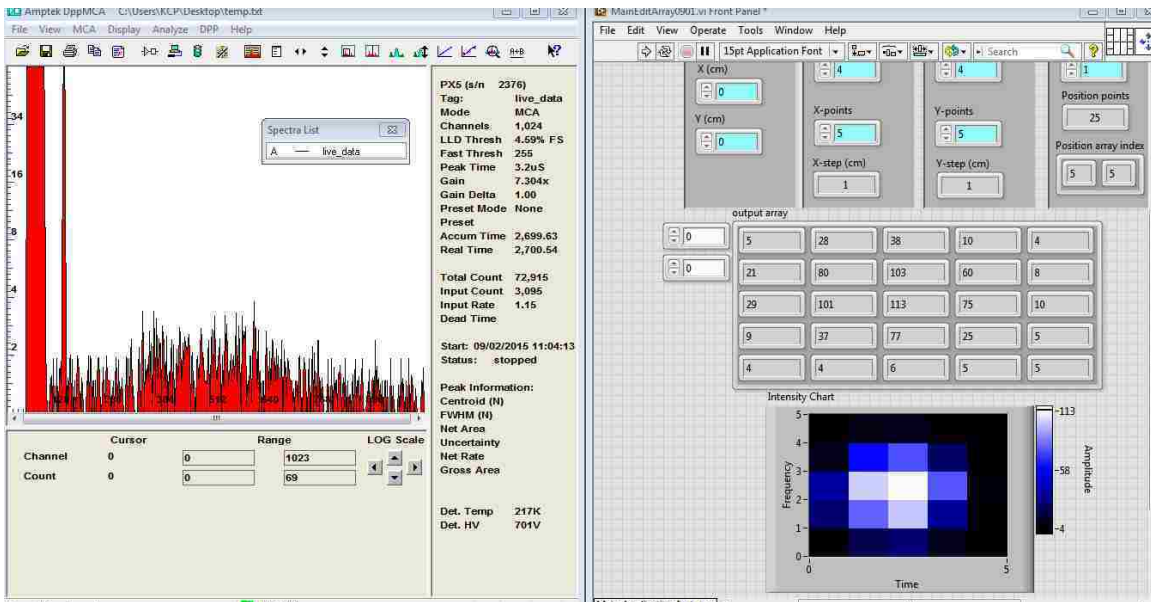
Figure 43: Screen image of computer program display.

Two dimensional images were taken in several different setups to examine detector response. The numerical values were converted to excel intensity plots for clarity, and to not only show screen shots. These are presented below with discussion. Numerical values of the counts in the peak are given in each of the pixel locations, and the intensity is color coded, black being zero and lighter colors representing higher counts.

3.4.1 Spatial Resolution

The first two images that were produced by the system can be seen in Figure 44. Both images were completed within 30 minutes, this means that relatively small areas could be imaged due to the time needed for collection at each pixel location. The number in each of pixel is the number of counts obtained by the detector. The 2 mm x 2 mm detector was moved in 2.5 mm steps, to create a pixelated image with 2.5 mm square pixels. Both sources are point sources and each was placed at $Z = 25$ cm. Each of sources show up on 3 pixels or the equivalent of 7.5 mm. This means that a spatial resolution of < 1.0 cm is obtainable at 25 cm distance.
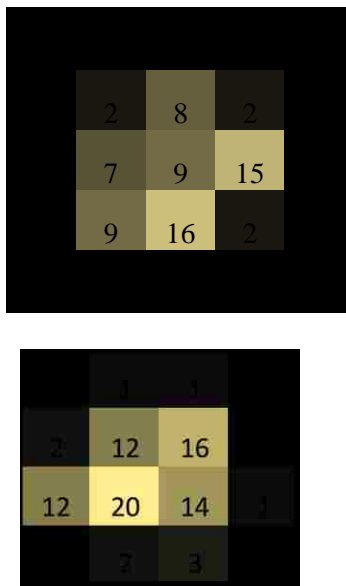
Figure 44: two dimensional test image of single point of Eu at 25 cm with 30 minute images, or n/30 minutes per pixel for n pixels, so top used ~1 minute per pixel and bottom used ~2 minutes per pixel. The two Eu sources (<1 μCi each) were stacked to increase intensity.

Next, both sources were imaged at the same time while positioned 3 cm apart. The distance of imaging was increased to 30 cm. As can be seen in Figure 45 there is definite separation between the sources but the spatial resolution decreases slightly to approximately 0.8 cm.

Figure 45: Two separated Eu-152 sources (3 cm apart) imaged at 30 cm from detector, at 5 minutes per pixel.

Finally, the sources were imaged at 50 cm distance from the detector while keeping the separation of the two sources at 3 cm. Now, in Figure 46, we can see that resolution is above 1 cm. There are no zero-count pixel between the two however when looking at cross sectional representation of this image, as in the graph for Figure 46, it is possible to resolve the two source peaks at -2 cm and 2 cm.
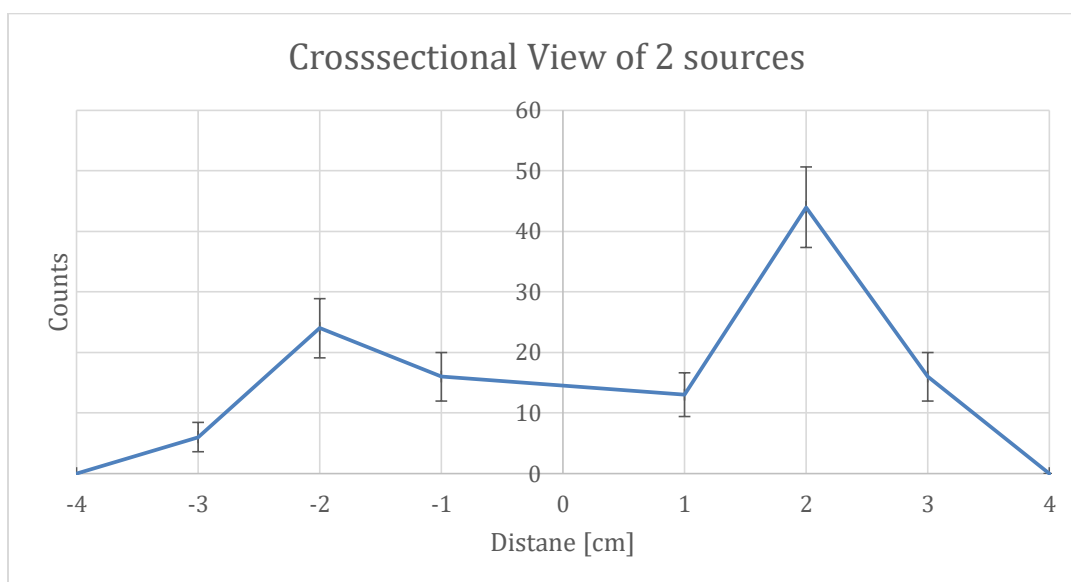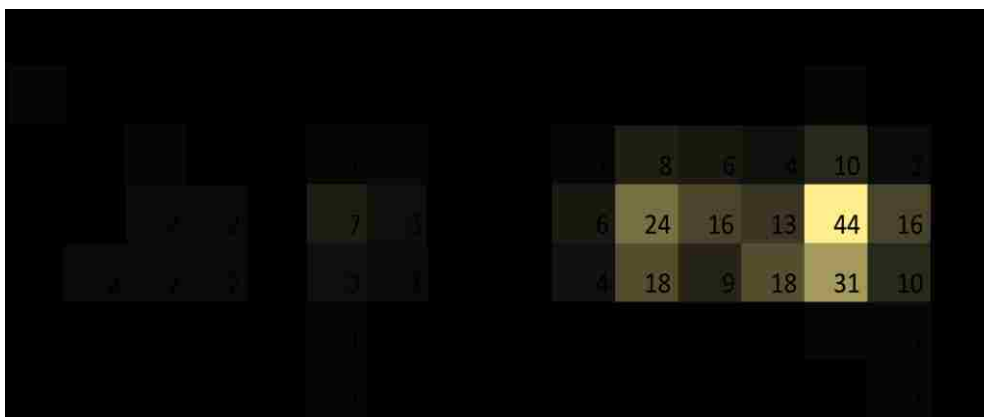
Figure 46: Two Eu sources in separate locations (3 cm apart) imaged at 50 cm from detector. Top left: 1 minute per pixel; top right: 5 minutes per pixel. Bottom: cross sectional view of the two sources.

The Eu-152 sources are very weak, with approximately 0.9 and 0.6 μCi of activity. For the 40 keV line (a combination of 39.522 keV and 40.118 keV lines) the branching per decay is a total of 20.5%, so the activity at that line is 6830 photons per second for the 0.9 μCi source and 4555 photons per second for the 0.6 μCi source, though emitted isotropically. At 50 cm from the detector with a surface area of 5x5 mm^2, the detector has an angular efficiency of only 0.0025%, and only 0.17 and 0.11 photons per

second are expected to hit the detector from the respective sources. Thus it is reasonable to use longer counting times.

A higher activity Co-57 source was acquired for this project. The source is spread over a 2 cm diameter active area, with a total activity of 30 µCi. For the same source-to-detector distance as discussed for Eu-152, 5.7 photons per second in the 122 keV peak are expected to hit the detector, though the detector efficiency at that energy is somewhat lower than at 40 keV. A 30 minute image at 50 cm is presented in Figure 47.
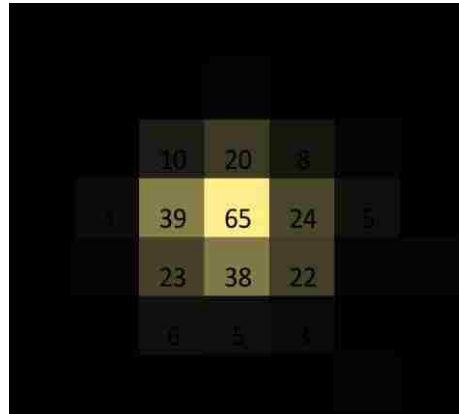
Figure 47: 30 minute image of Co57 source using the 122 keV line. Source distance 50 cm, 1 cm steps in x and y over 6 cm range each.

A detailed image of the source was needed to characterize the activity distribution across the face of the source. The source was brought to 17 cm from the detector and a highly detailed image was created as shown in Figure 48. The step sized used was 2 mm and the dwell time for creating each pixel was 15 seconds. This means that there is some overlap between pixels because the nozzle collimator has a diameter of 7 mm. It still gave us a good idea of the detail of the source. There are definitely some pixels which are reporting statistically significant deviations in the middle of the source, this points towards the source not being as uniformly distributed as originally thought but for now this is the most detailed image we can take.
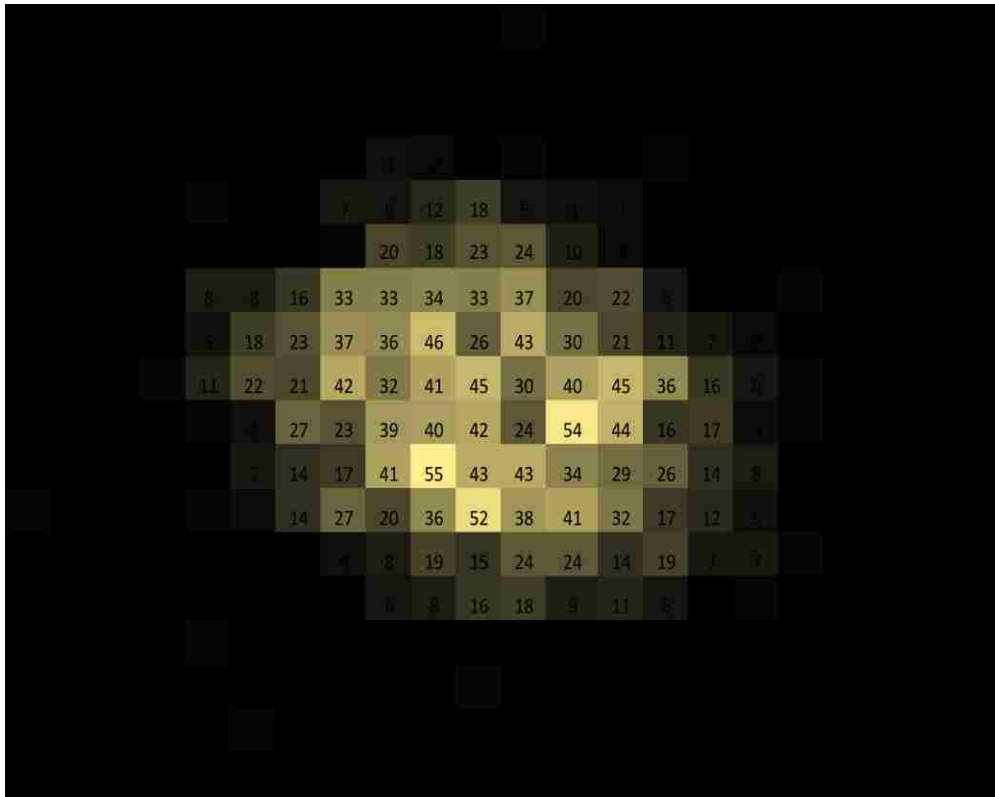
Figure 48: To characterize the activity distribution of the source, a 15 second per pixel image was developed with the source at the closest position, z=17 cm. The step size is 2 mm, though the nozzle collimator inner diameter is 7 mm.

3.4.2 Energy Discrimination

Detector software simply outputs the channel number vs. number of counts. This must be calibrated to energy to be useful for identifying unknown sources   At least two different spectral lines are needed to perform energy calibration but the more spectral lines that are used, the better the fit will be. Note that the energy calibration changes when the settings on the detector are changed, so the fit in Figure 49 is only applicable for those detector settings, which have been deemed as the optimal operating parameters.
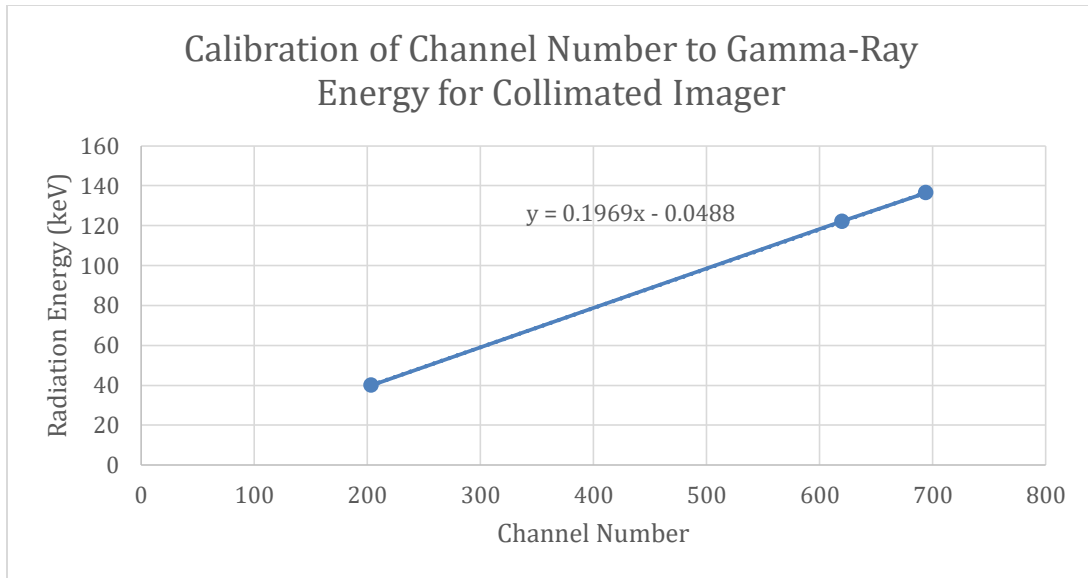
Figure 49: Channel to energy (keV) calibration for the collimated imager.

This calibration allows us to distinguish between sources of varying energies. Figure 50-52 shows how it is now possible to distinguish between a Co-57 and Eu-152 source which are placed next to each other but emit differing energies of radiation (Eu-152: 40.12 keV, Co-57: 122.06 keV).
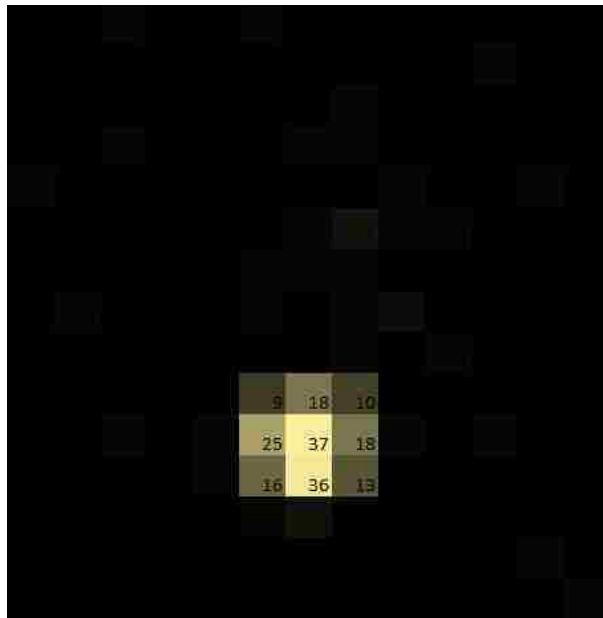
Figure 50: Eu-152 source imaged with Co-57 source; everything other than the 40.12 keV spectral line is being discriminated out.

63
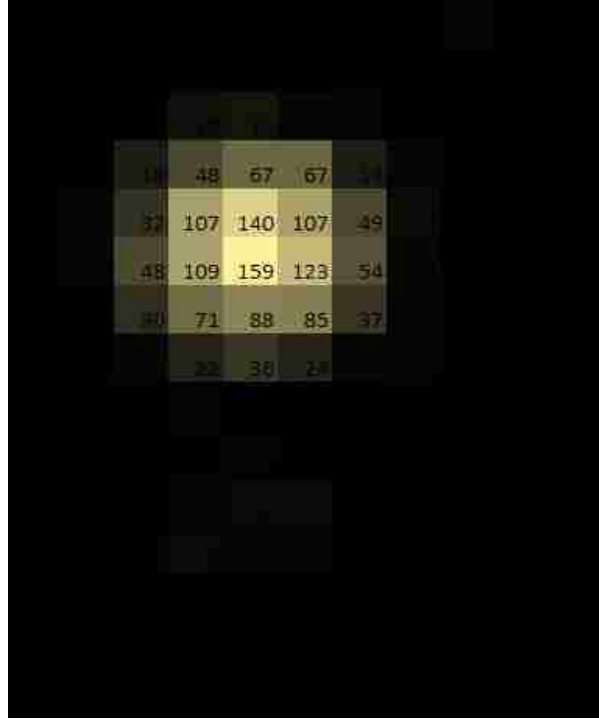
Figure 51: Co-57 source imaged with Eu-152 source; everything other than the 122.06 keV spectral line is being discriminated out
.
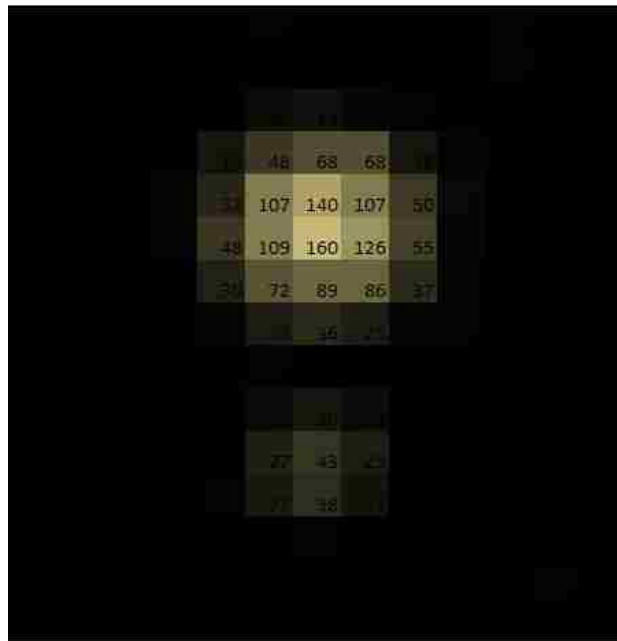
Figure 52: Image of both the Eu-152 source and Co-57 source as seen with no energy discrimination. Note that the Co-57 source has a higher activity so it appears brighter and is also a dispersed source so it appears larger.

3.5 Conclusion of Nozzle Collimated Imager

The nozzle collimated imager could detect and identify sources as well as create two dimensional images of their location. The system behaved as predicted by the governing mathematics and could be accurately modeled in MCNP. These simulations allowed for the production of a nozzle which was able to achieve less than 1 cm resolution at a source distance of 50 cm. Two different sources were identified and separated through post processing energy discrimination, proving the effectiveness of the analysis codes. The background in the experimental lab as well as the detector responses were well characterized. A shortfall of this design is the collection time. With only one detector stopping at each point the time for collection is compounded and for low activity sources at far distances collection times could run into the hours. The next step of this project will be using this detector as a proof of concept for a larger detector. This larger detector should decrease collection times and add functionality to the system.

4. Theory Validation and Characterization of Pixelated Detector

Pinhole requires large surface radiation detectors due to the spatial projection created. The detector should have position resolution. The large surface detector can be pixelated to create the image, which can be done in some detectors using an array of anodes to collect the electrons generated from radiation striking the material at specific locations. Kromek makes the D-Matrix Nuclear Imager, a CZT radiation detector made of larger CZT crystals with small, pixelated anode electrodes. The D-Matrix utilizes four CZT crystals, 1 cm thick, each having 121 anodes for a total of 484 pixels. Each pixel has an effective area of 0.2 cm giving the total detection area of 4.4 cm^2.

For pinhole imaging there are always three components, the source, the mask and the imaging plane. The source can be one or several point sources or spatially distributed. The mask can vary in thickness as well as the number of pinholes. The gamma rays emitted from the source are modeled as interacting on the surface of the detector but this is not usually the case, photons will penetrate some depth into the material before interacting. More details on the detector are presented in Section 4.3.

Before the D-Matrix was acquired for this project, preliminary work was performed with the Amptek detector using a copper plate with a single pinhole as a mask. The detector was moved to a series of different positions to effectively simulate a large area, pixelated detector. Calculations were also done to understand the expected image and noise that the detector would see for various mask materials and thicknesses.

4.1 Design

The D-Matrix detector can be made to utilize pinhole collimators to image radioactive sources at a distance. As mentioned above, the Amptek detector was also used to understand pinhole imaging, with the detector positions in different locations to simulate different pixel locations. A series of calculations, simulations, and lab experiments were performed to gain a better understanding of how the D-Matrix detector operates and responds so that proper design can be utilized in creation of the imaging system.

To start, shielding calculations were done for copper, iron, lead, and tungsten to find percentage of incoming gamma rays over the energy range of 1 keV to 1 MeV, that would be attenuated by 1 cm of material. Later other materials such as air, polyethylene, water and aluminum were added for comparison. The results of these calculations are shown in Figure 53 [43].
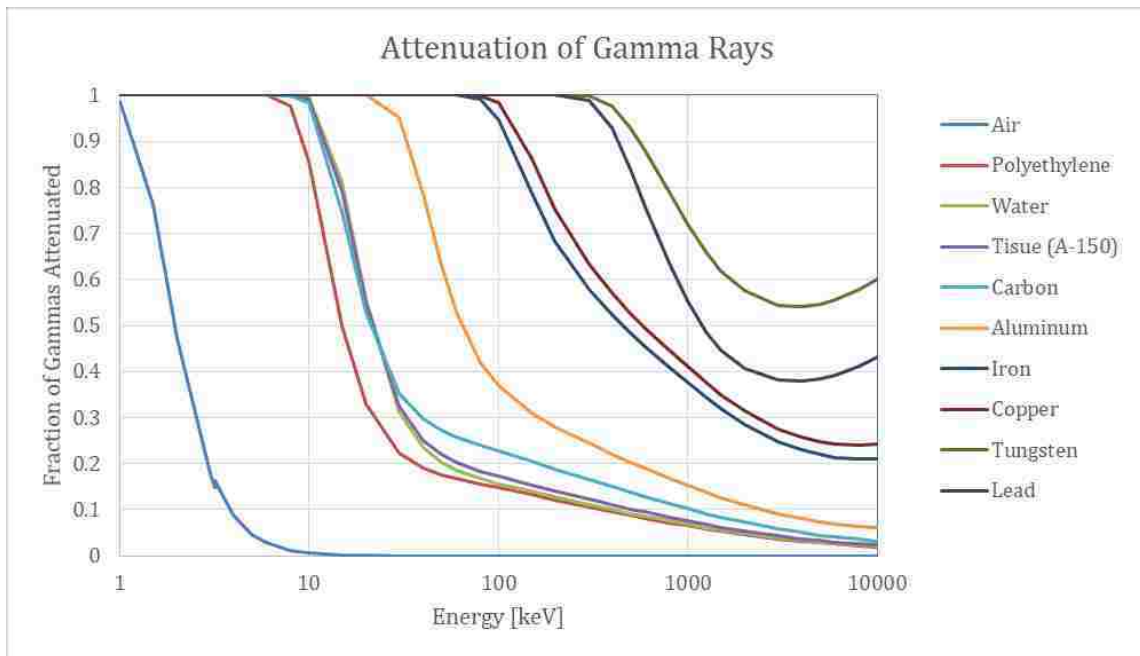
Figure 53: Fraction of gamma rays to be attenuated by various materials at varying energies.

There are simple optics equations which can utilized to gain a theoretical understanding of the optical resolution of a pinhole mask. Point sources are used in these calculations to simplify the equations. As we can see in Figure 54, by like triangles, the source-to-mask distance divided by the aperture is the same as the source-to-detector plane divided by the image size. Using the source-to-mask distance (SM) and the mask-to-detector distance (MD), for a total source-to-detector distance of SM+MD, and the pinhole size (a) and image size (I), the like triangles can be restated as Equation 14:

$$\frac{SM}{a} = \frac{(SM+MD)}{I} \qquad \text{or} \qquad I = \frac{a(SM+MD)}{SM} \qquad\qquad (14)$$
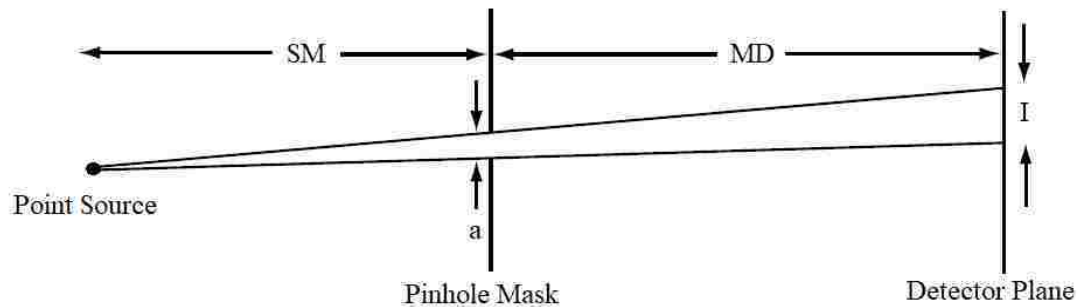
Figure 54: Basic dimensions of source, pinhole mask and detector. [44]

Equation 14 is known as the point response function (PRF). This equation shows how a single point in space will be projected onto an imaging plane. The smaller I is the sharper the resolution of the image, this can be done by decreasing a, increasing SM or decreasing MD. These changes have impacts outside of the resolution, most notably in efficiency. As a approaches zero size, I approaches a point on the detector plane, but also no source particles would be able to impact the detector. Since source particles are needed to create the image this is not physically possible. As SM increased the total

geometric efficiency of the system decreases due to only a finite number of particles being emitted from the source over a given amount of time.

A resolution of 1 cm, defined as FWHM, is desired so this can give baseline properties for our pinhole mask. Equation 14 assumes that the mask has no thickness, this is an acceptable simplification at large SM and MD values, small enough source offset, and with a thin enough mask. These assumptions and equations can be used for a preliminary mask design (further discussed in the Section 5.1) as well as produce a theoretical model to compare experimental data against.

Another equation can be created to determine the optimal multiple pinhole mask to use. Detectors have a limited size so the images projected must not overlap but the more pixels which are exposed to form an image, the better use of the detector and improved image resolution. Equation 15 relates SM and MD to the number of pinholes ($N_{pinholes}$), the size of the detector (S_{det}) and the desired field of view (S_{obj}). This equation was used to optimize experimental setups for varying conditions.

$$SM = \frac{(SM+MD)S_{det}}{S_{obj}\sqrt{N_{pinholes}}+S_{det}} \qquad (15)$$

4.2 Theory Validation

MATLAB was used to simulate the response of the detector shielded by a pinhole mask from a source. The program uses Monte Carlo techniques to generate gamma rays emitted from the source point which will then either impact the detector or be attenuated by the mask. The probability of these occurrences depends on the geometry/properties of the system: distances from mask to source, mask to detector, pinhole diameter, as well as

mask thickness and material. These simulations can be compared to lab two dimensional images simply by taking cross sections of the data as shown in the next section.

The gamma rays are assigned an angle at which they leave the source. For computational efficiency purposes, the angle is not isotropic but was a section of the isotropic emission in a cone directed towards the region of interest for the simulation, such as the pinhole mask. If a particle makes it through the pinhole it will impact the detector. If the particle impinges on the mask the probability that attenuation takes place is calculated using the thickness of the mask h and the attenuation coefficient μ. Equation 16 shows the probability that a gamma ray will travel through the mask un-attenuated and then impact the detector.

$$Prob = \ e^{-\mu h} \tag{16}$$

The probability of the gamma ray getting through is then compared to a randomly generated number between 0 and 1 and if this number is within the bounds set by Equation 16 then the particle is impacted on the detector along is original course. The location of this impact is added to a vector and once all particles have been run it is binned in a histogram. The plots generated using this method are seen in the next section when compared to experimental data.

4.2.1 Scoping Work with Amptek Detector

To simulate the multiple crystal lattice of the D-Matrix detector with the single crystal CdTe Amptek detector the scanning system from the previous project is used. The nozzle used for the last system was removed to more accurately represent the D-Matrix detector. If the Amptek detector is moved in steps that are the size of the crystal (5 mm)

we can effectively simulate an array of 5 mm x 5 mm crystals taking data at any location the scanning system can reach. This was not the same as the D-Matrix detector which has twenty-two 2 mm x 2 mm crystals which will provide a higher spatial resolution. The D-Matrix detector face is a fixed 44 mm x 44 mm whereas the Amptek setup can vary the effective size of the detection face.

Copper mask material was used in these preliminary tests due to the ease of machining copper and that it has relatively high gamma ray attenuation properties. The mask was 0.6 cm thick with a 1/8 in and 1/4 in diameter pinholes in different locations. The mask was clamped to the scanning system case to provide a consistent pinhole position throughout each measurement set. The source was then held by an optical mount with an adjustable height so the source could be moved relative to the imaging system, as shown in Figure 55.

Figure 55: Experimental setup to simulate D-Matrix detector.

For calculations, the 0.6 µCi Eu-152 source was used and approximated to be a point source. The reason that Eu-152 was used is the strong 40 keV spectral line which is

easily shielded by the mask and easily detected by the thin CdTe detector. At 40 keV it was seen that probability of a gamma ray being stopped by this thickness of copper is very close to 100%, so the copper was modeled as a perfect mask at this energy.

The single crystal detector simulated the array of detector crystals by stopping at adjacent locations for a set dwell time. This dwell time at each location would be taken as the time it would take for a lattice detector to produce that image. So the process for the single crystal detector took much longer than the array did which is a substantial factor for upgrading to an array crystal detector such as the D-Matrix detector.

The experimental data is collected and processed the same way that the original scanner data was. It is put into a LabVIEW array which is the exported to Excel where it can easily produce two dimensional images. The simulation which were built in MATLAB are only one dimensional to maintain simplicity for comparison to experimental data (appendix B). The main difference between the experimental data and the simulations is the shape and sometimes the location of the response functions, but the width is well represented. The simulation has a severe drop off while the experimental data has a more rounded response function. This could be due to multiple effects. In the simulation the edges of the mask are sharp, perfectly defined lines in space and the source is perfectly a point source, and these sharp edges show up very sharply in the results. Theoretical hand calculations are shown for the last two experiments.

The first experiment done was with the source against the face of the mask with both the 1/4 inch and 1/8 inch pinholes, Figures 56-59 detail the comparison between experimental and simulated results.
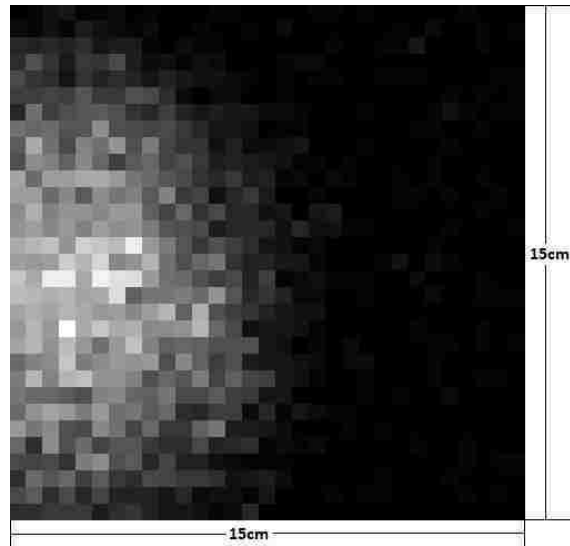
Figure 56: 1/4 inch pinhole diameter, source on mask face, 5 mm steps, scan of full 15 cm^2 area with 1 minute dwell time at each position.
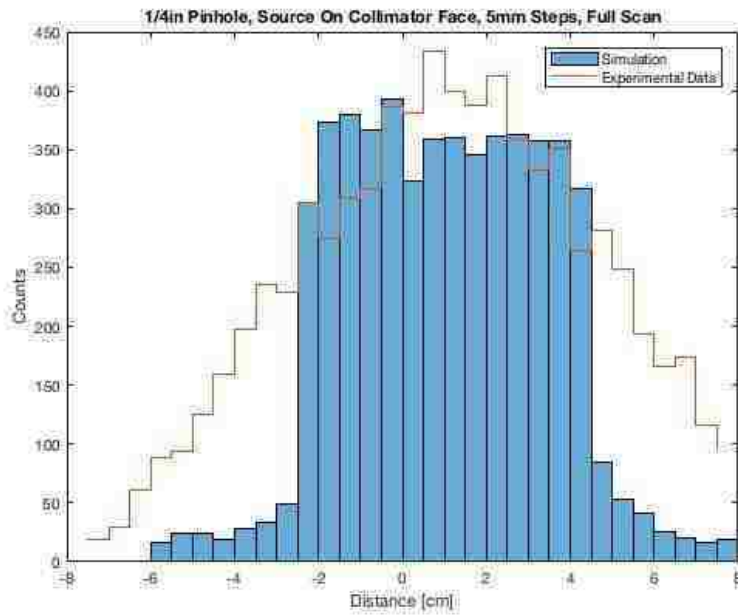
Figure 57: Comparison of experimental data shown in Figure 56 and MATLAB simulation with the same setup, slice along y-axis at source center.
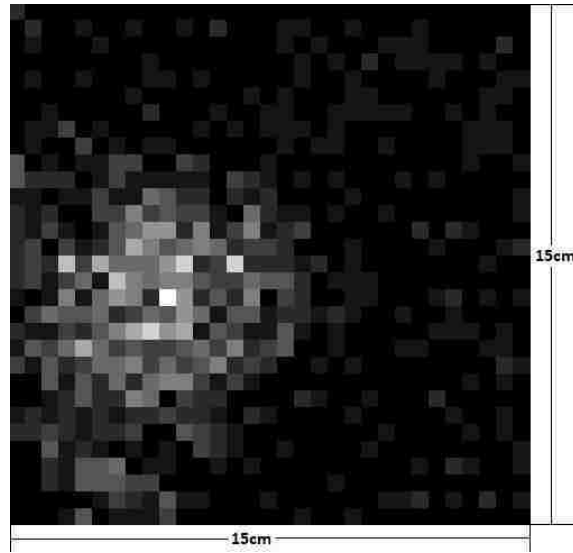
Figure 58: 1/8 inch pinhole diameter, source on collimator face, 5 mm steps, scan of full 15 cm² area with 1 minute dwell time at each position.
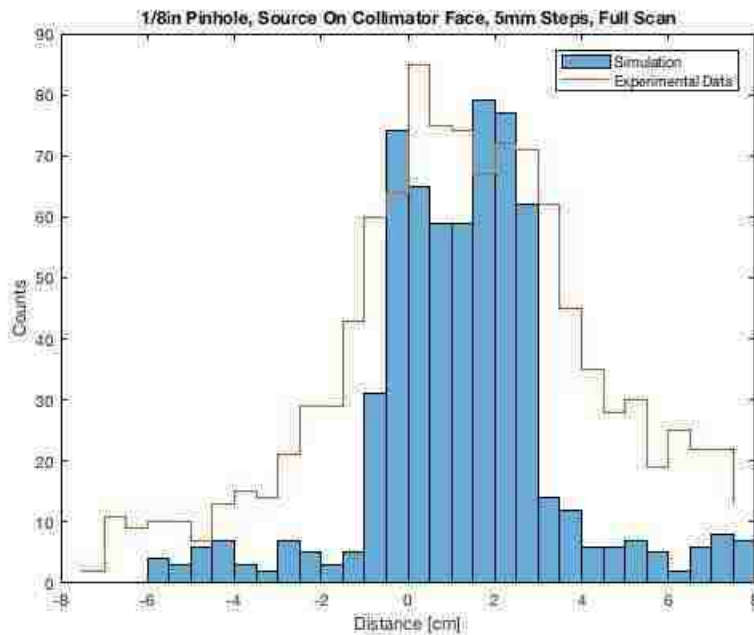
Figure 59: Comparison of experimental data shown in Figure 58 and MATLAB simulation with the same setup, slice along x-axis at source center.

Both these images are off-centered because at such a small source-to-mask distance even the smallest offset can lead to a large image displacement. This has no effect on the image resolution and is ignored. The approximate resolution using the 1/4 inch pinhole diameter at this source-to-mask distance is about 8 cm FWHM while the

74

resolution of the 1/8 inch pinhole is about 4 cm FWHM. A pinhole twice as narrow gives resolution two times narrower at the same source distance.

Next the source was moved to a distance equal to that of the mask-to-detector distance, 16 cm. Figures 60-62 show the results of that test. Figure 60 is the full image that the detector saw, Figure 61 is the simulated response and Figure 62 is a comparison of responses along the x-axis and y-axis with the calculated theoretical response.
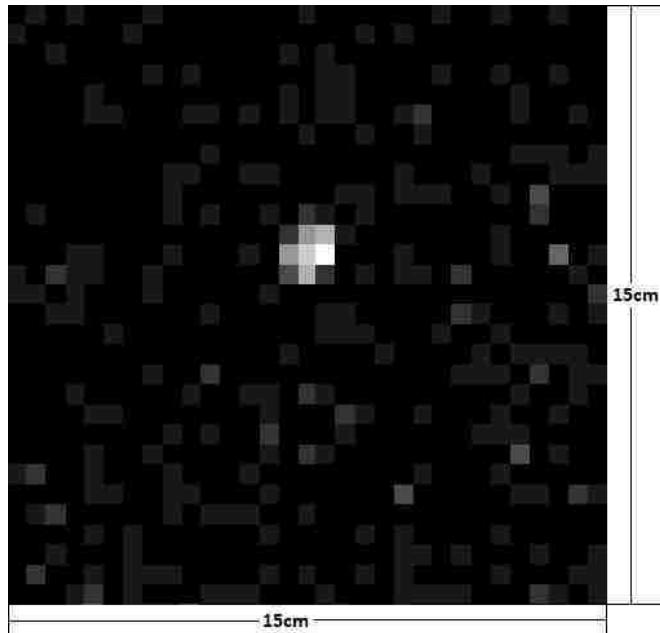
Figure 60: 1/4 inch pinhole diameter, source 16 cm from mask, 5 mm steps, scan of full 15 cm x 15 cm area with 1 minute dwell time at each position.
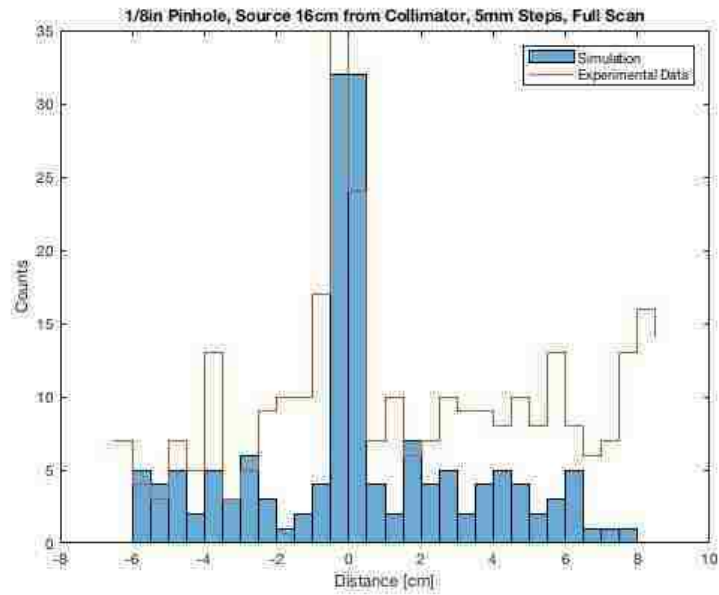
Figure 61: Comparison of experimental data shown in Figure 60 and MATLAB simulation with the same setup, slice along x-axis at source center.
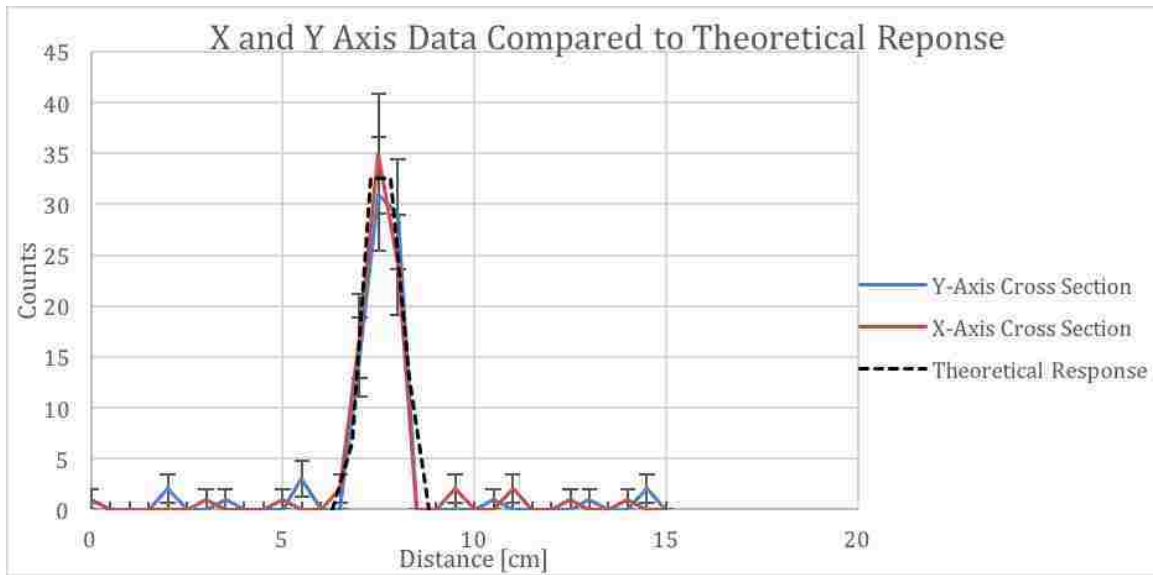
Figure 62: Comparison of x and y axis responses with theoretical response for Figure 60, slice along x/y-axis at source center.

The experimental and theoretical resolutions match and are about 1 cm at the

FWHM. Figures 63-65 show this same experimental setup but with 1 mm steps. The

theoretical response was calculated by using Equation 14 to find how large a point source

image would look on a detector.

76
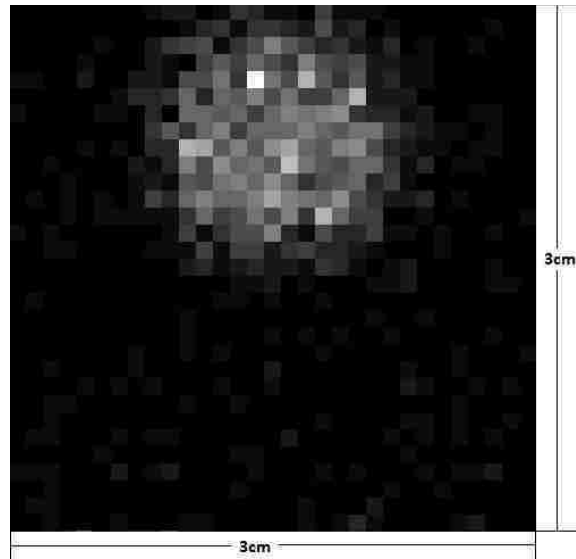
Figure 63: 1/4 inch pinhole diameter, source 16 cm from mask, 1 mm steps, scan of full 3 cm x 3 cm area with 1 minute dwell time at each position.
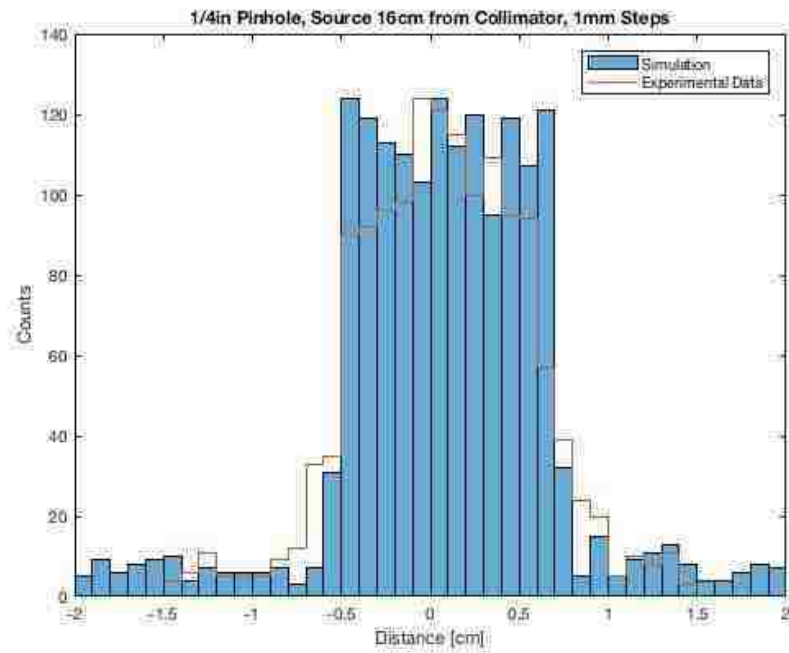
Figure 64: Comparison of experimental data shown in Figure 63 and MATLAB simulation with the same setup, profile slice along x-axis at source center.
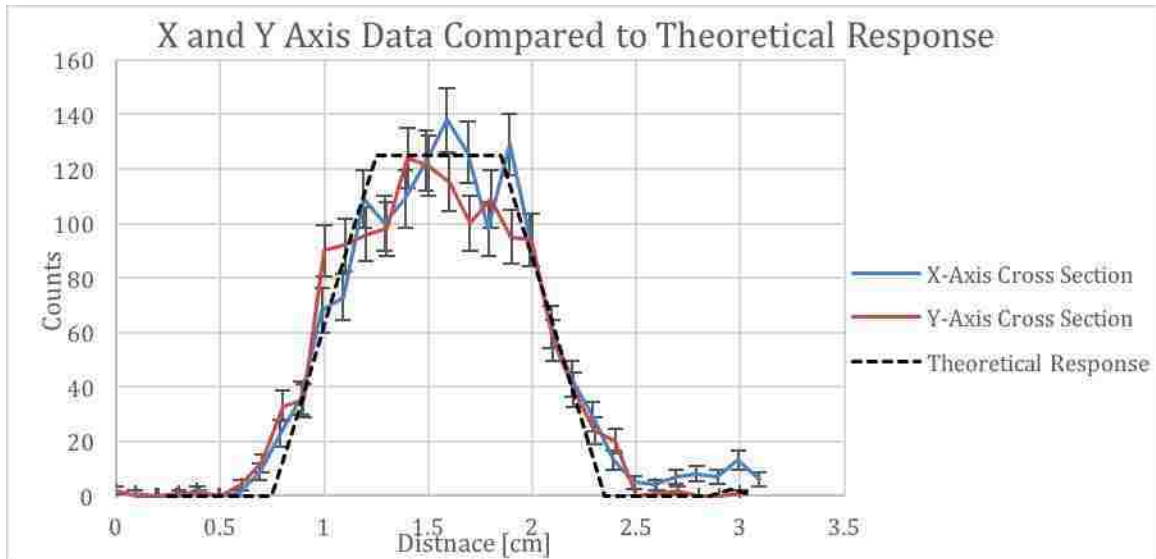
Figure 65: Comparison of x and y axis responses with theoretical response for Figure 63, a profile slice along x/y-axis at source center.

As the source-to-mask distance is increased, the resolution gets sharper. However, the efficiency decreases too, it will be up to us to determine optimal measuring distances for balancing both resolution and detector efficiency. The figures show the response from the experimental data, along with MATLAB simulations, and hand calculations. The simulation begins to agree with the experimental data more as the source distance increases. With varying pinhole size, the image size changes accordingly. Changes are also seen from varying the distance between the source and mask. These factors can now be applied to the D-Matrix imaging system.

4.3. Detector Characterization

The detector that is used for these experiments, a Kromek D-Matrix, needs characterization to understand the response obtained and how that effects the images produced. The spectra obtained from the detector are analyzed and energy discrimination methods are applied to reduce noise and to identify the source being imaged. The individual pixel responses must be note under controlled conditions so that when images are produced certain variances can be accounted for. The size of the single pinhole used is varied to explore the tradeoffs between resolution and efficiency.

4.3.1 Detector

The Kromek D-Matrix gamma imager features a 19.36 cm^2 CZT crystal imaging area in an aluminum housing with a carbon fiber window above the detector. The detection area is comprised of four separate square CZT crystals, known as modules, each measuring 2.2 cm on a side. The crystals are butted together to form a larger square of 4.4 cm x 4.4 cm. These crystals each subdivided into an array of 11x11 pixels by a pixelated anode placement, for 121 pixels in each crystal. Summed, that is 484 pixels with an operating area 4.4 cm on a side. Each pixel can produce energy spectra as if it were an individual detector, though there is an expect signal bleed between pixels due to the pixel being a part of the larger crystal, and slight edge effects as charge sharing between pixels is necessarily different there. Figure 66 shows the dimensions of the full detector.

Figure 66: Dimensions of D-Matrix detector.

It should be noted that that the D-Matrix detector was not functioning properly when given to UNM, and the included software was out of date. Both situations limited the proper full testing and characterization of the detector due to time constraints they placed on the project.

The D-Matrix software does not come with a way to analyze spectra it produces so as a part of this research project an analysis code was written in MATLAB (Appendix C). This code organized the data by pixel and then by channel counts which each pixel saw thus generating a series of 484 separate spectra which could be examined and analyzed individually. This program also produced an excel spreadsheet in which all 484 pixels counts were summed individually and shown as a heat map representation of the detector over a selected energy range, which are the images seen in this report. To characterize the system, we performed tests on spectrum characterization - to understand the energy calibration and efficiency curve. Heat map tests were done to understand the

relative response over the face of the detector, and background characterization.

4.3.2 Spectrum Characterization

Spectra produced by the D-Matrix CZT detector system were very similar to those produced by the Amptek CdTe detector. Figures 67 and 68 shows Co-57 and Eu-152 spectra respectively along with the calculated FWHM values at the varying energies.
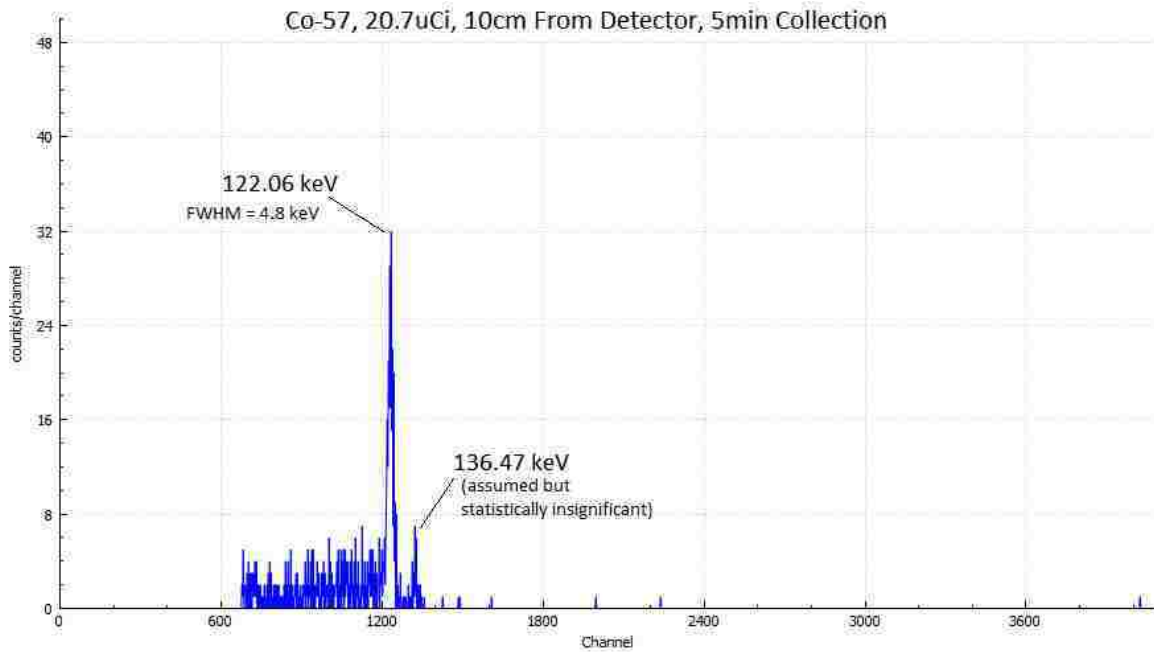
Figure 67: Co-57 spectra from the D-Matrix.

81
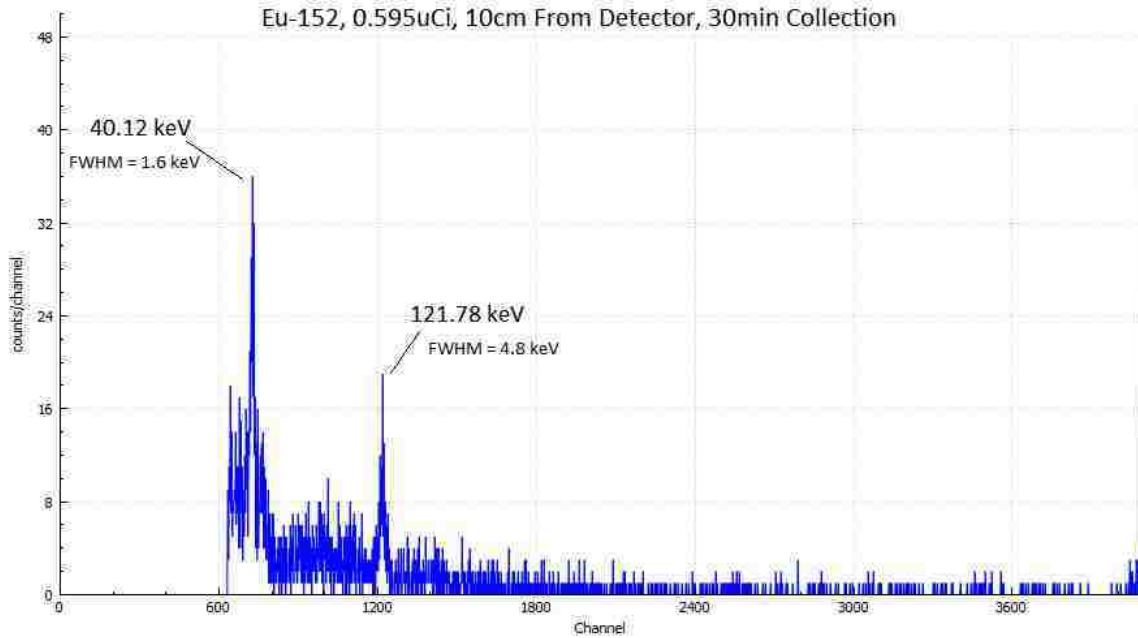
Figure 68: Eu-152 spectra from the D-Matrix.

Energy calibrations were performed. The D-Matrix system produces 484 pixel spectra and performing this calculation for every spectrum is unreasonable so for this purpose a pixel whose spectra was clear and easily readable is given to show an example of this relationship. The problem of dealing with each individual pixel was addressed later. The sample relationship for energy calibration is shown in Figure 69 where radiation energy is plotted vs the channel number at which that energy appears in the detector. This can be used to create a linear fit equation to extract gamma ray energies from the detector.

82
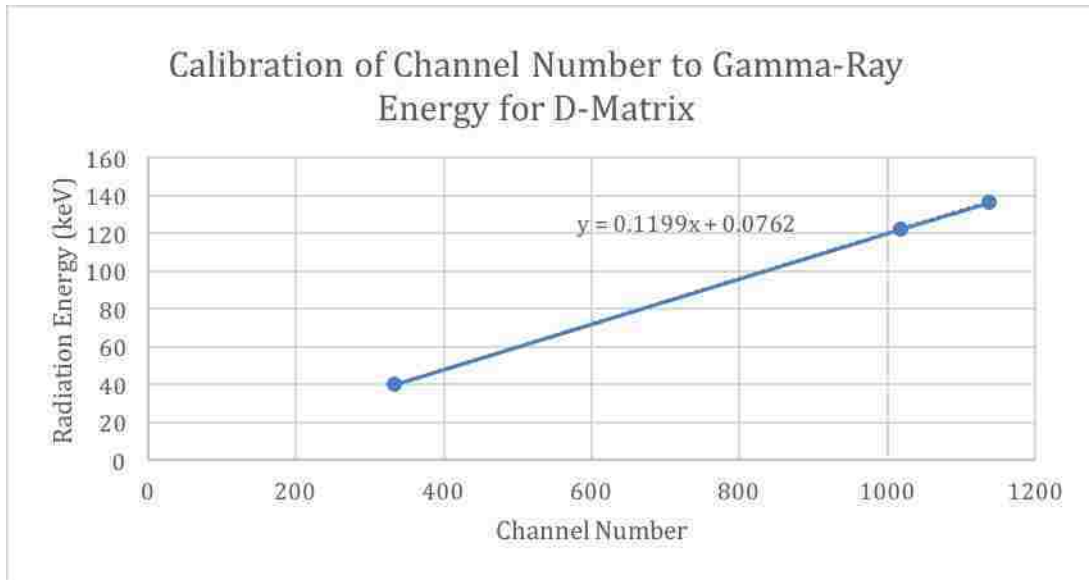
Figure 69: Channel to energy (keV) calibration for a single pixel of the D-Matrix system.

Radiation detectors have different responses to different energy gamma rays. Low energy gamma ray might not penetrate to the active region of the detector while high energy gamma rays might pass through the detector without depositing its full energy, so the efficiency curve must be understood. Three sources were used to create the curve in Figure 70, Co-57, Eu-152 and Ba-133. This shows a relatively flat efficiency curve near 100 keV, peak near 100 keV, which drops off slightly on the low energy side to 40 keV. On the other hand, the peak at 344.3 keV has a much lower efficiency.
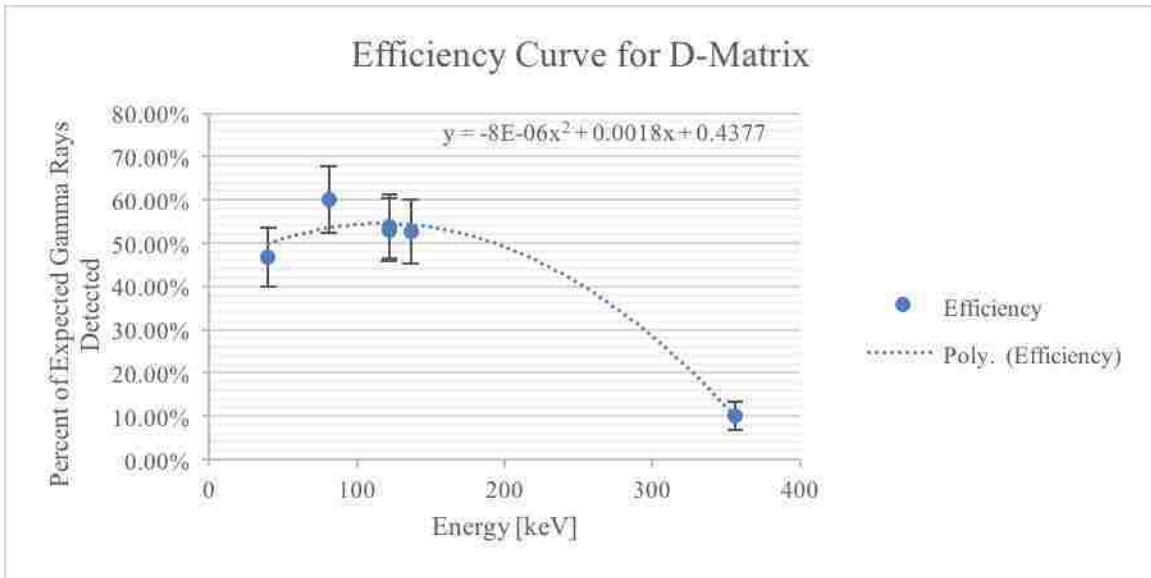
Figure 70: Efficiency curve for the D-Matrix detector.

4.3.3 Heat Map Characterization

Subsequent tests involved the detector response as a whole to both background and a source. Figure 71 shows the full spectrum summed counts from each pixel of the background radiation over 30 minutes. Lighter colors represent higher numbers of counts. Figure 72 shows counts for a Co-57 source centered over the detector with no collimation, 20 cm from the detector.
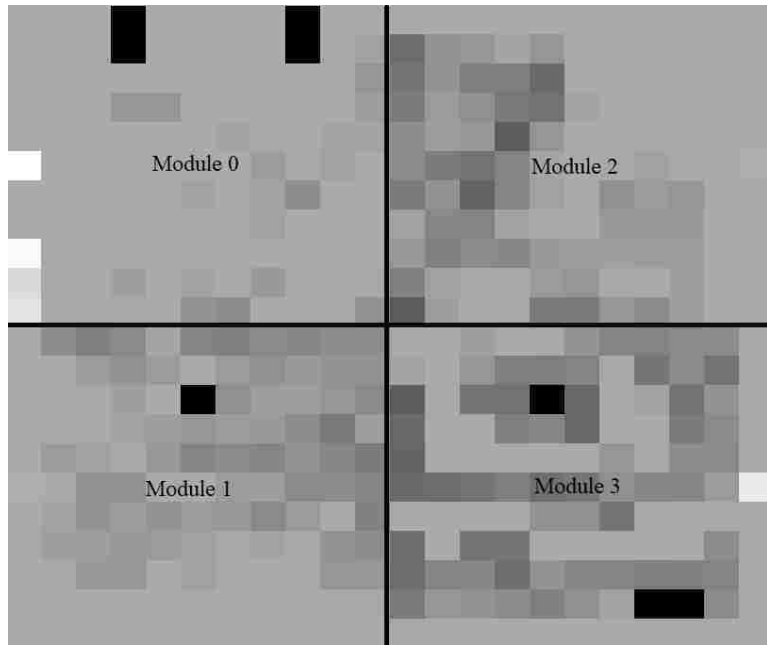
Figure 71: Heat map of D-Matrix response to background.
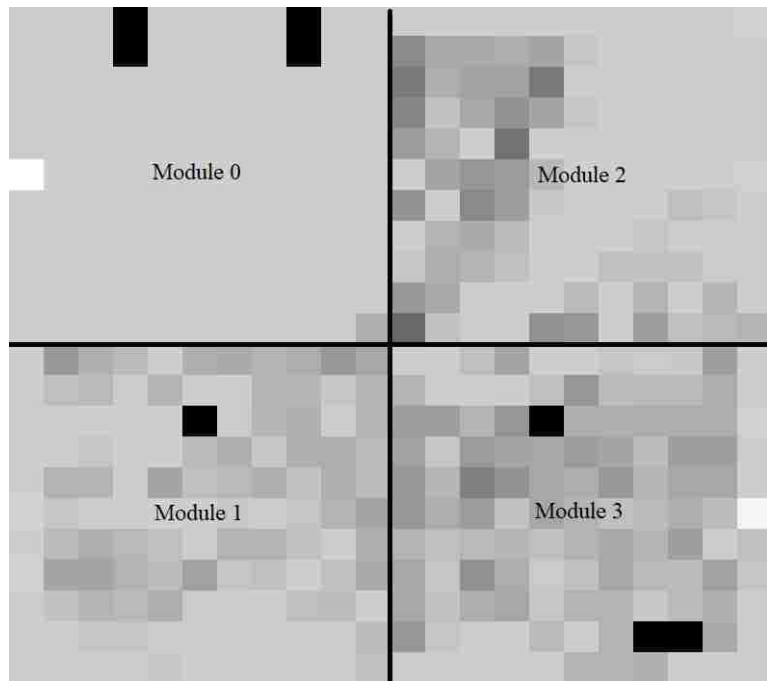
Figure 72: Heat map of D-Matrix response to Co-57 source placed on detector face.

First it is evident that even in a radiation field most of the pixels responses tend to be similar. Certain pixels always obtain higher or lower than average counts in both background and in the presence of a source. There are eight pixels not receiving any

counts, this was noted by the technicians at Kromek and deemed as non-functional pixels. They are the pixels showing up as purely black. Next, there are 2 pixels which are white (receiving more counts than average) in both cases. These are pixels which we deemed to be non-functioning crystals ourselves because in every situation these crystals produce an excess amount of counts. These pixels were turned off from data acquisition so that they did not create abnormal signals. It is also evident that there is a difference in response from module to module. The difference between module 0 (upper left) and modules 2 and 1 (upper right and bottom left respectively) is very distinctive. Finally, a ring can be seen around the edge of the entire detector. These crystals appear to be consistently obtaining higher counts than average, which may be due to not having to share charge with a neighboring anode beyond the edge of the detector.

An interesting time dependence to the detector background count rate was noticed and is shown in Figure 73. When the detector was first turned on, certain pixels - most notably in module 1 - were firing faster than average, represented as lighter pixels in Figure 73 (left). As time went on they faded closer to the average but never reached equilibrium with other pixels, see Figure 73 (middle) and (right). Fortunately, this noise appears in the spectrum only in lower energy channels away from any source energies of interest. This means that by using spectral gating this artifact can be removed from images.

Time = 0min   Time = 30min   Time = 60min
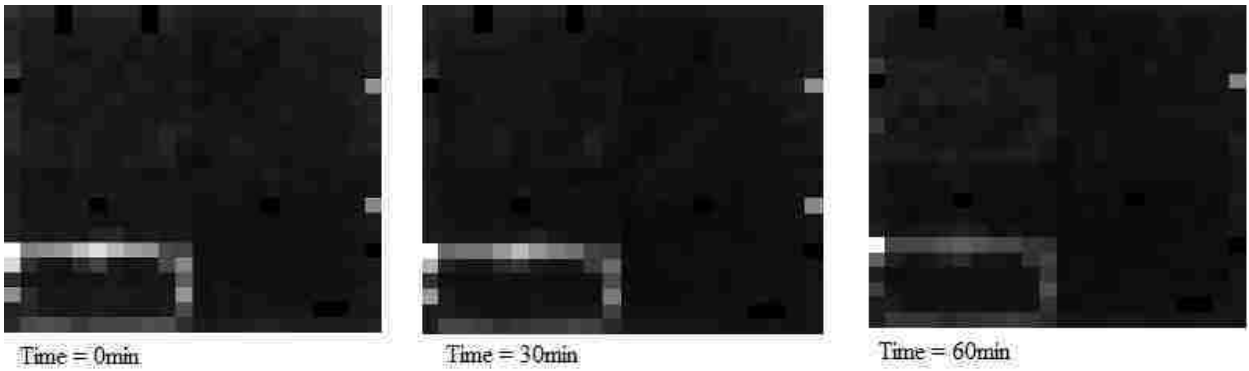
Figure 73: Change of detector response to background over time.

A function of aggregate background counts from the whole detector vs. time was created. Figure 74 displays how the relation drops quickly within an hour but then continues to fall slowly over the course of a day. So, when we performed measurements we let the detector warm up for at least an hour before acquiring data.
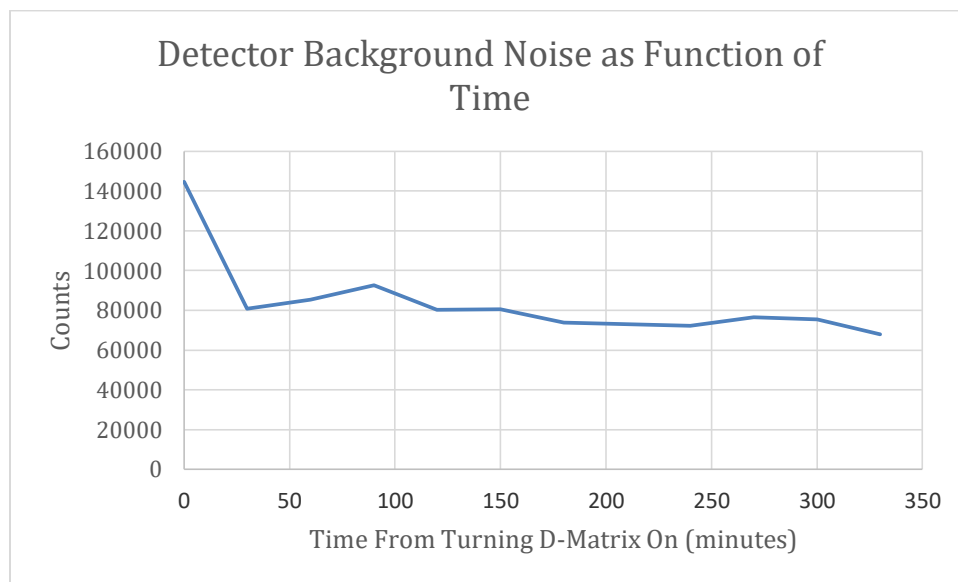
Figure 74: Detector aggregate counts over time.

Imaging was first performed with the single pinhole copper mask from the moving Amptek detector tests. The initial test was to image the Co-57 source at a distance of 2 cm from the copper mask using the 1/4 in pinhole located directly above the center of the detector for 30 minutes. The results from Figure 75 show that there was an

87

uneven response between the modules, most notably, in module 3. Due to the hardware and software interface of the detector it was not possible to change the gain on individual modules. There is also still a noticeable response so images can be produced.
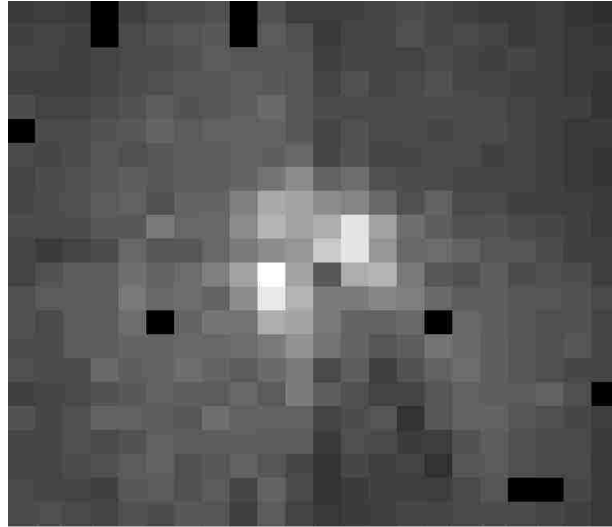
Figure 75: Image of Co-57 source directly above center of detector with 1/4 in pinhole.

The next figure shows 4 separate tests runs in which the pinhole and source were placed above and centered on a single module for the same amount of time and same distance from detector to source. The source was Co-57 and the pinhole was 1/8 in.
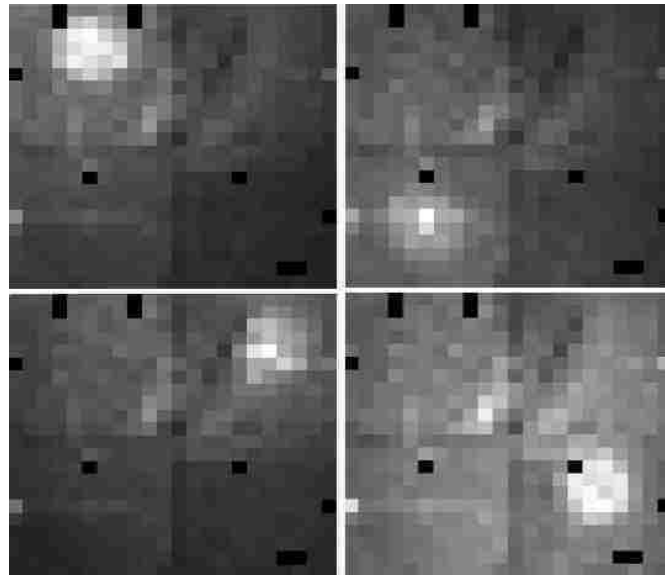
Figure 76: Separate images taken with source centered above each module individually. Top left: module 0. Top right: module 1. Bottom left: module 2. Bottom right: module 3.

Comparing the four quadrants with the source over each one, we can assemble an image, Figure 77, which shows the relative module response to the same radiation field. Module 3 has the overall weakest response.
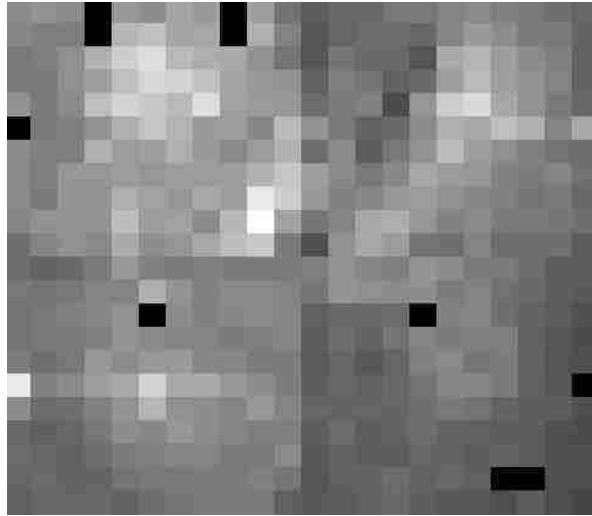
Figure 77: A composite of all four module's responses to the source.

While these figures showed an image of the source, a circular disk, the response is not as clear as would be hoped. Two possible sources for this unclear response are radiation penetrating the pinhole mask, and detector counts from other energies not of interest. The mask used in this test was copper, copper is a good shield for low energy gamma rays but the attenuation coefficient begins to drop off with increasing energy at around 100 keV (see Figure 53). A better pinhole material is needed. For the second issue, detector counts outside the energy range of interest could be eliminated by an energy discrimination program which would only allow for the energy of interest to contribute to image counts.

4.3.4 Spectral Energy Discrimination

From initial tests it was determined that a process of energy discrimination was necessary to count only relevant photon energies from the source and not count background, to improve the signal-to-noise ratio and improve imaging contrast. Figure 78 shows a 16 pinhole mask when the raw counts of every channel were taken to make the heat map. Most of the information in this image would be useless. There are about four shapes visible, but their exact shape is indeterminate due to the amount of noise in some pixels compared to others.
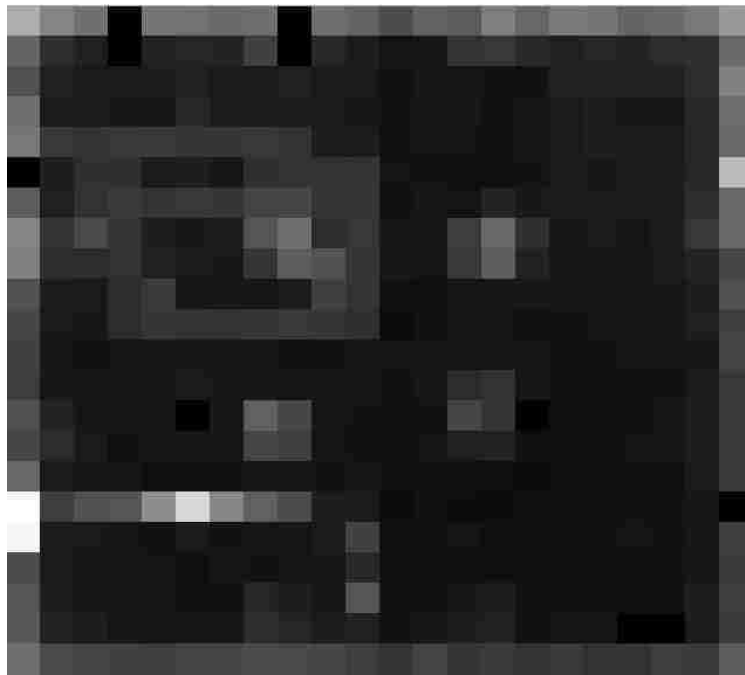
Figure 78: Image without energy discrimination.

A MATLAB code was written using "method one" from Section 2.3.3 and shown in Appendix E, so that it would only look at the counts between a block of channels for every pixel that corresponded to a known gamma ray energy. This was a simple but imperfect way to discriminate out noise which is not in the same region of channels as the peak of interest. For Co-57 the peak of interest is the 121.78 keV peak due to its

prominence and the relatively low background at that energy. "Method one" for energy

discrimination is not ideal because there are variations between each pixel which can lead

to peaks of the same energy occurring at different channels so a wide gate must be set.

Despite these issues, Figure 80 shows that this simple technique greatly improved our

image from the raw data. This image is from the same data set as Figure 78 but Figure 79

shows the results after energy discrimination. There are 16 shapes which are clearly

separated and some even resemble triangles. These were created by a pinhole mask that

had a separation of 1.1 cm, a pinhole diameter of 0.1 cm and a thickness of 1/8 in.
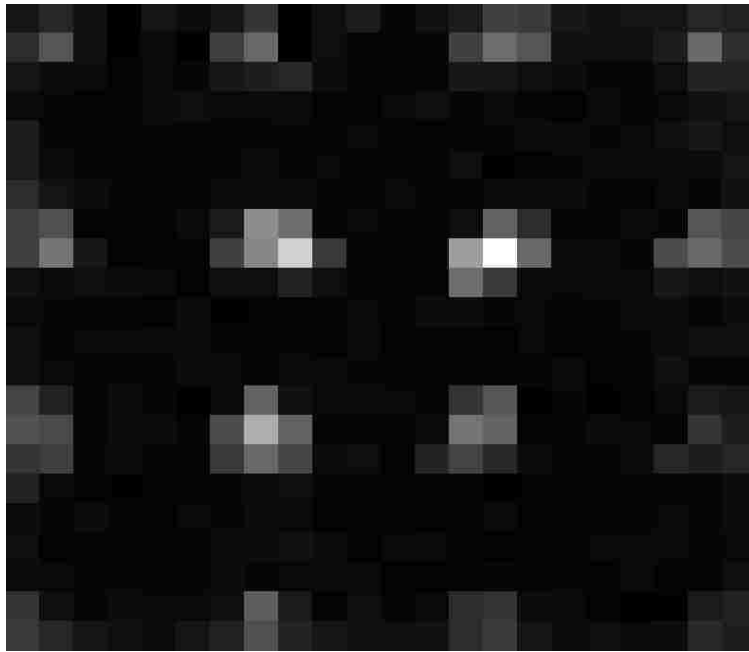
Figure 79: Image with "method one" energy discrimination.

Those images also show that the discrimination was working but there was room

for improvement. A way to increase the effectiveness of the discrimination would be

peak finding and further background subtraction. The MATLAB code was modified

again to now utilize "method two" of background subtraction, described in Section 2.3.3.

The same raw data from Figure 78 is now shown in Figure 80 using "method two" of energy discrimination.
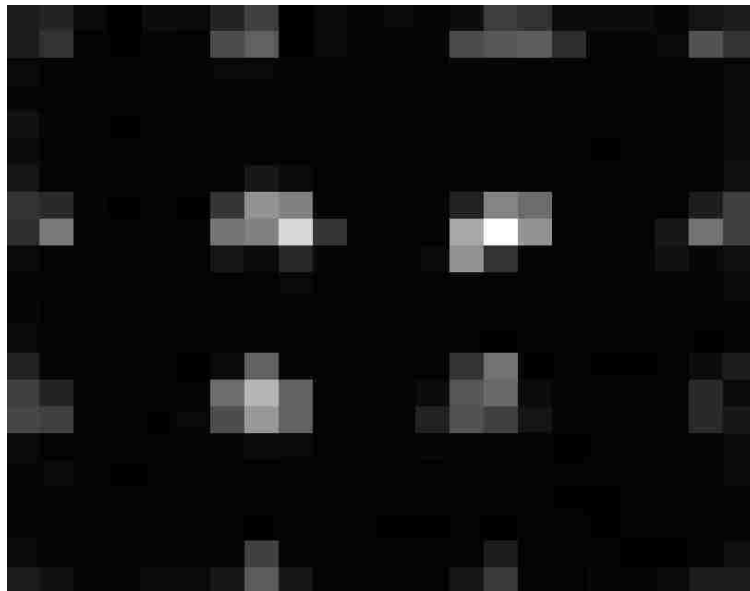
Figure 80: D-Matrix data using "method two".

Differences between Figure 79 and Figure 80 are hard to distinguish just by viewing the heat map representation. Figures 81 and 82 are the cross sectional detector responses as using "method one" in Figure 79 and with "method two" in Figure 80.
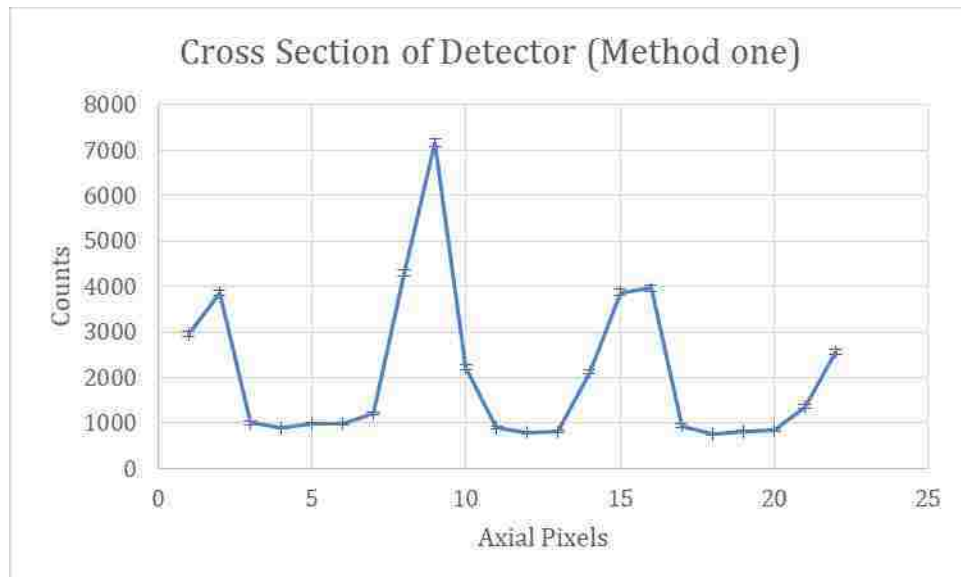
Figure 81: Cross sectional detector responses using "method one".
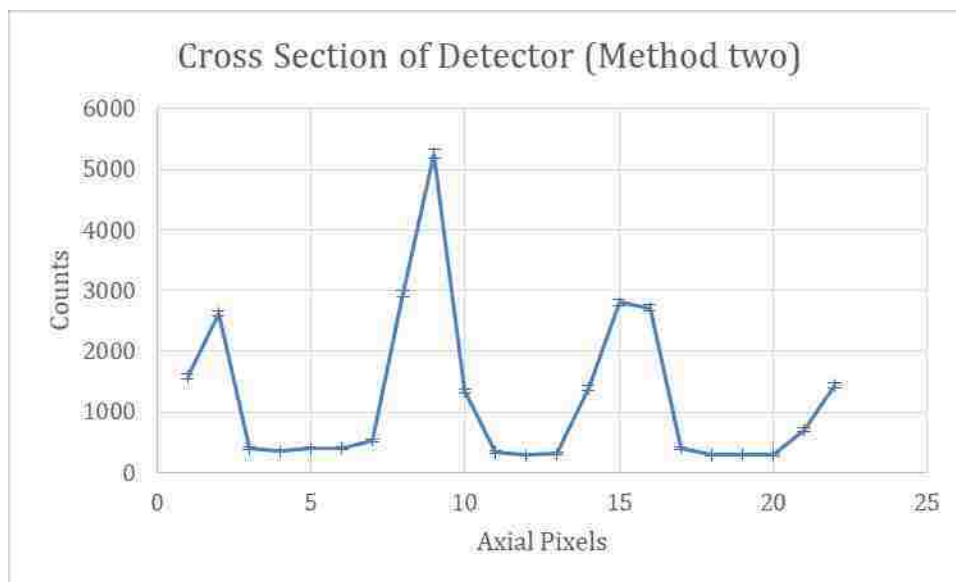
Figure 82: Cross sectional detector responses using "method two".

While the shapes are the almost the same between the two figures, the background is more suppressed using "method two". The peak to trough height in Figure 81 is 7.99 while the peak to trough height in Figure 82 is 14.95. This means that there is less noise and better contrast using this "method two" which will allow better image resolution at further distances as well as improved signal to noise in subsequent image reconstruction.

4.3.5 Distance and Detector response

As a source moves further away the signal response becomes smaller and the more likely it is that the source will not be distinguishable below background. The distance at which the source becomes undistinguishable is a variable of the source strength and the measurement time. The source used in these experiments is a 3.67 µCi Co-57 source which has equivalent gamma ray intensity to about 2.5 g of U-235 (with no self-shielding), when looking at the 122 keV line from Co-57 and the 186 keV line from U-235. Figure 83 shows how the response from the detector changes as a function of

93

distance the source is from the detector over a 10 minute run time. The mask-to-detector distance is kept at a constant 2 cm and only the source-to-mask distance changed.
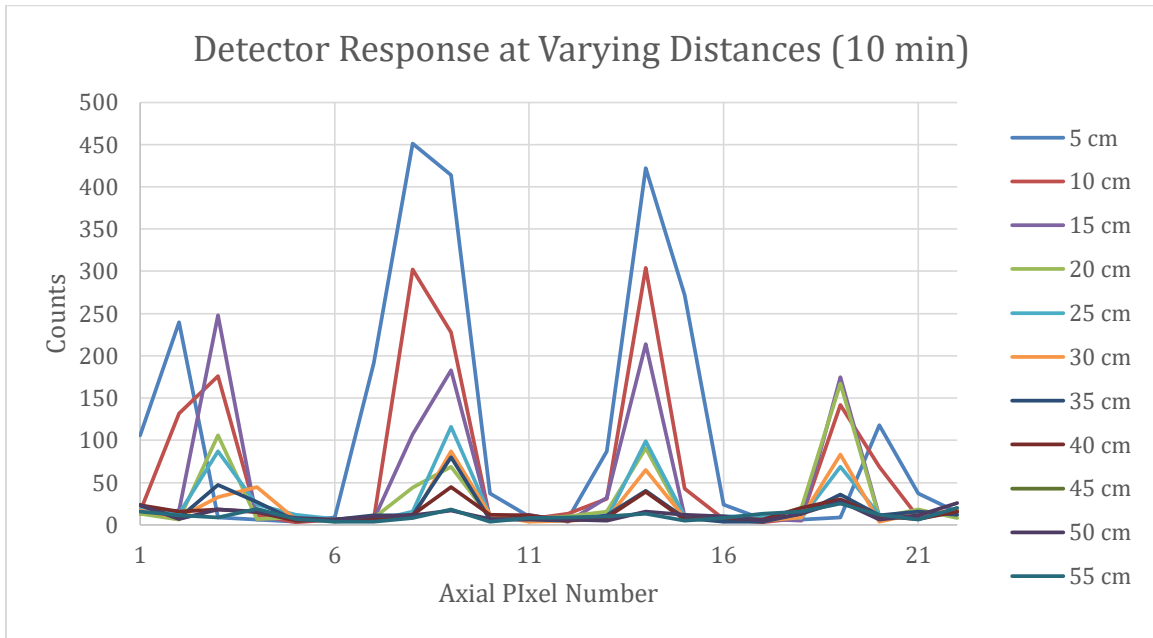
Figure 83: Detector response at distances up to 55 cm.

It is interesting to note that as the source gets further away the responses from each of the sub-images becomes more equal, this is due to the source being cut off a low source-to-mask distances or high angles through the outer pinholes. The source signal is statistically significant, according to Equation 7, until 45 cm. For any distance longer than 45 cm a source of this strength would require a longer collection time.

4.4 Conclusions of Validation and Characterization of Pixelated Detector

The design of the detection system as well as validation of the proposed mathematical descriptions and characterization of the pixelated detector response was successful. Starting with the study of the attenuation of gamma rays and a selection of lead as the mask material which would be applicable for this system. The study of the

point response function, Equation 14, gave us an idea of the effects of pinhole size, source-to-mask distance as well as mask-to-detector distance on the resulting image from a point. These factors all must be balanced so that a sharp resolution image can be generated while retaining an efficiency which does not impede system performance. Equation 15 helped with the design of multiple pinhole masks to choose parameters when setting up the experiment so that detection area usage could be maximized. Modeling of a single pinhole system was done with a Monte Carlo based MATLAB code. This code was then compared to one dimensional cross section of experimental results generated by converting the nozzle collimated imaging system into a pinhole imaging system. The simulations as well as the mathematically theory agreed well with the experimental results.

The Kromek D-Matrix was then acquired and characterized. First the spectra were analyzed and it was noticed that not all 484 pixels responded in the same way with respect to spectrum channel location. This variation was slight and nullified using the spectra finding and background subtraction method of "method two" described in Section 2.3.3. An efficiency curve was generated for the detector showing how the response varied with respect to the energy gamma ray. The full detector heatmap was response was then studied. This proved to result in varied responses over time from when the detector was turned on, over the four different modules of the detector and each of the pixels had widely varying responses as well. There was no way to account for these factors in a meaningful way. Luckily, when energy discrimination "method two" was applied to each of the spectra from the pixels the resulting heatmap were much more uniform. Large variances from pixel to pixel were minimized and module wide artifacts were negated.

The signal to noise ratio was also increased by applying "method two" so this allowed for the images to come across as stronger on the detector. With the detector well understood the study of varying masks, experimental setups and image reconstructions could be begin.

5. Pinhole Imaging

5.1 Pinhole Masks

To behave like optical pinholes, the pinhole masks should allow radiation through only the hole and not through the solid material. This though produces a trade off as thicker material will attenuate photons impinging on the solid mask material but will make the aperture thicker and limit angular acceptance. It was determined that lead was the optimal mask material due to its cheap cost, ease of machining and effectiveness at shielding gamma rays, and thus we could use thin sheets and reduce angular acceptance issues. We only need to shield a range of gamma ray energies due to the energy efficiency response of the detector itself. Gamma rays of high enough energy to efficiently pass through the lead would also pass through the CZT crystal without interacting or without depositing full energy, as shown in the following measured efficiency plot, Figure 84. This is not an optimal situation because that means that the gamma ray, even though geometrically hitting the detector, is not being properly counted, but appropriate for low energy imaging. This must be considered when choosing the thickness of lead which is to be used as a mask and reduces the need for very thick lead as the interaction efficiency in the detector falls for the higher energy gamma rays.
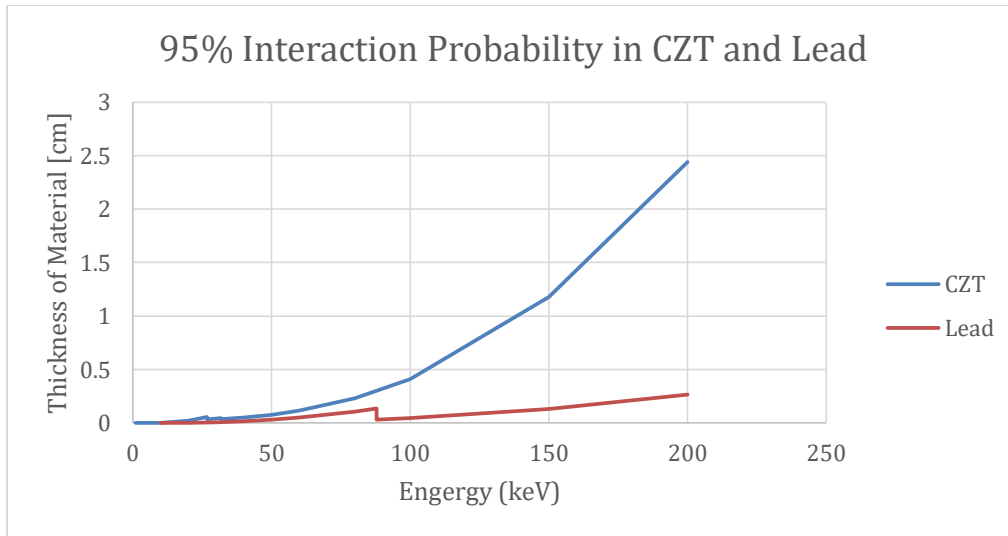
Figure 84: Thickness of material required for have an interaction probability of 95% with CZT and lead.

The ideal situation would be for both lead and CZT to have high interaction rates at high energies, instead CZT starts to require more material for a high interaction probability, which follows an energy dependent exponential function at these low energies. A standard thickness of lead of 1/8 inch (0.3175 cm) was chosen to be the thickness of the mask because it blocks out the majority of all gamma rays in these low energies of interest, which are 40 keV fromEu-152 and 122 keV from Co-57. This thickness was changed on some experiments to attempt to approximate infinitesimally thin mask used in some simulations.

Masks have four variables which effect the imaging of a material: number of pinholes, diameter of pinholes, separation between the pinholes and thickness of the mask. The image is further determined by the source-to-mask and mask-to-detector distances. The number of pinholes thought to be optimal was 16 because this would allow for a relatively high geometric efficiency as well as high resolution while utilizing the entire detector. Any more pinholes would risk overlap between the subsequent images - the regime of coded aperture imaging. On the other hand, fewer pinholes would negatively

98

impact geometric efficiency and effective use of detector imaging area. In Practice, the number of pinholes can also be decreased simply by centering the plate differently and covering up unused pinholes, so it is best to get masks with many pinholes machined. Based on previous simulations and calculations a pinhole diameter of 0.1 cm was chosen for initial experiments, but other diameters were produced. A diameter of 0.1 cm gives a theoretical spatial resolution sharper than 1 cm for all but very large, and often impractical mask-to-detector lengths. The distance between the pinholes of 1.1 cm was decided upon initially as well, as this would allow space between the images as well as effectively use imaging space. This was later decreased to more effectively use the detector space. Finally, a thickness of lead of 1/8 in (0.3175 cm) was chosen for initial experiments because that thickness of lead blocked close to 100% of all gamma rays in the energies of interest. 1/16 in of lead also worked over the energies of interest, blocking upwards of 95%. The thicker the lead the better the attenuation but the lower the angle of acceptance so thinner masks were made to try and find a balance between gamma ray attenuation and acceptance angles. The angle of acceptance is not as much a concern for point sources near the centerline of the mask, but it is important for imaging distributed sources. Figure 85 shows how the maximum angle of acceptance of a 0.1 cm pinhole changes as the thickness of the mask is increased, with 0 degrees being a ray perpendicular to the mask face. The angle of acceptance very quickly drops off to about 50 degrees at 2 mm thickness. The pinhole imaging may still be useable for a distributed source object for a mask several millimeters thick, but the source size accepted is strongly reduced after that
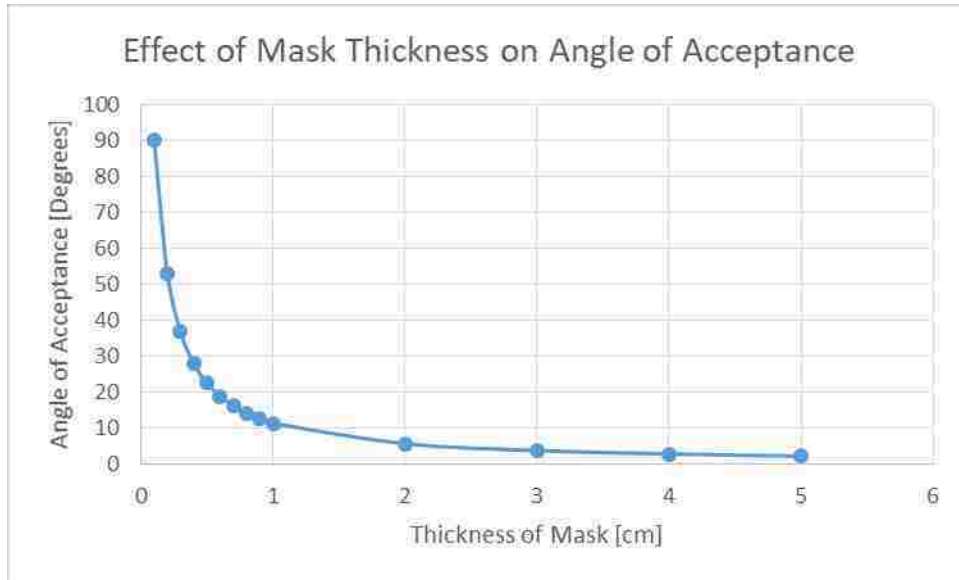
Figure 85: As the mask becomes thicker the angle of acceptance of the pinhole decreases.

The space between images and use of detector space is also a function of mask-to-detector distance as well as source-to-mask distance which was varied to examine image response be easily manipulated. Factors such as pinhole diameter and center-to-center spacing, the pitch, must be taken into account in broad sense. Once the mask is drilled it these are permanent fixtures of the mask and so several mask options were machined, a selection of which are shown in Figure 86. Table 3 shows the variations between all the masks that were designed.
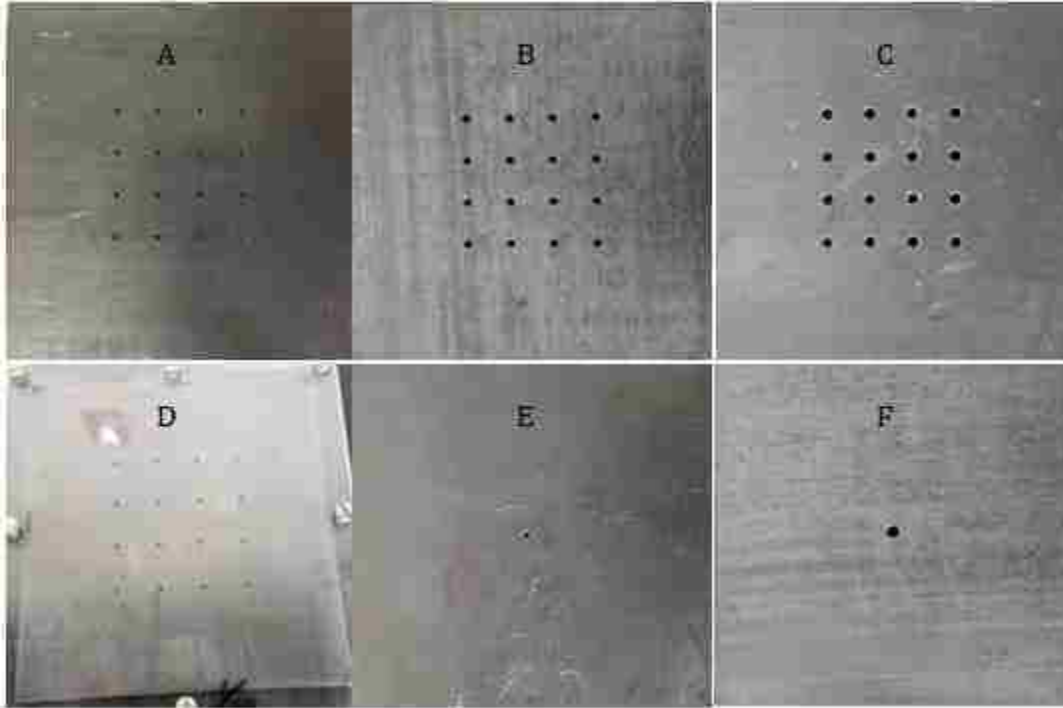
Figure 86: Examples of different pinhole collimators.

Mask	Number of pinholes	Pinhole Separation [cm]	Pinhole Diameter [cm]	Mask Thickness [in]
A	16	1.1	0.1	1/8
B	16	1.0	0.2	1/8
C	16	0.7	0.3	1/16
D	16	1.0	0.1	1/64
E	1	N/A	0.1	1/16
F	1	N/A	0.2	1/8
N/A	1	N/A	0.3	1/16
N/A	16	1.0	0.1	1/32
N/A	16	0.9	0.1	1/8
N/A	16	0.8	0.1	1/16

Table 3: Description of masks found in Figure 86, and more designs not pictured.

As this project is to image distributed sources, we acquired a Co-57 source

distributed over the area of a circle and a lead source mask, shown in Figure 87. It is best

to have a source which is distinguishable by its orientation, the simplest such shape is a

triangle. This has the benefit of allowing us to examine resolution by looking near the

sharper corners of the image. In use, the circular source is taped to the source mask to

mimic a triangular source. Affixing it also prevents motion of the source relative to the triangle mask to prevent variations due to different intensities in different regions for a real source. The source mask is 1/8 in thick and the triangle measures 1.58 cm on a side with slightly rounded inner corners, due to machining constraints.

Figure 87: Triangle source shaper.

The source, along with the source mask, and the pinhole mask, are placed on different shelf levels of an acrylic shelf system built in house. Shelf levels are in 1 cm steps, allowing for great variation in imaging conditions. The shelf system is placed directly on top of the D-Matrix detector, and placement is repeatable by pencil markings made on the detector's metal housing. The experimental setup shown in Figure 88 is what was used to produce the final images.

Figure 88: Experimental setup for imaging the triangle shaped source.

5.2 Single Pinhole Imaging Results

Single pinhole images create one, very detailed image of the source. This is presented first to show source detail as well as possible issues which result from pinhole imaging. The single pinhole masks where of two different pinhole diameters, one of 0.1 cm and the other 0.3 cm. The 0.1 cm diameter pinhole allows very sharp resolution imaging of the source but with low efficiency. The 0.3 cm diameter pinhole allows a higher total efficiency but lower imaging resolution. Both the masks are lead with a thickness of 1/8 in.

First the 0.3 cm pinhole diameter was used. An image which filled the detector was the chosen so that the most detail could be seen. Given the source shaper dimensions, a magnification of 2.6 (SM = 5 cm, MD = 13 cm) was chosen so that the image would fit

the detector but there would not be any loss of the image off the edges of the detector, assuming the source is properly aligned.

The image is very triangular in shape but there are three abnormal sections which look definitely non-triangular. The top right bulge appears to be an impossible source location seeing as the triangle edge continues flatly both above and below it. The source shaper was still intact as well and appeared to not have any defects that could result in less attenuation in this area. The bottom right bulge appears to be very similar to one directly above it. It is possible that the triangle shaper was angled at the time of the image, so the bottom pixels are not flat, however this seems to not be a uniform deviation across the lower pixels. Finally, in the bottom left of the triangle a corner appears to be cut off, resulting in a curved edge where there should be a point. These abnormalities appeared on many 0.3 cm pinhole images, so the 0.1 pinhole was used to see if the improved resolution could be helpful in solving the abnormality problem. Figures 89 and 90 shows the same experimental setups. Figure 89 was created with a 0.3 cm and Figure 90, with a 0.1 cm pinhole.
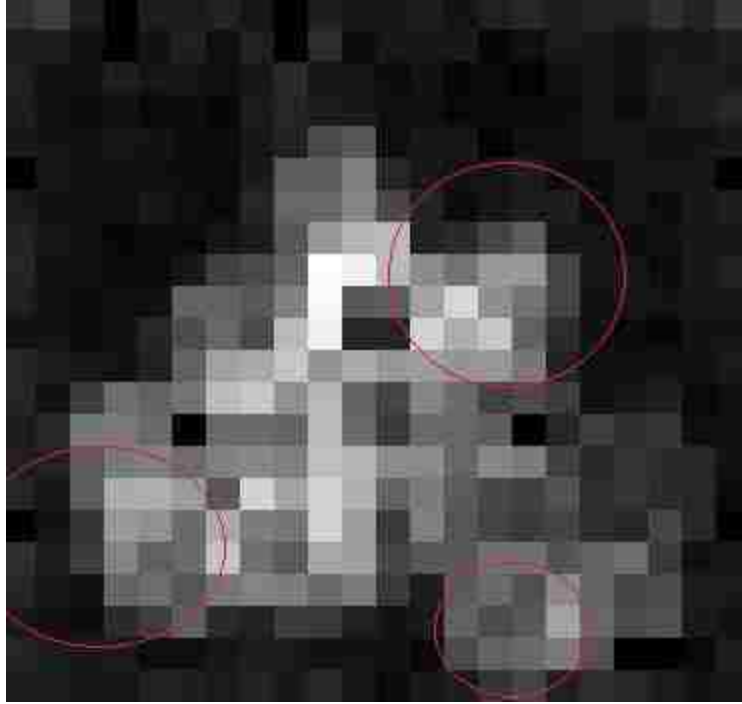
Figure 89: 0.3 cm single pinhole image of triangle shaped Co-57 source with a magnification of 2.6. Abnormalities in the triangular shape are noted.
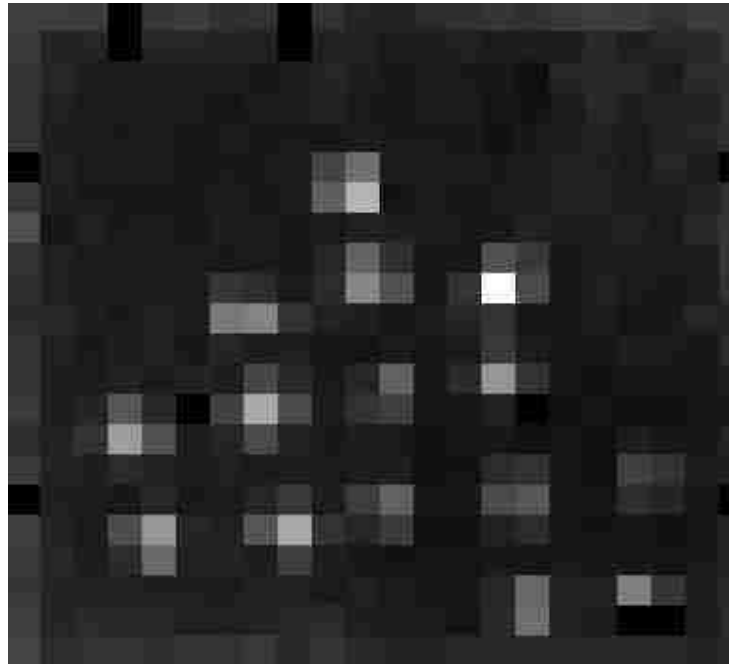
Figure 90: 0.1 cm single pinhole image of the triangle shaped Co-57 source with a magnification of 2.6.

It is immediately apparent that all was not as it seemed when it came to the distributed Co-57 source. Instead of a uniform distribution of Co-57 on the source there

105

were localized points of source material across the face of the source, which we assume were caused by stippling of the source material onto the disk during manufacture. The defects noted in Figure 89 were simply a result of the source stippling and not of defects in the shaper or detector. When contacted, the manufacturer couldn't give information about the size of the stipples on the source. If a uniform distribution of stipples is assumed, then referenced against the size of the triangle source shaper it can be calculated that image resolution is approximately 0.15 cm. This is smaller than the pixel width of the detector, at 0.2 cm so the experimental setup can image to the limits of our detector pixilation. For the rest of the images and reconstructions shown it is important to note that the Co-57 source is not a uniform source and might play a role in the shape of the reconstructed image when using multiple pinholes.

5.3 Multiple-Pinhole Imaging Results

Due to the large number of variables which can be changed in multiple-pinhole imaging and the limited scope of this study, only a few masks were produced and analyzed. The variables involved are the number of pinholes, center-to-center separation of the pinholes - the pitch, diameter of the pinholes and the thickness of the mask. The number of pinholes was chosen to be 16, this was because an additional unit of pinholes would lead to impractically small images for the limited pixel density of the D-Matrix detector. If fewer pinholes were required then the 4x4 array simply needed to be masked so that 2x2 arrays could be created. 1x1 arrays, just single pinhole masks, were also used. Masks with 3x3 arrays were not studied in these experiments. The pitch of the pinholes varies from 1.1 cm to 0.8 cm. The 1.1 cm pitch proved to be too large, no matter

106

what magnification was used there was image loss at the edges of the detector, while 0.8 cm separation proved to be the most practical for most lab applications. Pinholes were produced in 0.1 cm, 0.2 and 0.3 cm diameters. Smaller pinholes proved impractical from an efficiency standpoint when signal was competing with detector electronic noise as well as background radiation. Larger pinholes would result in image overlap in many practical experimental setups as well as increasingly poor imaging resolution. The thickness of the material was determined earlier in the experimentation and heavily depended on the energy of the gamma ray being studied. However, some collimators of thinner material were produced to hopefully achieve results closer to infinitely thin detector simulations.

5.3.1 2 x 2 Pinhole Imaging

Using the already created 4 x 4 pixel mask, two of the rows and columns were masked to create a 2 x 2 pinhole array. Due to only four images being represented on the detector a magnification greater than one was used. Magnification of 1.33 was obtained by a source-to-mask distance of 4 cm and a mask-to-detector distance of 3 cm. This was calculated to be the best magnification for pixel utilization on the detector. A pinhole diameter of 0.2 cm was chosen, 0.1 cm diameter might allow individual stipples to show on each of these resulting sub-images. For reconstruction process it is desired that the source look as uniform as possible in each of the sub-images. Figure 91 shows the resulting image.
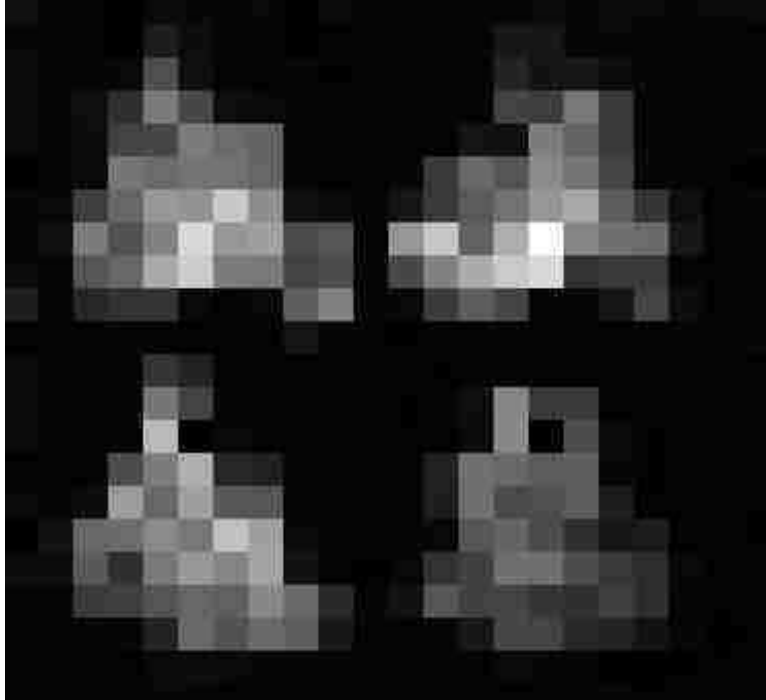
Figure 91: Image created by 2x2 pinhole mask array with a magnification of 1.33.

Each of the resulting sub-images are easily distinguishable as triangles. There are some recognizable differences in the images. These differences could be the result of the detector itself, dead pixels creating gaps or jagged edges. Some of the source stippling might be shown as well. It can also be seen that each image consists of slightly different information about the object. In addition, the upper right image has more intensity in the bottom left corner of the triangle while the bottom left image has greater intensity on the upper right region of the triangle. This means that when reconstructed these images will give all combine to form a complete image of the object, this is shown using the overlap method in Figure 92. The image was calculated to overlap approximately once every 10 pixels. The overlap sum image is in the center of the image and highlighted with a white square around it.
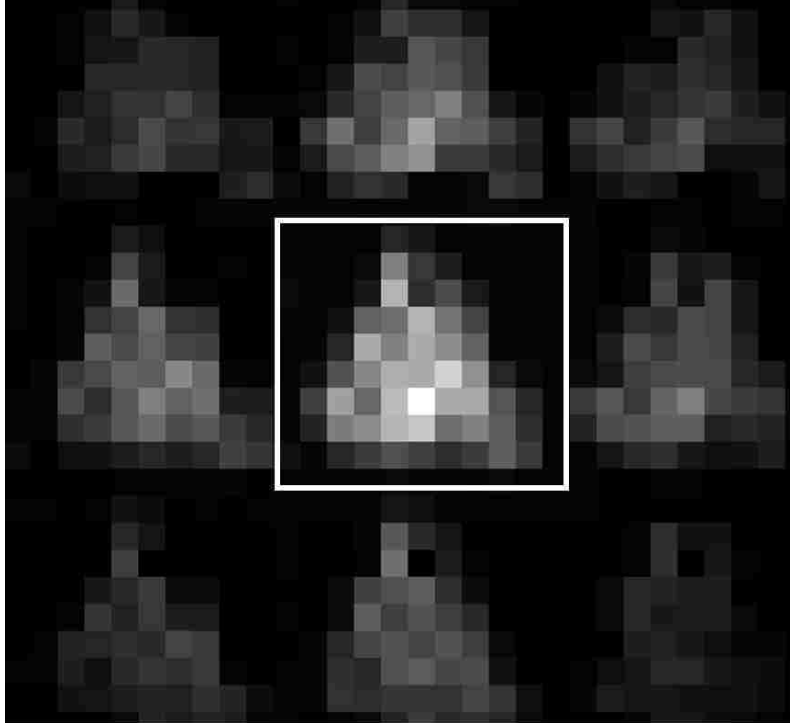
Figure 92: Overlap reconstruction of 2x2 pinhole image.

The reconstructed image appears more complete and triangular than any individual sub-image so it was a success. The total geometric efficiency using four pinholes for imaging was also higher than for a single pinhole. Only using 2 x 2 does not give fine enough position data for the other implications of overlap imaging to be used but it can be used to obtain high-resolution images of a source.

5.3.2 4 x 4 Pinhole Imaging

Many iterations of the 4 x 4 pinhole mask were created and tested but only the most successful and remarkable results will be shared here, Table 5, in Section 5.1, shows all pinhole masks, most of which had the 4 x 4 pinhole arrangement. In the initially characterization of the detector a 4 x 4 mask was used to test the signal-to-noise ratio. As

could be seen from the results the image spacing was too large and cut off potentially useful parts of the sub-images.

First, a mask thickness had to be chosen. Calculations show that any lead mask thickness below 1/8 in would allow some fraction of the gamma rays of interest to penetrate through and add to noise in otherwise dark pixels. The gamma rays may interact by complete absorption in the mask or they may scatter, typically losing energy in the process. With the development of the energy discrimination codes it was hoped that the gamma rays that scatter may fall outside of the gated energy region of interest and not affect counts too much in the region of interest. Figures 93 and 94 show the resulting images from 1/32 in and 1/64 in thickness masks, respectively. Each mask consisted of a 4 x 4 pinhole array, with a separation of 1 cm and pinhole diameters for 0.1 cm. The mask was 2 cm from the detector while the source was 5 cm from the mask.
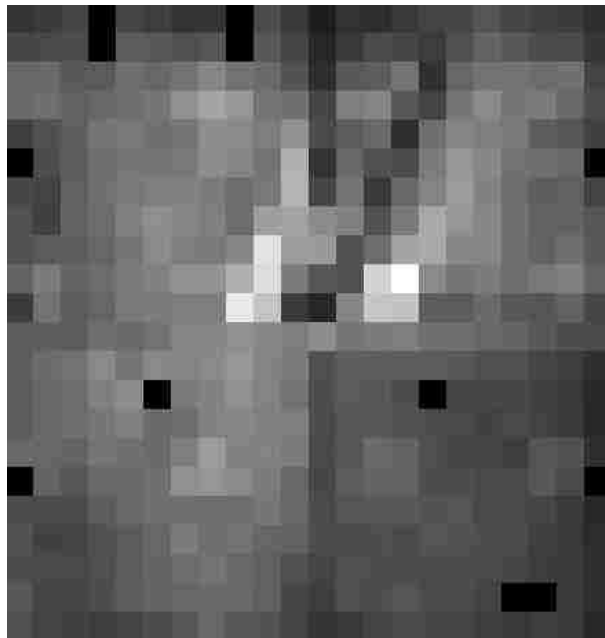
Figure 93: 1/64 in pinhole mask.

Clearly 1/64 in is too thin material to image gamma rays at 122 keV. The sub-images are barely distinguishable even with the best background subtraction algorithm.

The 1/64 in mask would have fair results when imaging x-rays at about 40 keV or below but it is clearly inappropriate for 122 keV gamma rays. The 1/32 in mask showed clearer differences between masked areas and areas behind pinholes for the 122 keV photons, see Figure 93. A cross sectional analysis result is shown in Figure 95 before reconstruction was done.
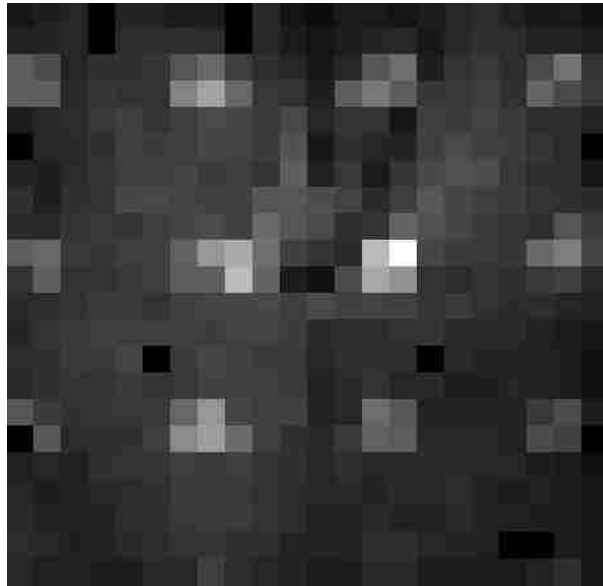
Figure 94: 1/32 in pinhole mask.
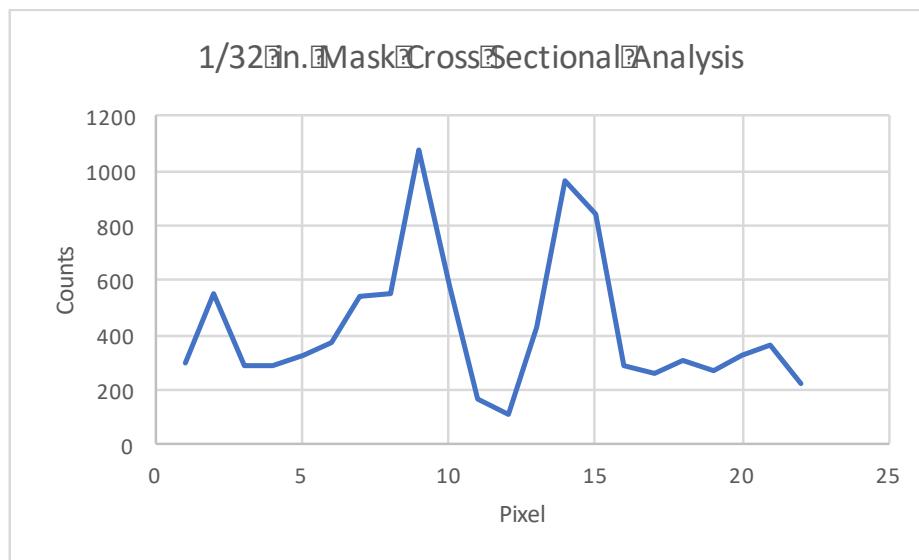
Figure 95: Y-axis cross section at pixel number 11 of the 1/32 in mask.

The average signal-to-noise ratio of the sub-images is about 3, this is more than twice as noisy as the original background subtraction method. From these results it was decided that 1/8 in was the more practical choice for this energy range, the limitations being that sources too close or with too much lateral offset from the detector might not be seen.

Spatially distributed source imaging was attempted with an Am-241 source using the gamma ray at 59.54 keV. The 59.54 keV line is low enough energy that it would be useful in testing out the thin pinhole masks. However, the source was very weak and barely showed up above background, even after very long runs. Figure 96 is an example single pixel spectrum after 12 hours of acquisition at a distance of 10 cm; the 59.54 keV line is visible in the region of channel 700 but it is easily lost in the increasing background noise at the low energy. More advanced peak finding algorithms might be able to consistently distinguish the peak, but due to pixel gain and efficiency variations our program was not able to make significant noise reduction to visualize the source.
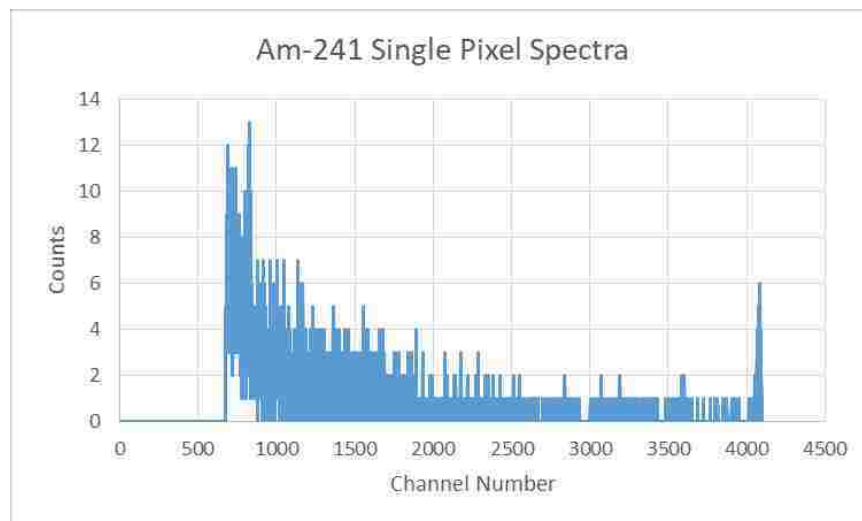
Figure 96: Am-241 single pixel spectrum.

Pinhole masks with a pitch of 1 cm were used to image the Co-57 source. Figure 97a shows the how this spacing allowed all 16 sub-images to fit on to the detector plane, however there is still significant unused space in the detector which could be utilized. The pinhole diameter was 0.1 cm with a source-to-mask distance of 8 cm and a mask-to-detector distance of 2 cm resulting in a magnification of 0.25. The images were collected in 30 minutes of detector operation time.
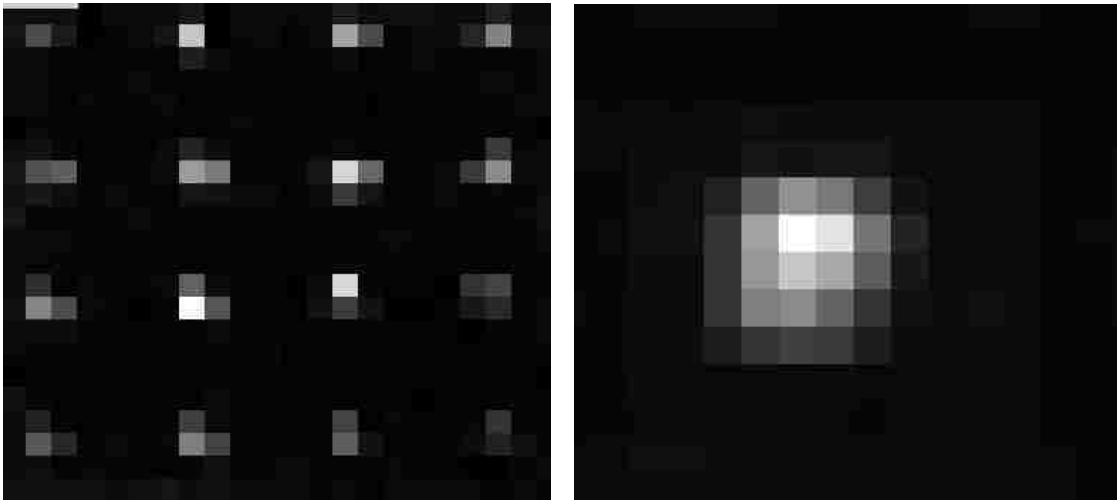
Figure 97: a) 16 sub-image produced with 0.1 cm pinholes at a magnification of 0.25. b) The reconstruction image.

Figure 97b is the reconstruction of the image. This reconstruction is noticeably not triangular. This is because each of the sub-images, which cover only 3 to 5 pixels each, do not contain enough information for the triangle shape to be reconstructed.

The increased resolution of 0.1 cm pinholes does no good when basic source geometry cannot be resolved due to lack of information. Pinhole sizes were then increased to 0.2 cm, keeping all other mask variable constant, this is shown in Figure 98.
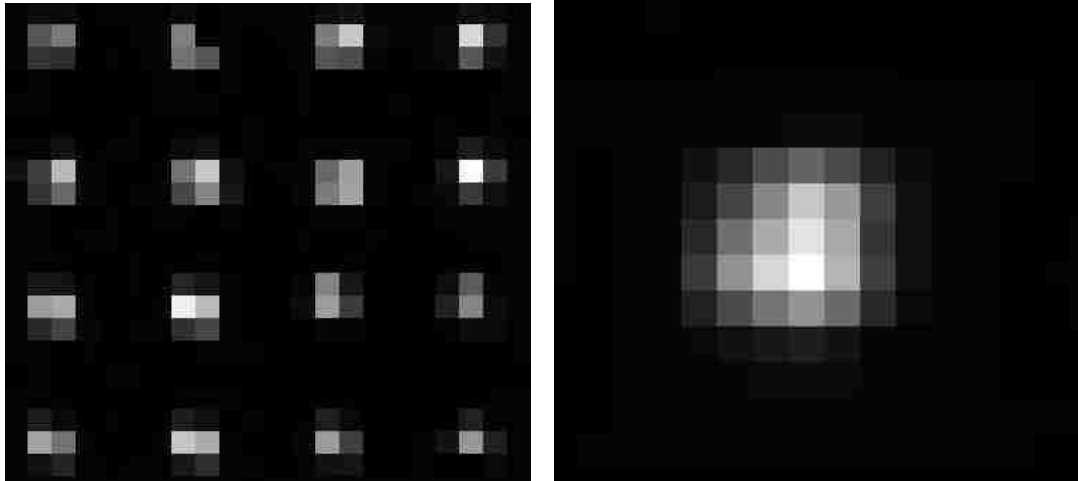
Figure 98: a) 16 sub-images produced with 0.2 cm pinholes at a magnification of 0.25. b) The reconstrcuted image.

Figure 98 shows the resulting detector image and reconstruction. The sub-images in 98a are larger than those in Figure 97a, averaging one more pixel per sub-image, but few are still recognizably triangular. Note that there is still empty space before images overlap so improvements can be made to make better use of the detector area. The reconstruction in Figure 98b shows an image which is still hardly recognizable as triangular. There are hints of triangularity in a narrower top of image than bottom of image and a sloped left side. The images must be larger and be able to convey more information per sub-image for the reconstructed images to work. Increasing the magnification using this particular mask was an option to make the images larger. However, the single pixel buffer between the sub-images and the edge of the detector and a 4 pixel buffer between each of the sub-images (2 pixels for each sub-image) was not something that could be fixed by increasing magnification. A final mask was designed with 16 pinholes separated by 0.8 cm, pinhole diameter of 0.3 cm and a thickness of 1/8 in. Figure 99 shows the resulting image and reconstruction with a source-to-mask

distance of 3 cm and a mask-to-detector distance of 4 cm for 30 minutes of collection time.
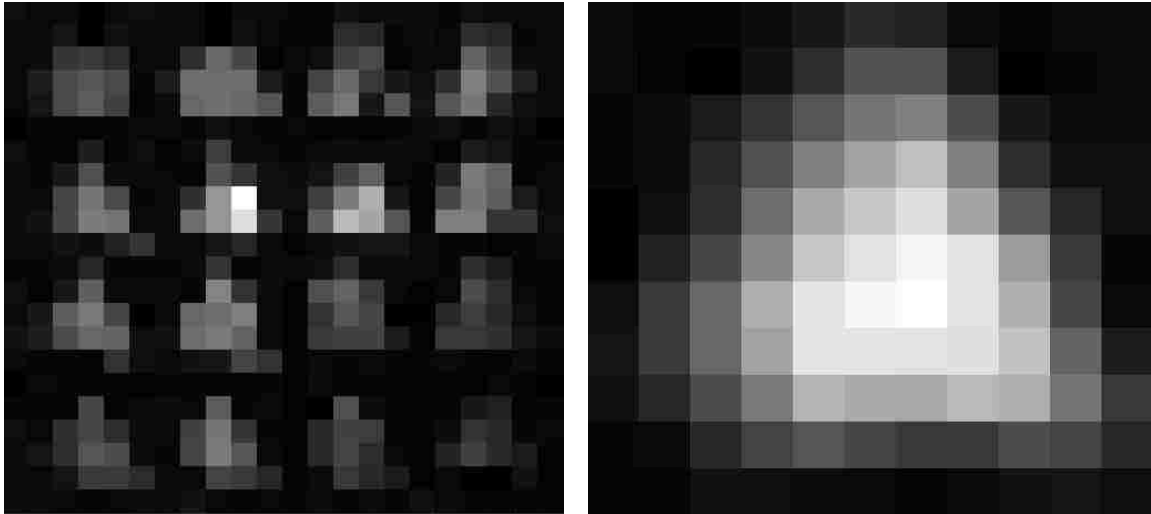
Figure 99: a) 16 sub-images produced with 0.3 cm pinholes at a magnification of 0.75. b) The reconstructed image.

In Figure 99a the sub-images are each of triangular shape and roughly 10 pixels in size. This leaves enough room for there to be blank space between each of the sub-images so that the reconstruction can be clear in shape and without noise. Each sub-image can be seen to have emphasis on specific parts of the triangle depending on their spatial orientation. The bottom left sub-images having emphasis on upper right section of the triangle and upper sub-images having emphasis on lower right section of triangle.

In Section 2.4.3.1 information theory with regard to image reconstruction is discussed. It becomes important here because the center-to-center spacing of the sub-images directly impacts the reconstruction image quality. Having an integer number of pixels between sub-images limits the difference in independent information and leads to very blocky reconstructions in which detail can be lost. Figures 100, 101, and 102 use a mask-to-detector distance of 3 cm, pinhole size 0.3 cm, and pinhole pitch of 0.8, but a varying source-to-mask distances of 3 cm, 5 cm, and 7 cm, respectively. Already shown,

Figure 99 is a part of this data set with a source-to-mask distance of 3. Figure 100 shows

how, with a pixel spacing of 5.7 between the centers of adjacent sub-images, the image

reconstruction can be represented with much smaller steps then in Figure 99. These

smaller pixels lead to a much finer detail reconstruction. With this relatively large

magnification there is some overlap in sub-images, most specifically in the bottom right

of each sub-image which leads to noise in that location in the reconstruction. This overlap

is caused by the abnormality in the source itself due to stippling, which was previously

shown on the bottom right in the high resolution, single 0.1 cm pinhole image in Figure

90. At broader resolution it can still be seen on the bottom right of Figure 100b.
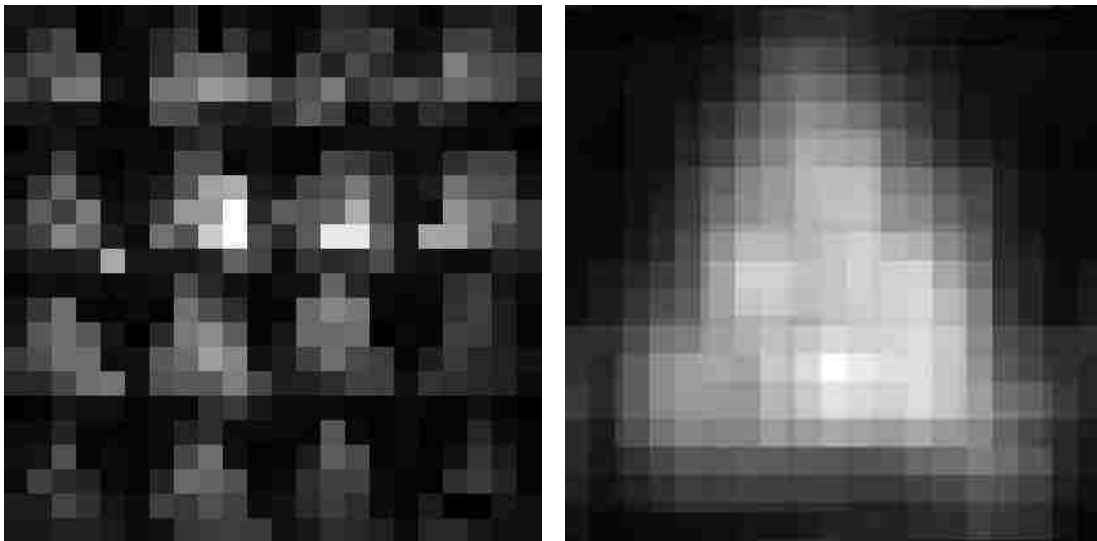
Figure 100: a) 16 sub-images produced with 0.3 cm pinholes at a magnification of 1 and a sub-image spacing of 5.7 pixels. b) The reconstructed image.

At a source-to-mask distance of 5 cm Figure 101 shows a reconstruction done

with an integer sub-image pixel spacing, 5. The resulting reconstruction in figure 101b

has the resulting reconstruction is extremely blocky and not considered good resolution.

116
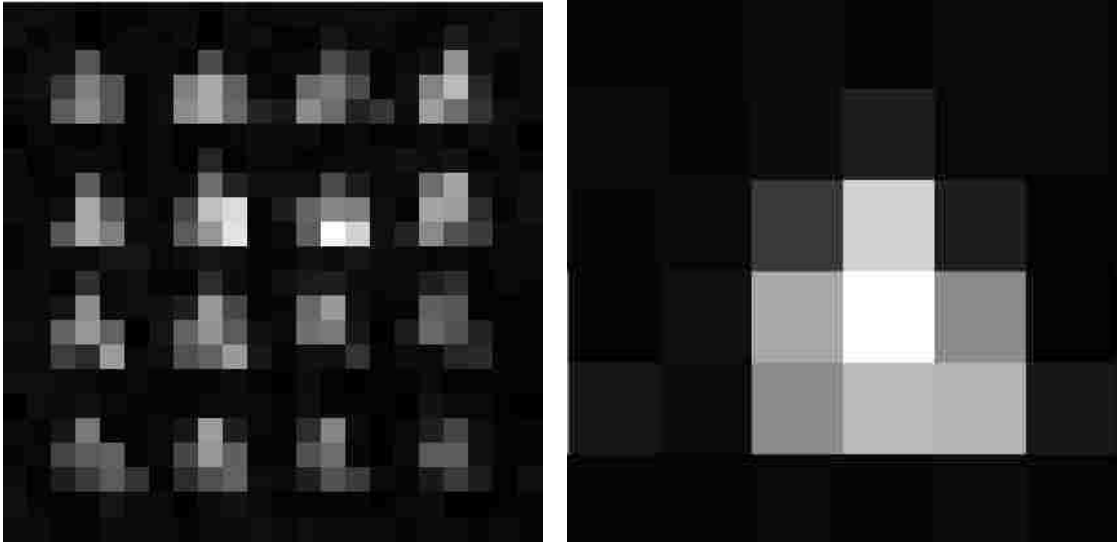
Figure 101: a) 16 sub-images produced with 0.3 cm pinholes at a magnification of 0.6 and a sub-image spacing of 5 pixels. b) The reconstructed image.

In Figure 102 the sub-images are well defined and the image spacing is non-integer at 4.7. However, with a source-to-mask distance of 7 cm, giving a magnification of 0.43 the sub-images become much smaller. Like in Figures 97 and 98 there are simply not enough pixels illuminated for each sub-image to have enough information for the sum-image. It might be possible to determine this as a triangle, but it is not readily apparent.
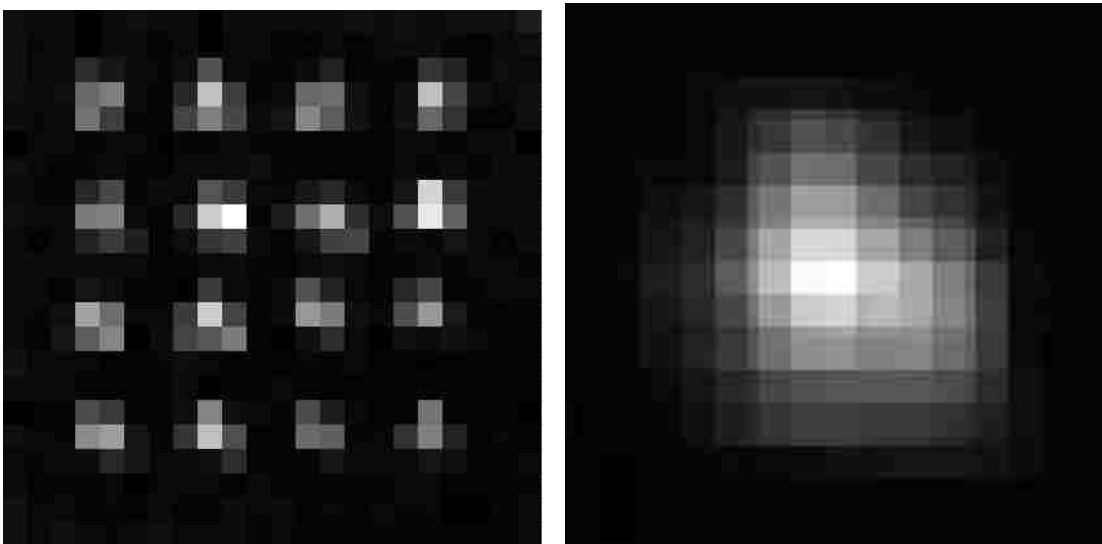
Figure 102: a) 16 sub-images produced with 0.3 cm pinholes at a magnification of 0.43 and a sub-image spacing of 4.7 pixels. b) The reconstructed image.

The next set of measurements used a wider variety of magnifications and distances to observe the effect of information loss through varying sub-image spacing. The same pinhole mask was used but this time the mask-to-detector distance was increased to 6 cm which allows for a wider range of magnifications.

The first run done was with a source-to-mask distance of 4 cm and a mask-to-detector distance of 6 giving a magnification of 1.5. This is an extreme case, but the results were interesting. This magnification was enough in this situation for the individual stipples of the sources to be seen in every sub-image. This made the sub-images in Figure 103a a series of points rather than distinguishable shapes. This made the sub-image spacing nearly impossible to determine. The reconstruction shown in Figure 103b is very poor, a pixel spacing of 6.5 was used through trial and error. After attempting the reconstruction with multiple different pixel spacing it was decided that 6.5 yielded the best results, though still very poor.
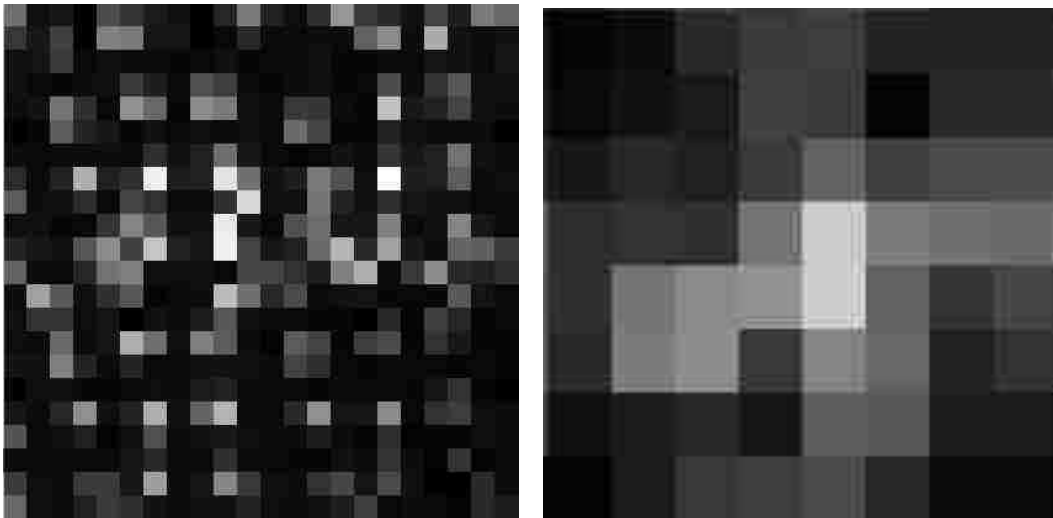
Figure 103: a) 16 sub-images produced with 0.3 cm pinholes at a magnification of 1.5 and a sub-image spacing of 6.5 pixels. b) The reconstructed image.

Figure 104a still shows the stippling of the source and very inconsistent triangular sub-images. However, 104b does a remarkable job at the recreation of the source. It is

apparent that the spatial frequency chosen for reconstruction was more appropriate. This was a 16 pinhole mask with a pitch of 0.8 cm, pinhole diameter of 0.3 cm, a source-to-mask distance of 6 cm and a mask-to-detector distance of 6 cm. Since the stippling shows in the sub-images, it is the translated to the reconstruction as relative hot spots within the triangle. The stippling seen in the reconstruction is similar to that seen in the high-resolution single pinhole image in Figure 90.
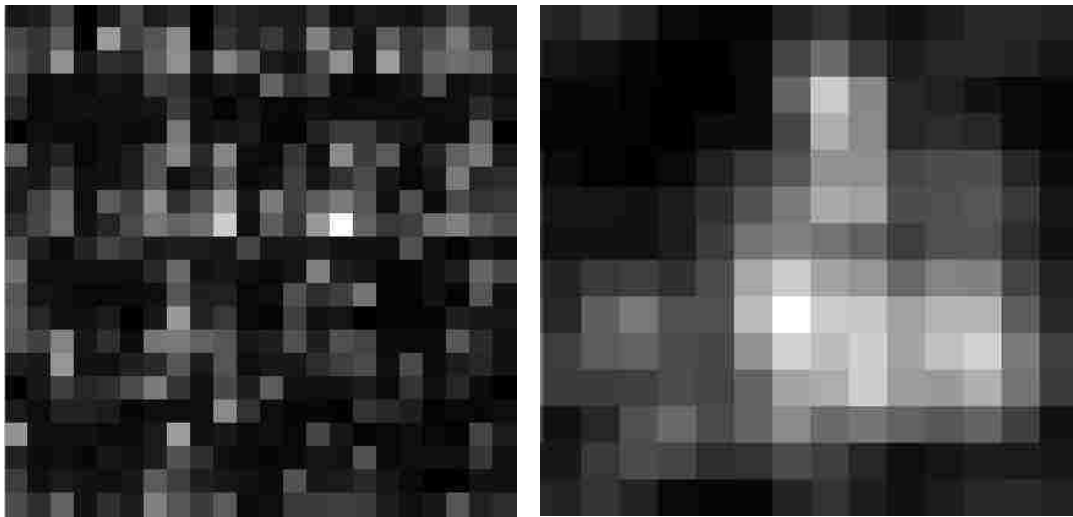
Figure 104: a) 16 sub-images produced with 0.3 cm pinholes at a magnification of 1 and a sub-image spacing of 6.5 pixels. b) The reconstructed image.

With Figure 105, using a 16 pinhole mask with a pitch of 0.8 cm, pinhole diameter of 0.3 cm, a source-to-mask distance of 8 cm and a mask-to-detector distance of 6 cm, triangular sub-images can be clearly seen but there does appear to be some overlap. This magnification is another case where the sub-images in Figure 105a have an integer pixel spacing and results in a blocky reconstruction. The reconstruction, however poor resolution, is still easily recognizable as a triangle in Figure 105b.
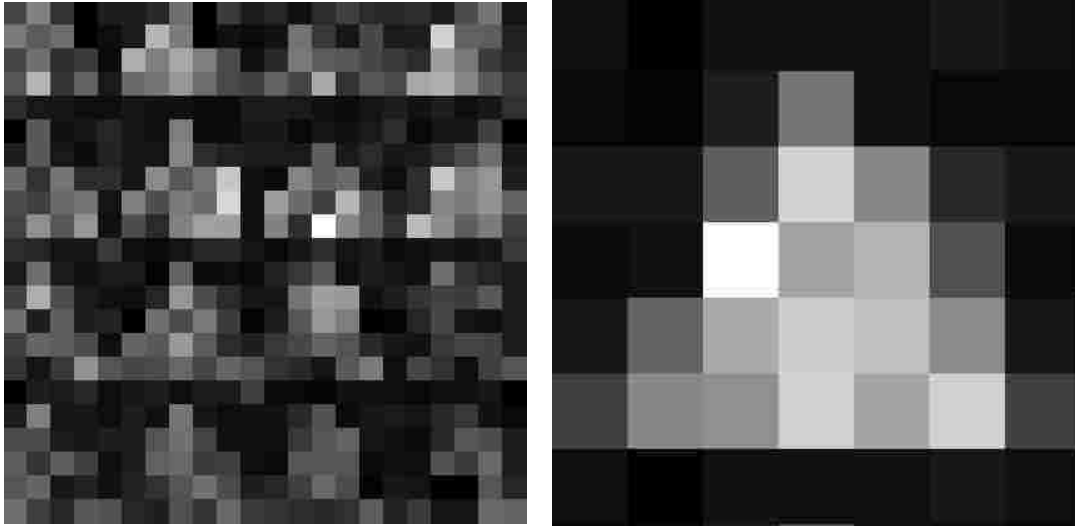
Figure 105: a) 16 sub-images produced with 0.3 cm pinholes at a magnification of 0.75 and a sub-image spacing of 6 pixels. b) The reconstructed image.

The next two images and reconstructions show non-integer spaced reconstructions which result in finer step images of the source. Figures 106 and 107 are done with the 16 pinhole mask, a pitch of 0.8 cm and Figure 106 has a source-to-mask distance of 10 cm and a mask-to-detector distance of 6 cm while Figure 107 has a source-to-mask distance of 12 cm and a mask-to-detector distance of 6 cm. There is significant noise in these images, the reconstruction broadens in both Figures and becomes blurred. Possible reasons for this noise could be lack of image clarity due to size of sub-images or long run times which allow detector noise to build up.
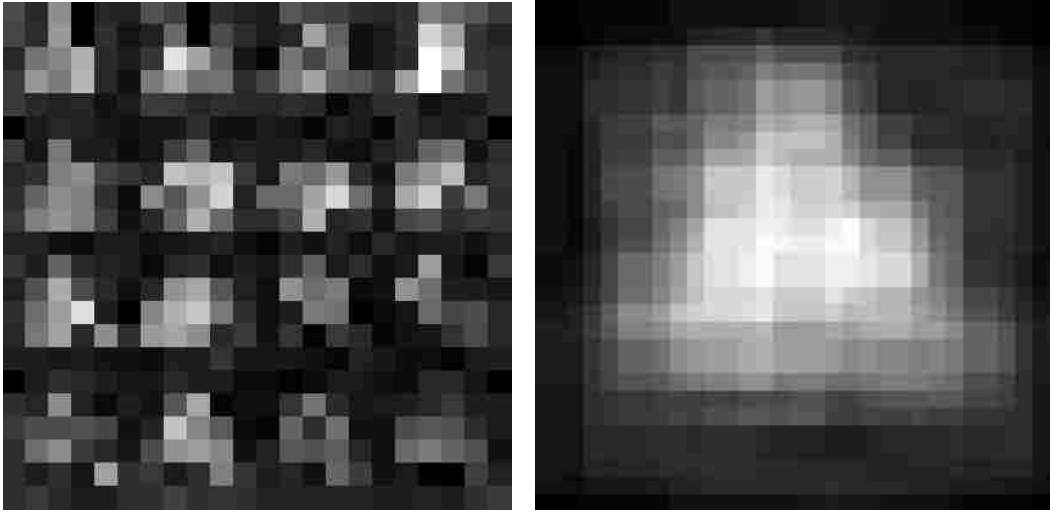
Figure 106: a) 16 sub-images produced with 0.3 cm pinholes at a magnification of 0.6 and a sub-image spacing of 5.6 pixels. b) The reconstructed image.
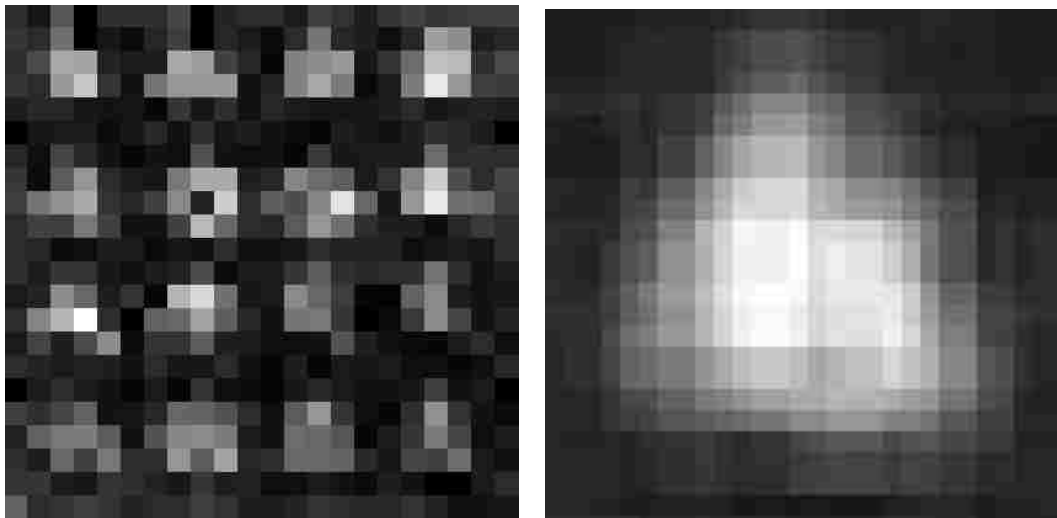
Figure 107: a) 16 sub images produced with 0.3 cm pinholes at a magnification of 0.5 and a sub image spacing of 5.4 pixels. b) The reconstructed image.

Finally, with Figure 108 the sub-images, which are decreasing in size happen upon an integer spacing and result in a very poor image of the source. This was run with the 16 pinhole mask, a pitch of 0.8 cm and a source-to-mask distance of 10 cm and a mask-to-detector distance of 6 cm.
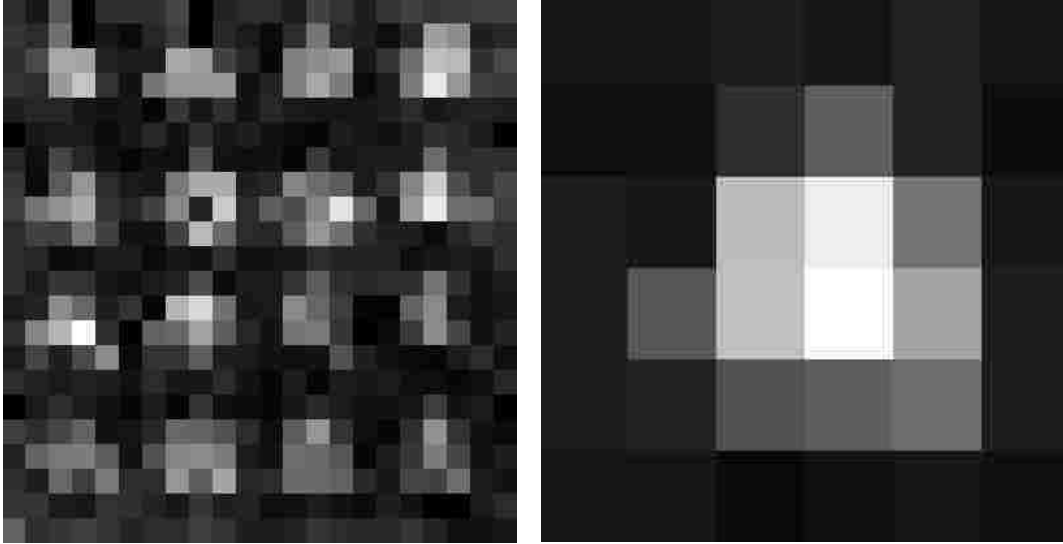
Figure 108: a) 16 sub images produced with 0.3 cm pinholes at a magnification of 0.43 and a sub image spacing of 5 pixels. b) The reconstructed image.

5.3.3 Resolution

The poor resolution, integer pixel number spacing should be avoided. It is possible to relate pinhole spacing, sub-image spacing, and magnification. By like triangles, for a point source the pinhole size "a" is projected as an image size "I" on the detector face with the ratio I/a = the source-to-detector distance/the source-to-mask distance, or $I = a(SM+MD)/(SM)$, following Equation 14. For a distributed source we can talk about the magnification from the source to the image, where $M =$ MD/SM. In terms of magnification M then the image size I can be stated as Equation 17. This can be put in terms of pixel numbers by dividing by 2 mm, the size of a pixel.

$$I = a\left(\frac{SM+MD}{SM}\right) = a\left(\frac{SM}{SM} + \frac{MD}{SM}\right) = a(1 + M) \tag{17}$$

Tests were done to determine how close two sources could be located and still resolved. The pixilation of the detector into 2 mm squares is the limiting factor in how sharp the resolution of the reconstructed image can be achieved. An Eu-152 point source

was placed at 7 different axial locations with a constant source-to-mask distance of 10 cm and mask-to-detector distance of 3 cm. The results of each detection run were then separately saved so that overlap could be seen. A 16 pinhole mask was used with a pinhole diameter of 0.1 cm and a pinhole spacing of 0.8 cm. The seven locations were -0.6 cm to + 0.6 cm by 0.2 cm steps. The images of these point sources were the reconstructed and one dimensional cross sections were taken of each source at a constant value. Then the one dimensional cross section of the source was fitted with a Gaussian which allowed us to measure the FWHM of the response. When two sources can be considered resolved is where there is no overlap in their FWHM. Theoretically the spatial resolution should be enough to determine source separation at 1 cm apart. Figure 109 shows the two sources 0.6 cm apart, it is apparent that their FWHM overlap greatly, as expected. The x-axis in the following figures is representative of reconstruction space.
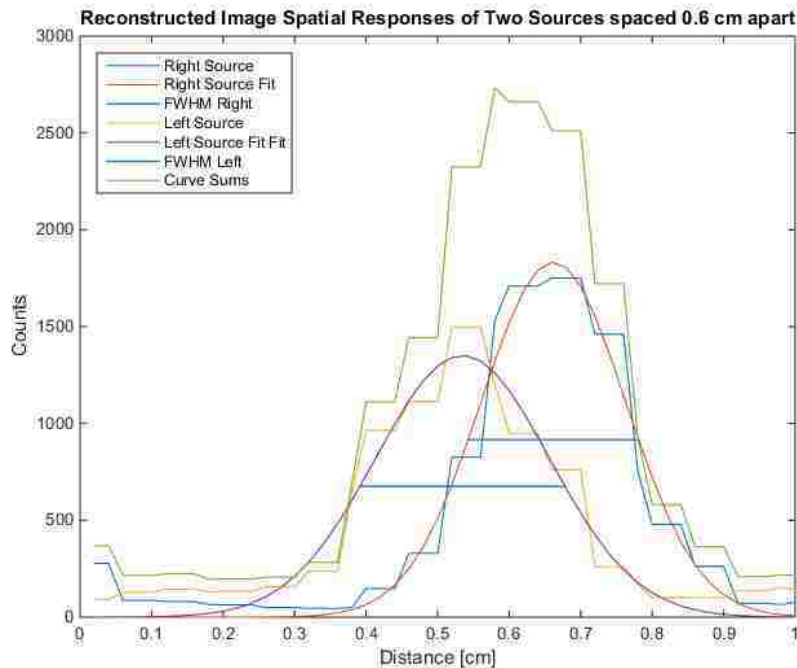
Figure 109: Two sources, 0.6 cm apart that cannot be resolved.

123

At 1 cm separation it is predicted that the sources should be resolvable. However, Figure 110 shows that there is still some overlap in the responses, this is due to multiple factors. First the inherent limitations due to the pixilation which means that a source that two gamma rays that strike the detector 0.2 cm apart from each other have a chance of appearing as if they impacted at the same location. Then there are complications when collecting the charge generated from each of the photon events. The anodes are not completely separated from each other so it is possible that a photo strike that occurs in one pixel can show up on multiple pixels surrounding it. While the result of this non-perfect electron collection should result in a count that get eliminated in energy discrimination, noise can overlap and show up as real counts.
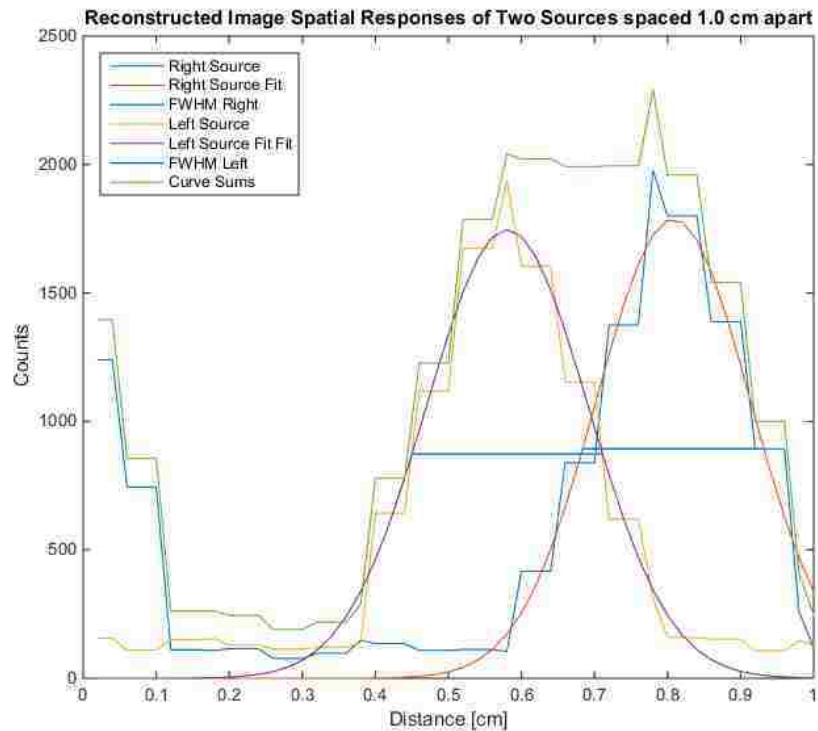
Figure 110: Two sources, 1.0 cm apart that should theoretically be resolvable but because of detector effects there is overlap in their responses.

Finally in Figure 111, with a separation of 1.2 cm, the sources are shown as clearly resolvable from one another using their FWHMs.
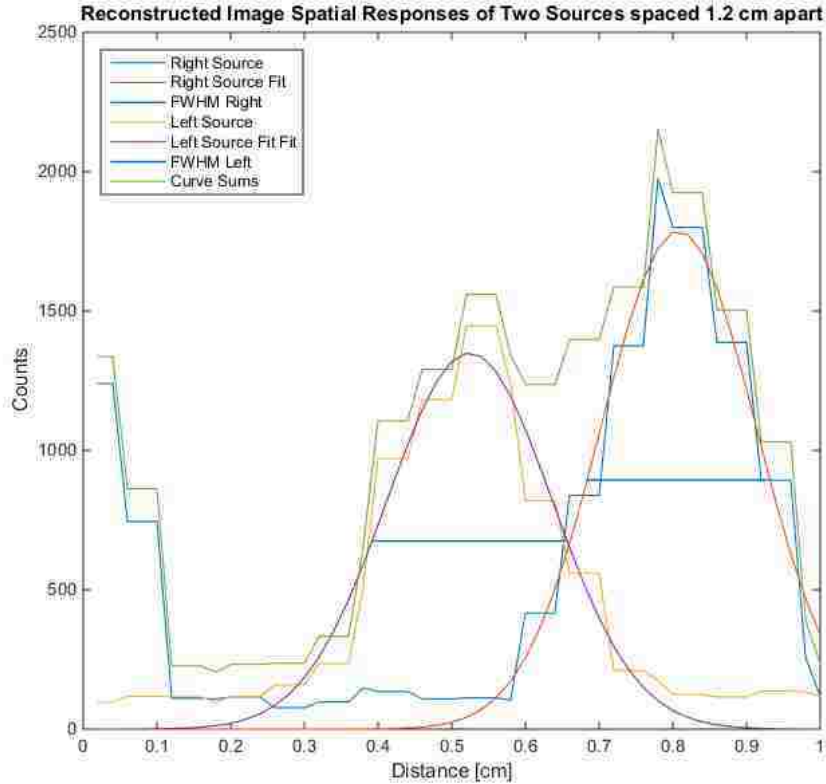
Figure 111: Two sources, 1.2 cm apart which can be resolved.

5.3.4 Depth of Field

The previous section shows that image spacing and the distance of the source from the mask are related. With this information it should be possible to determine source distance from the collimator simply by looking at the sub image spacing. The theory is discussed in detail in Section 2.4.4. From that section, we can relate mask-to-detector distance (MD), magnification ($\mathcal{M}$) and source-to-mask distance (SM), where magnification in this case is of the center-to-center distance between pinholes (ph) to the

center-to-center distance between images (im), $\mathcal{M}$ = im/ph. Restating Equation 9 we

have:

$$SM = \frac{MD}{\mathcal{M}-1} \tag{18}$$

As an example of how we extract the image distances and thus the spatial

frequency of the sub-images on the detector, we examined the Eu-152 point source. This

image was generated with a pinhole spacing of 0.8 cm a source-to-mask distance of 10

cm and a mask-to-detector distance of 3 cm. The image is presented in Figure 112.
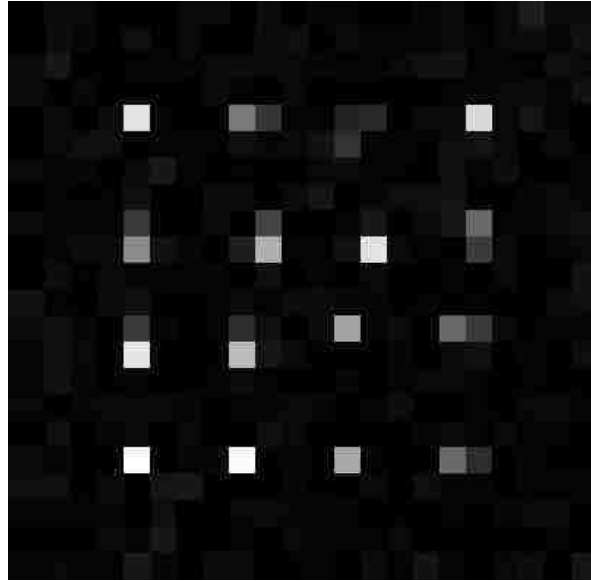
Figure 112: Eu-152 point source imaged on the full detector.

Assuming that x and y- axis projections show the same spacing, Figure 133 shows

projection of the data onto the x-axis. The spacings between the peaks were averaged and

then the error was calculated using the standard deviation of the mean to get a pixel

spacing of 0.80 ± 0.06 cm. This same method to calculate error is applied later in the

section when two sources at different distances are imaged simultaneously and their

source-to-mask distances are determined.
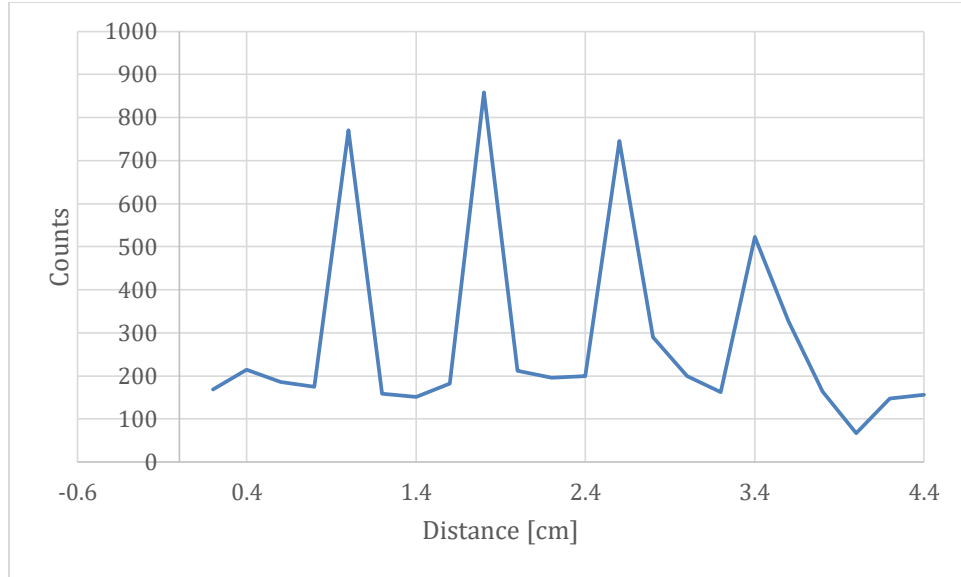
Table 4 shows a summary of the experimental parameters used for a point Eu-152 source. There were three difference mask-to-detector distances each with varying source-to-mask distances resulting in a varying sub-image spacing. This data will allow us to check our geometric expectations of the system.

Pinhole Spacing [cm]	MD [cm]	SM [cm]	$\mathcal{M}$	Sub-image Spacing [cm]
0.8	3	2	2.25	2
0.8	3	3	1.425	1.6
0.8	3	4	1.325	1.4
0.8	3	5	1.25	1.28
0.8	3	7	1.175	1.14
0.8	3	10	1.125	1.04
0.8	3	15	1.125	0.96
0.8	6	5	2.075	1.76
0.8	6	6	1.75	1.6
0.8	6	8	1.5	1.4
0.8	6	10	1.4	1.28
0.8	6	12	1.35	1.2
0.8	6	14	1.25	1.14
0.8	9	5	3.5	2.24
0.8	9	9	2	1.6
0.8	9	12	1.675	1.4
0.8	9	30	1.275	1.04

Figure 112 shows the comparison of data points from Table 4 to the expected geometric relationship we can derive from magnification. An uncertainty of ±0.06 cm on the sub-image spacing, im, is carried over from the example above. The data does not show a linear relationship which is expect from the magnification trend.
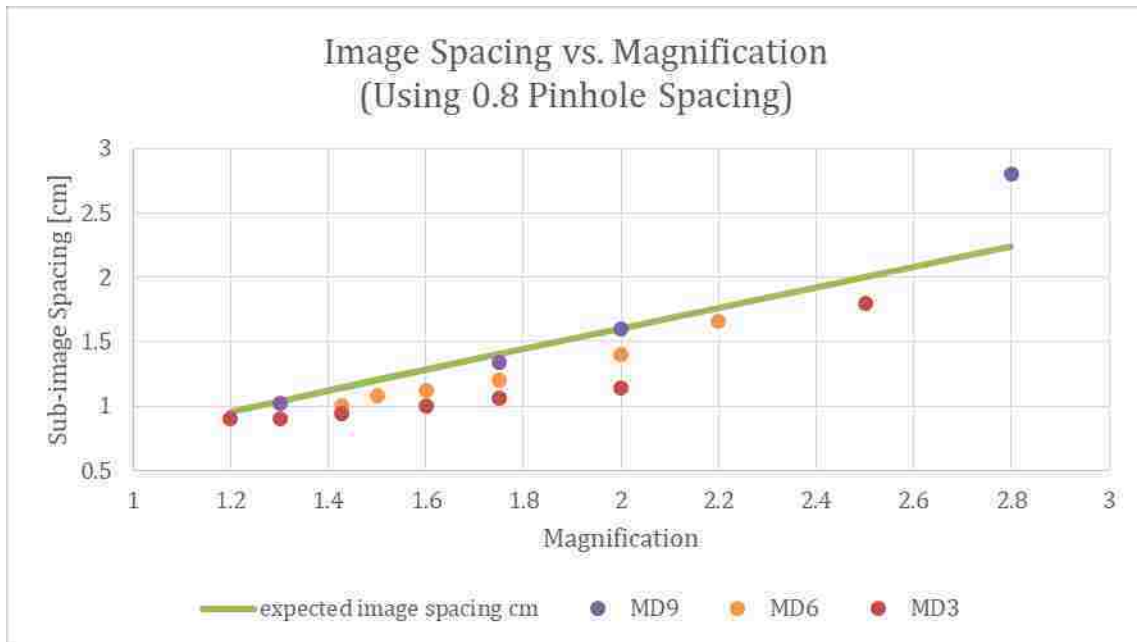
Figure 114: Comparison of experimental data to the expected geometric relationship. Data points for MD = 3 cm, 6 cm and 9 cm are shown in different colors. The expectation line based on the geometric arguments is the solid line.

Figure 115 shows Equation 18 applied to three different mask-to-detector distances (top: 3 cm, middle: 6 cm, bottom: 9 cm) and compared to experimental data. While the general trends of these fits are representative of the experimental data, the accuracy of the theoretical prediction to the experimental data is not accurate. The predicted line matches the data more closely as the mask-to-detector distance is increased.
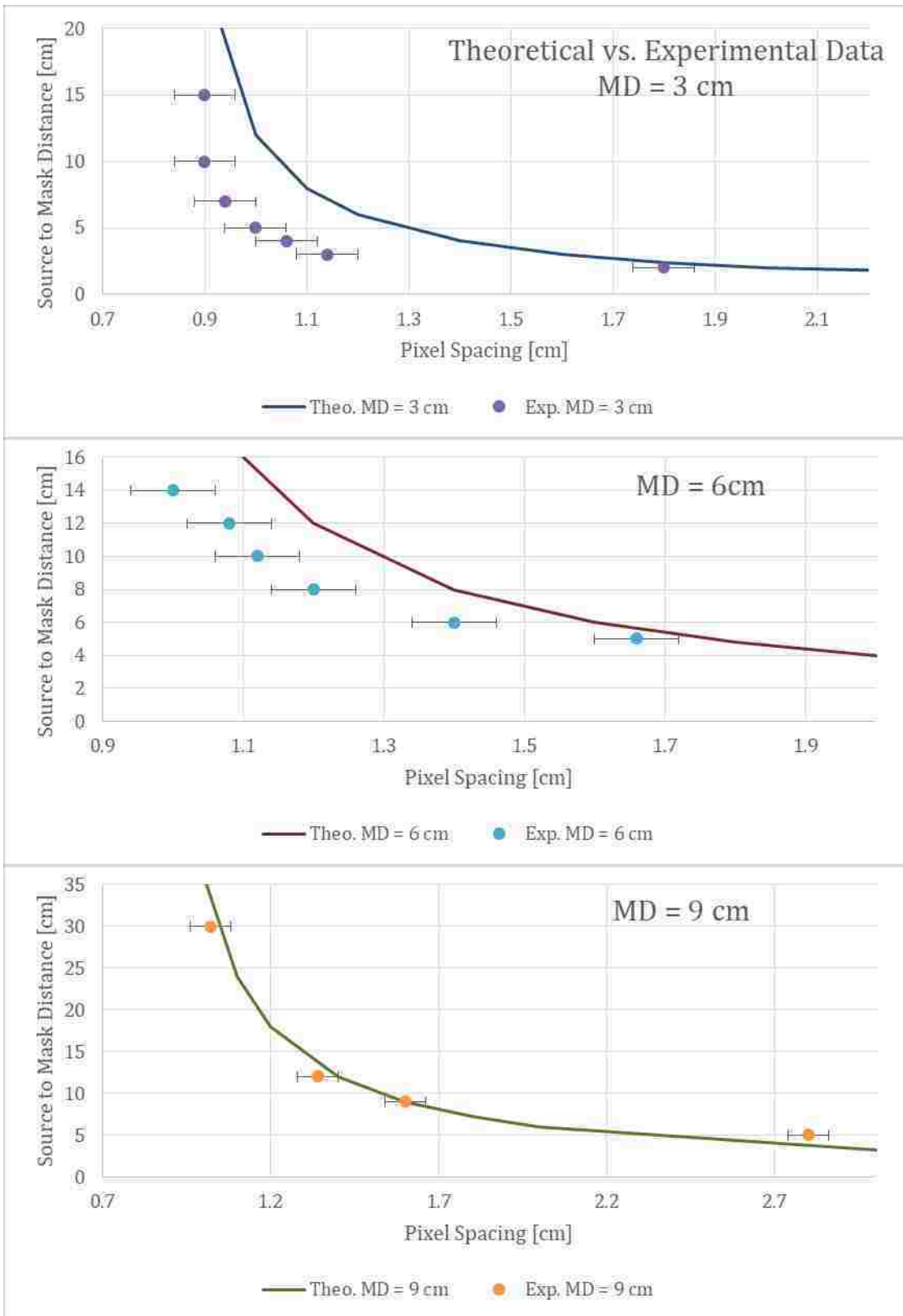
Figure 115: Three graphs that show the experimental data and the geometric expectation for (top) MD = 3 cm, (middle) MD = 6 cm and (bottom) MD = 9 cm.

129

With further analysis it was discovered that if the mask-to-detector distance is decreased by 1.75 cm the fit lines become more accurate to the data. This stems from the design of the detector, the CZT crystal are recessed and the depth of the crystals has not actually been measured due to the sensitivity of the electronics and fear of damage. So the depth of the crystal below the plane of the detector was taken from the engineering schematics of the detector. It is possible that the distances represented on the schematics were not accurate to the current model or a typo occurred. Figure 116 shows the much closer match between data and geometric expectations.

Changing MD also changes the magnification so Figure 114 is reproduced with new values as Figure 117. The match between data and expected is remarkably good but there are some outlier at higher magnifications. The fits accurately represent the experimental data enough to where predictions on source-to-mask distances could be made using this equation. As pixel spacing increase as source-to-mask distance decreases the fit from Equation 18 becomes less accurate. This is most likely due to the thickness of the pinhole mask due to the geometric theory assuming an infinitely thin mask.

Further experimental work was done with point sources. Two point source of two different energies were imaged at the same time and at different distances. Ba-133 and Eu-152 sources were used, each was offset from the centerline normal to the detector by 2 cm so that they images would not direct overlap and so that one source would not shield the other. The raw result is shown in Figure 118.
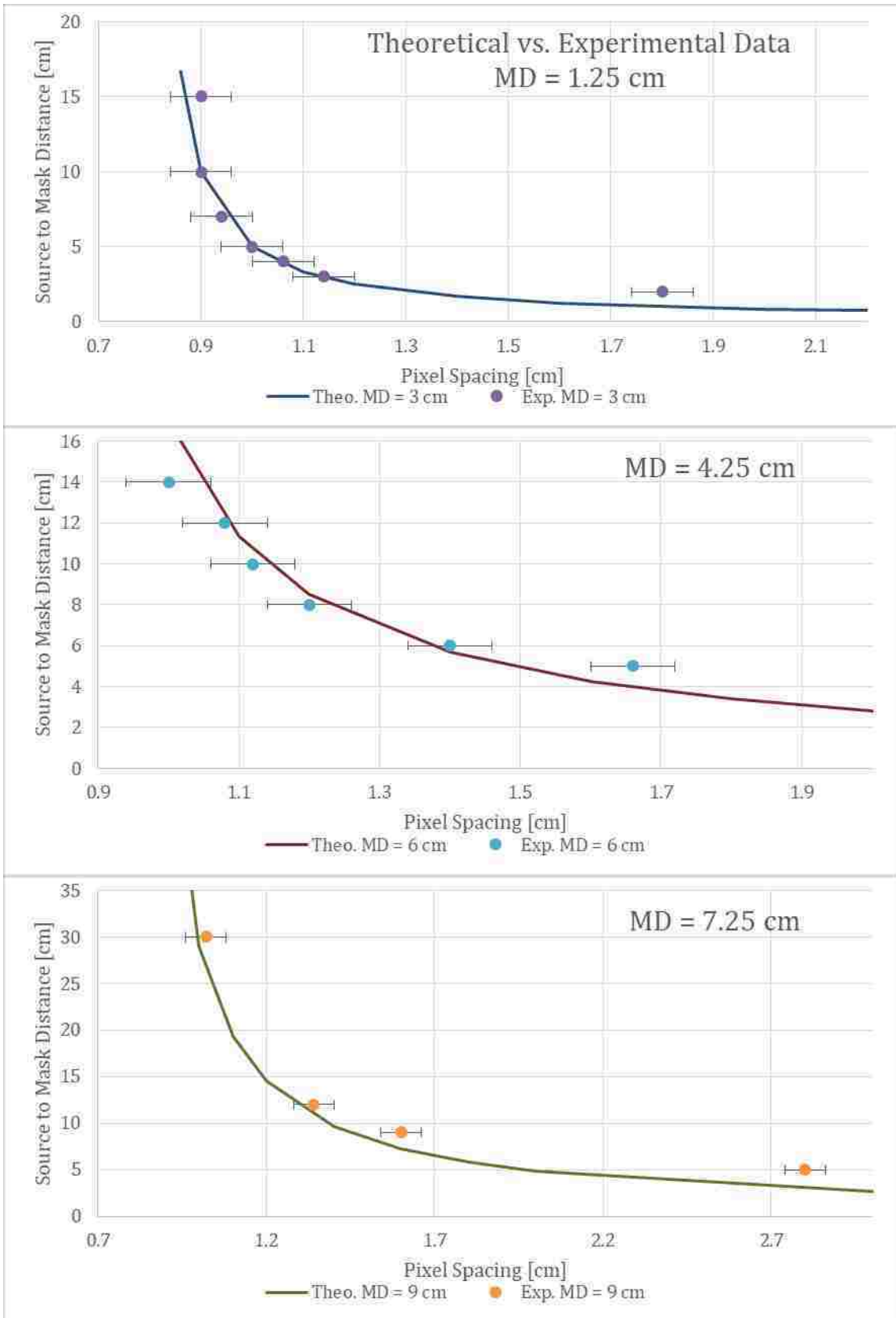
Figure 116: Three graphs that show the experimental data and the geometric expectation for (top) MD = 1.25 cm, (middle) MD = 4.25 cm, (bottom) MD = 7.25 cm. MD values are reduced from figure 115 by 1.75 cm.

131
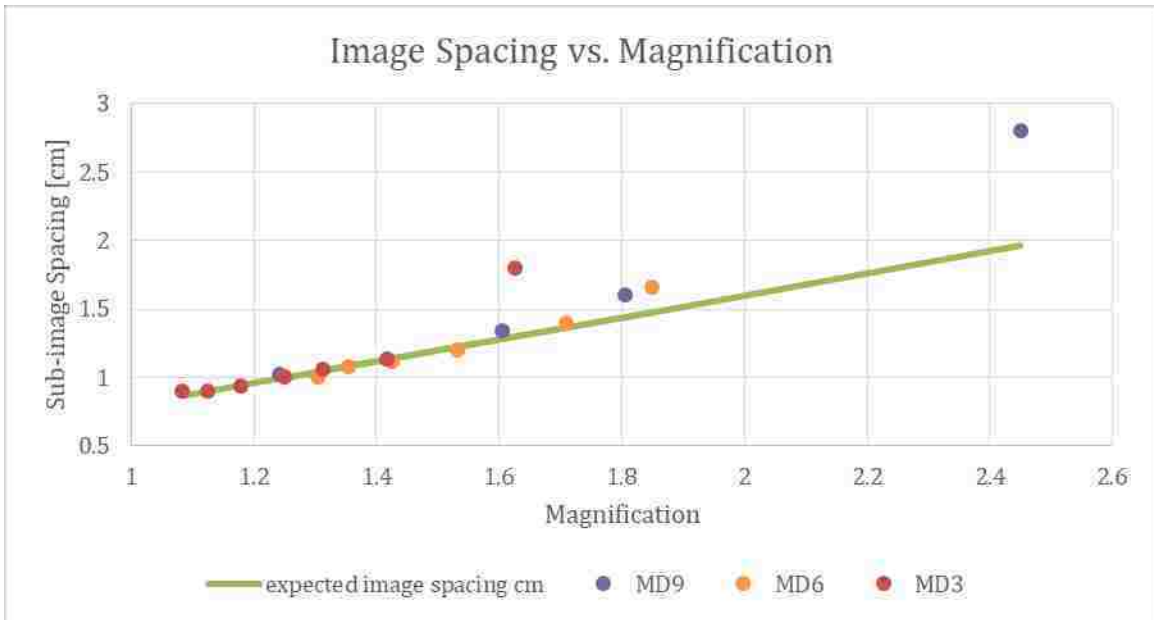
Figure 117: Comparison of experimental data to the expected geometric relationship. Data points for MD = 1.25 cm, 4.25 cm and 7.25 cm are shown in different colors. The expectation line based on the geometric arguments is the solid line.
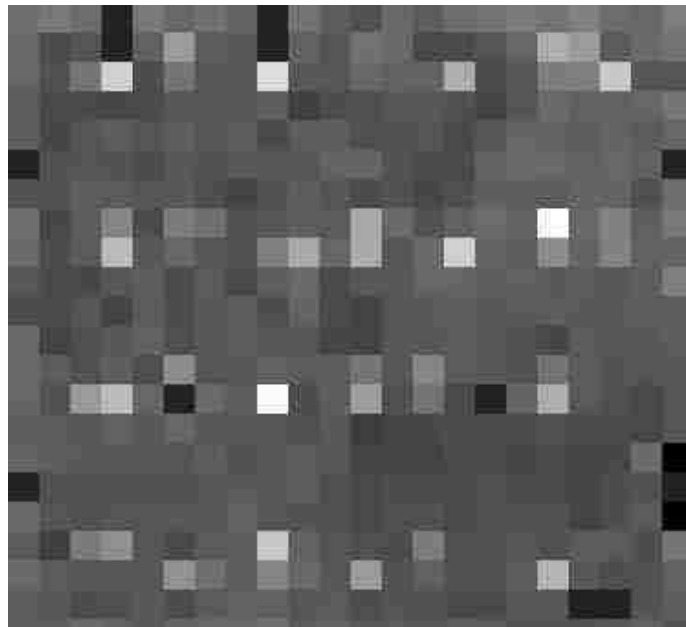
Figure 118: Heat map including both Ba-133 and Eu-152 sub-images.

The average of all the sub-images spaces is taken to get the best answer for the correct image spacing. This raw data was then analyzed using the same analysis method as before but this time modified to look for two separate energy peaks and bin them

132

differently. Figure 119a shows the Ba-133 81 keV signal, which has a spacing of 5.5 pixels, while Figure 119b shows the Eu-152 40 keV signal, which has a spacing of 6 pixels.
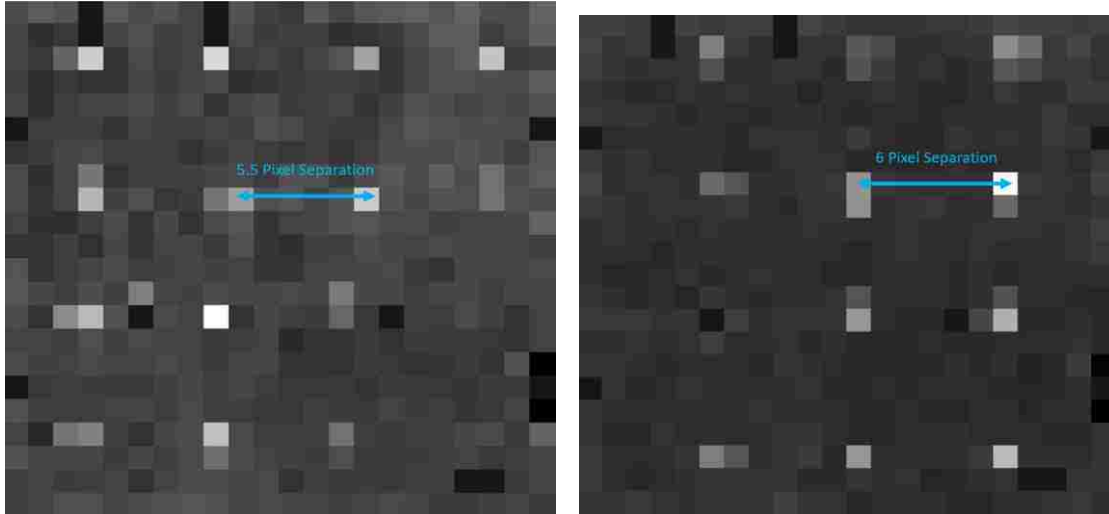
Figure 119: a) Isolated Ba-133 sub images with spacing of 5.5 pixels. b) Isolated Eu-152 sub images with a spacing of 6 pixels.

Just from the simple inspection of pixel spacing, it can be seen that the Eu-152 source is closer to the detector. This is a very easily applied source of information without consulting formulas or further analysis. If Equation 18 is solved for these two pixel spacings, the results are 20 ± 0.4 cm SM distance for the Ba-133 source and 10 ± 0.06 cm SM distance for the Eu-152 source. The real distances of the two sources were 18 cm and 10 cm, respectively. Both calculations are very close but only the closer source was within error, but there is room for improvement. Additional images with this pinhole mask at varying mask-to-detector distance could improve answers and the equations describing the source-to-mask relationship.

Due to the varying distances of the two sources, there is a different spatial frequency on the detector face and a focus can be done by using the appropriate spatial frequency in adding sub-images to make the sum image. A source is focused when the

133

correct spacing is used and its reconstruction has very high resolution. When the incorrect

spacing is used the source is not in focus and the reconstruction is very broad resolution.

Figure 120 shows the reconstruction of Ba-133 using the correct step size of 6 pixels as

well as the wrong step size of 5.5 pixels, which would be appropriate for Eu-152. The

FWHM of the in-focus Ba-133 source is 1.5 cm while the FWHM of the defocused

source is 2.0 cm.
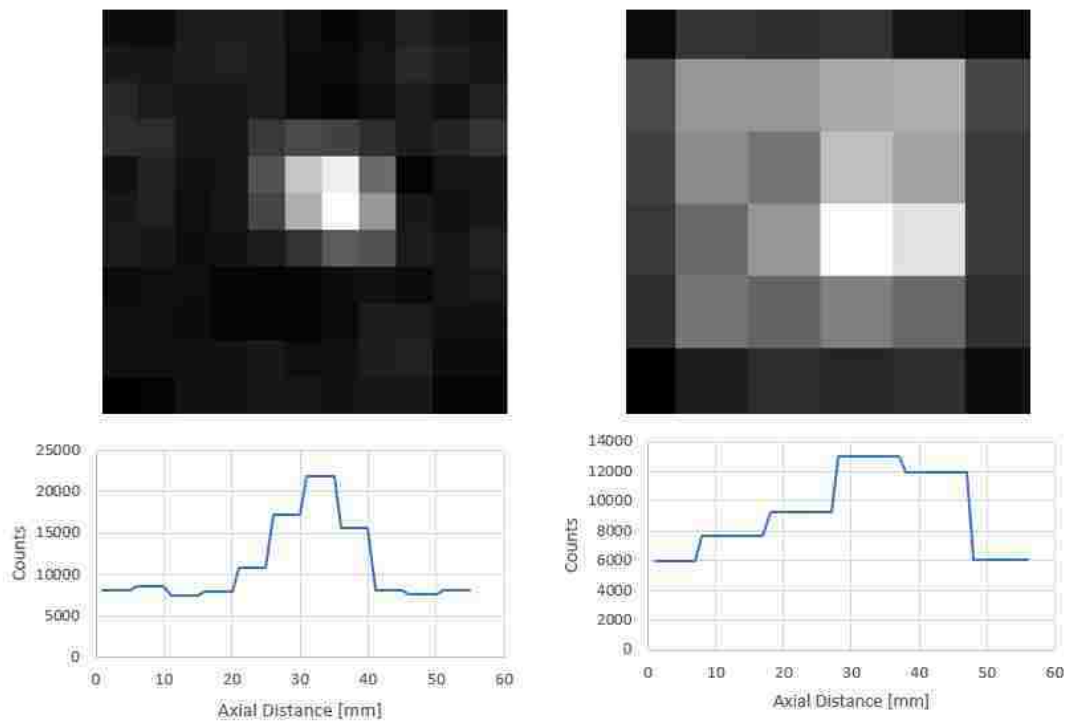
Figure 120: Top left: in focus reconstruction of Ba-133 using a 5.5 pixel spacing. Bottom left: one dimensional projection of reconstructed Ba-133 source with FWHM of 1.5 cm. Top right: defocused reconstruction of Ba-133 using a 6 pixel spacing. Bottom right: one dimensional projection of reconstructed Ba-133 source with a FWHM of approximately 2.5 cm.

The Eu-152 source was reconstructed using a pixel spacing of 5.5 and 6. The

focused Eu-152, shown in Figure 121, with a pixel spacing of 6 yielded a reconstruction

with a FWHM of 1.0 cm while the defocused Eu-152 reconstruction with a 5.5 pixel

addback resulted in a 1.5 cm FWHM.
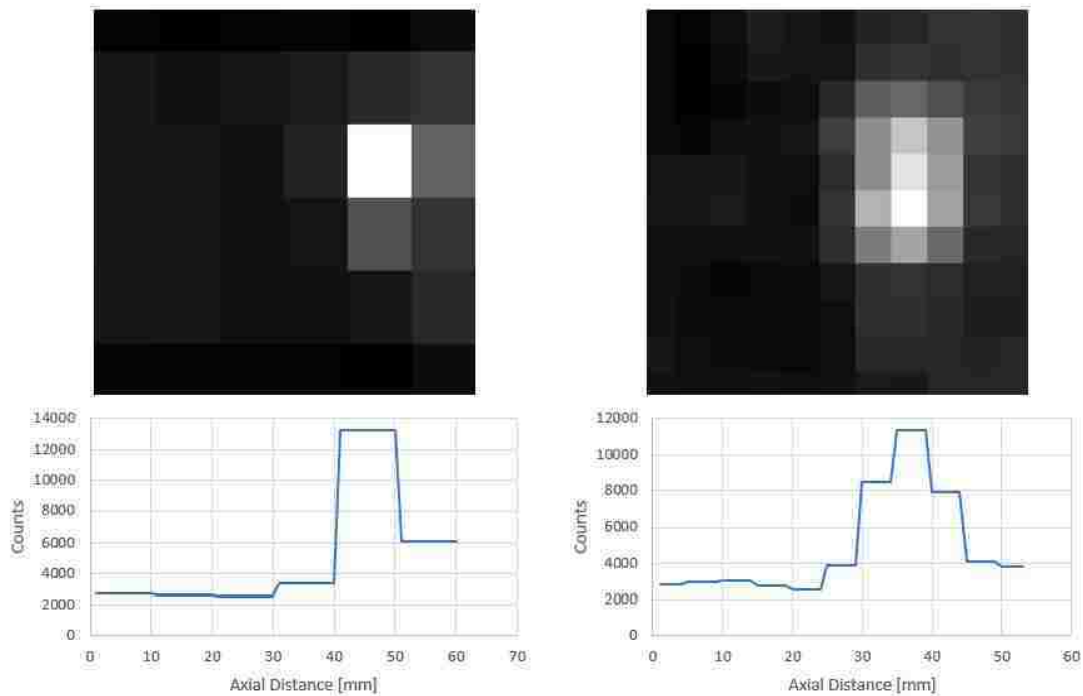
Figure 121: Top left: in focus reconstruction of Eu-251 using a 6 pixel spacing. Bottom left: one dimensional projection of reconstructed Eu-251 source with FWHM of 1.0 cm. Top right: defocused reconstruction of Eu-251 using a 5.5 pixel spacing. Bottom right: one dimensional projection of reconstructed Eu-251 source with a FWHM of 1.5 cm.

5.4 Conclusion of Pinhole Imager

We developed a multiple-pinhole imager for higher efficiency direct imaging of low energy gamma rays appropriate for passive spatial imaging of SNM. The lead pinhole masks were designed for varied uses, some of which were applicable to this experiment and some of which proved to not be. The modularity of this concept allowed for easy manipulation of the experimental set up. Masks that were too thin did not attenuate the source enough to generate usable images.

Single pinhole results yielded large and fairly resolved images. The most resolved images created in these experiments were from 1 mm, single pinhole images. The problem with this method that the images took a long time to create due to the lack of

135

geometric efficiency. There was also the problem that these images were subject to distortion due to the randomly varying responses from the pixels. Whether a pixel was dead or receiving a higher than normal count rate, these led to discrepancies with the image generated.

Using multiple pinholes increased the geometric efficiency and, though the sub-images were smaller, if the sub-images are placed to have different pixel representations of the images and thus different information, they can be added to a better resolution image than the individual sub-images. Having multiple sub-images also provided depth-of-field information from the sub-image spacing, so the imager not only produces two dimensional, x-y, images of distributed sources but brings in information on the 3rd dimension, z, of the source. Using a spectral detector allowed us to perform background subtraction and greatly improve the signal-to-noise ratio. It also allowed us to perform nuclide identification and treat different nuclides independently in the same data set, for example finding different distances. There are caveats with the imaging, if sub-images are spaced by an integer number of pixels then the sum images may be blocky. Also, if sub-images are not large enough the reconstruction will result in very poor resolution images.

Several parameters were tested. Varying the number of pinholes allows for higher resolution imaging but losing the ability to determine source distances while increasing the number of pinholes allows for distance determination but can limit the resolution. Wider pinhole diameters allow for larger sub-images and a higher detector efficiency but cause slight smudging and increase the chance of image overlap. The pinhole separation can have an effect on the range of the distance determination but must also keep the

images from overlapping or missing the detector. Thinner masks on the order of 1/32 in and 1/64 in would be useful for energies in the sub 100 keV range, possibly in application having to do with characteristic x-ray imaging. These thin masks would allow an increased field of view for energies that that do not penetrate the mask. The design of the detection system as well as validation of the proposed mathematical descriptions and characterization of the pixelated detector response was successful. Starting with the study of the attenuation of gamma rays and a selection of lead as the mask material which would be applicable for this system. The study of PRF, Equation 14, gave us an idea of the effects of pinhole size, source-to-mask distance as well as mask-to-detector distance on the resulting image from a point. These factors all must be balanced so that a sharp resolution image can be generated while retaining an efficiency which does not impede system performance. Equation 15 helped with the design of multiple pinhole masks to choose parameters when setting up the experiment so that detection area usage could be maximized. Modeling of a single pinhole system was done with a Monte Carlo based MATLAB code. This code was then compared to one dimensional cross section of experimental results generated by converting the nozzle collimated imaging system into a pinhole imaging system. The simulations as well as the mathematically theory agreed well with the experimental results.

The Kromek D-Matrix was then acquired and characterized. First the spectra were analyzed and it was noticed that not all 484 pixels responded in the same way with respect to spectrum channel location. This variation was slight and nullified using the spectra finding and background subtraction method of "method two" described in Section 2.3.3. An efficiency curve was generated for the detector showing how the response

137

varied with respect to the energy gamma ray. The full detector heatmap was response was then studied. This proved to result in varied responses over time from when the detector was turned on, over the four different modules of the detector and each of the pixels had widely varying responses as well. There was no way to account for these factors in a meaningful way. Luckily, when energy discrimination "method two" was applied to each of the spectra from the pixels the resulting heatmap were much more uniform. Large variances from pixel to pixel were minimized and module wide artifacts were negated. The signal to noise ratio was also increased by applying "method two" so this allowed for the images to come across as stronger on the detector. With the detector well understood the study of varying masks, experimental setups and image reconstructions could be begin.

5. Conclusions

Both detection systems, the collimated imager and the pixelated pinhole imager, were developed and characterized so that they produce images. Each system proved able to detect low energy radiation sources at a distance and above background levels. The calculations and simulations were validated and conformed to the experimental data gathered. Distances, both source-to-mask and mask to detector, play a large factor in the image spatial resolution as well as the ability for the detector to identify the sources. To perform standoff imaging the maximum useable source-to-detector distance was determined to be 50 cm for a 3.67 μCi source of Co-57. The distance of course will vary with nuclide and activity. These low energy sources emit radiation at comparable to that of SNM so it is feasible that these systems could be used in the field to image SNM. The collimated imager is prepared and nearly equipped to be taken into the field for non-laboratory experimental testing. The pixelated pinhole imager is not suitable for portable use at this time but the images produced are capable of underdoing image processing for reconstruction of the source. Future consolidation and data analysis techniques are required to streamline the imaging process. In their current state, these systems can identify and imaging SNM using low every gamma rays.

The nozzle collimated imager could detect and identify sources as well as create two dimensional images of their location. The system behaved as predicted by the governing mathematics and could be accurately modeled in MCNP. These simulations allowed for the production of a nozzle which was able to achieve less than 1 cm resolution at a source distance of 50 cm. Two different sources were identified and separated through post processing energy discrimination, proving the effectiveness of the

analysis codes. The background in the experimental lab as well as the detector responses were well characterized. A shortfall of this design is the collection time. With only one detector stopping at each point the time for collection is compounded and for low activity sources at far distances collection times could run into the hours. We developed a multiple-pinhole imager for higher efficiency direct imaging of low energy gamma rays appropriate for passive spatial imaging of SNM. The lead pinhole masks were designed for varied uses, some of which were applicable to this experiment and some of which proved to not be. The modularity of this concept allowed for easy manipulation of the experimental set up. Masks that were too thin did not attenuate the source enough to generate usable images.

Single pinhole results yielded large and fairly resolved images. The most resolved images created in these experiments were from 1 mm, single pinhole images. The problem with this method that the images took a long time to create due to the lack of geometric efficiency. There was also the problem that these images were subject to distortion due to the randomly varying responses from the pixels. Whether a pixel was dead or receiving a higher than normal count rate, these led to discrepancies with the image generated.

Using multiple pinholes increased the geometric efficiency and, though the sub-images were smaller, if the sub-images are placed to have different pixel representations of the images and thus different information, they can be added to a better resolution image than the individual sub-images. Having multiple sub-images also provided depth-of-field information from the sub-image spacing, so the imager not only produces two dimensional, x-y, images of distributed sources but brings in information on the 3rd

dimension, z, of the source. Using a spectral detector allowed us to perform background subtraction and greatly improve the signal-to-noise ratio. It also allowed us to perform nuclide identification and treat different nuclides independently in the same data set, for example finding different distances. There are caveats with the imaging, if sub-images are spaced by an integer number of pixels then the sum images may be blocky. Also, if sub-images are not large enough the reconstruction will result in very poor resolution images.

Several parameters were tested. Varying the number of pinholes allows for higher resolution imaging but losing the ability to determine source distances while increasing the number of pinholes allows for distance determination but can limit the resolution. Wider pinhole diameters allow for larger sub-images and a higher detector efficiency but cause slight smudging and increase the chance of image overlap. The pinhole separation can have an effect on the range of the distance determination but must also keep the images from overlapping or missing the detector. Thinner masks on the order of 1/32 in and 1/64 in would be useful for energies in the sub 100 keV range, possibly in application having to do with characteristic x-ray imaging. These thin masks would allow an increased field of view for energies that that do not penetrate the mask. The design of the detection system as well as validation of the proposed mathematical descriptions and characterization of the pixelated detector response was successful. Starting with the study of the attenuation of gamma rays and a selection of lead as the mask material which would be applicable for this system. The study of PRF, Equation 14, gave us an idea of the effects of pinhole size, source-to-mask distance as well as mask-to-detector distance on the resulting image from a point. These factors all must be balanced so that a sharp

141

resolution image can be generated while retaining an efficiency which does not impede system performance. Equation 15 helped with the design of multiple pinhole masks to choose parameters when setting up the experiment so that detection area usage could be maximized. Modeling of a single pinhole system was done with a Monte Carlo based MATLAB code. This code was then compared to one dimensional cross section of experimental results generated by converting the nozzle collimated imaging system into a pinhole imaging system. The simulations as well as the mathematically theory agreed well with the experimental results.

The Kromek D-Matrix was then acquired and characterized. First the spectra were analyzed and it was noticed that not all 484 pixels responded in the same way with respect to spectrum channel location. This variation was slight and nullified using the spectra finding and background subtraction method of "method two" described in Section 2.3.3. An efficiency curve was generated for the detector showing how the response varied with respect to the energy gamma ray. The full detector heatmap was response was then studied. This proved to result in varied responses over time from when the detector was turned on, over the four different modules of the detector and each of the pixels had widely varying responses as well. There was no way to account for these factors in a meaningful way. Luckily, when energy discrimination "method two" was applied to each of the spectra from the pixels the resulting heatmap were much more uniform. Large variances from pixel to pixel were minimized and module wide artifacts were negated. The signal to noise ratio was also increased by applying "method two" so this allowed for the images to come across as stronger on the detector. With the detector well understood

the study of varying masks, experimental setups and image reconstructions could be

begin.

6. Future Work

Additional data points would allow further insight into the applications of this detection system, there are many variables in this project and more data covering a variety of changes to every variable could allow for more in depth understanding of the system and accurate analysis. Kromek provides details for altering the API of their software many of these programs could be directly installed in the program used to image rather than utilizing other programs for analysis. It is possible that data acquisition, data analysis and image reconstruction could be integrated into a single interface. Changing the type of reconstruction algorithm could be used to determine the best algorithm over all for certain contexts. Analysis of shape could be used for this imaging. There are methods of measuring ellipticity, rectangularity, and triangularity and giving quantifiable numbers to how accurate a reconstruction is of the original shape. The D-Matrix detector can also be used in conjunction with different masks. Coded aperture is an often used masking system which could be implemented and directly compared to that of standard pinhole imaging. Deconvolution is used to in coded aperture imaging to produce a reconstructed image of the source, if the mask configuration in known. There should be an appropriate deconvolution method that could be used for pinhole image reconstruction that could be applied to this project. The addition of an auto peak finding and source identification feature would greatly benefit the usability of this system in the field. Finally, there can be improvements made to the portability of the collimated imager as well as conceptual designs made for a portable pinhole imaging system.

References

[1] M. Gatton and e. al., "The Camera Obscura and the Orgin of Art: The case for image projection in the Paleolithic," in *XV World Congress of the Union Internationale des Sciences Prehistoriques et Protohistoriques*, Oxford, 2010.

[2] J. Needham, Science and Civilisation in China, Cambridge : Cambridge University Press, 1962.

[3] P. Richter, The Notebooks of Leonardo da Vinci, Courier Corporation, 1883.

[4] F. Gemma, De Radio Astronomica et Geometrica, Belgium , 1554.

[5] F. Dierks, "Sensitivity and Image Quality of Digital Cameras," *Baserl Vision Technologies ,* 2004.

[6] L. Meitner and O. Frisch, "Disintegration of Uranium by Neutrons: A New Type of Nuclear Reaction," *Nature ,* vol. 143, 1939.

[7] R. Hewlett and O. Anderson, A History of the United States Atomic Energy Comission, vol. 1, Pennsylvania : The Pennsylvania State University Press , 1962.

[8] H. Truman, C. Attlee and W. King, "Atomic Energy," The White House, Washington, D.C., 1945.

[9] D. Acheson and D. Lilienthal, "A Report on the International Control of Atomic Energy," Washington, D.C., 1946.

[10] B. Baruch, "The Baruch Plan," United Nations, New York , 1946.

[11] D. Fischer, "History of the International Atomic Energy Agency," IAEA, Vienna, 1997.

[12] U. Nations, "Treaty on the Non-Proliferation of Nuclear Weapons," United Nations Office for Disarmerment Affairs, Ney York City, 1968.

[13] Danlaycock, Wiki Media Commons, 11 February 2014. [Online]. Available: https://commons.wikimedia.org/wiki/File:NPT_parties.svg. [Accessed 16 March 2017].

[14] U. Congress, "The Atomic Energy Act of 1954," Washington, D.C., 1954.

[15] T. Jevremovic, Nuclear Principles in Engineering, West Lafayette: Springer, 2005.

[16] D. Slaughter and e. al., "Detection of Special Nuclear Material in Cargo Container Using Neutron Interrogation," Lawrence Livermore National Lab , Livermore, 2003.

[17] A. Glaser, "Detection of Special Nuclear Material," Princeton University , Princeton , 2007.

[18] M. Nelson, "Dection of Special Nuclear Material With High Purity Germanium and Mercuric Iodide Gamma Detectors," Air Force Institute of Technology , Dayton, 2003.

[19] G. Gilmore R., Practical Gamma Ray Spectroscopy, Wiley, 2008.

[20] Amptek, "Uranium Energy Spectra," Amptek, Bedford, 2017.

[21] M. F. L'Annunziata, Radioactivity: Introduction and History, Amsterdam: Elserier B. V., 2007.

[22] K. J. Hofstetter and D. M. Beals, "Comparison of CdTe and CdZnTe Detectors for Field Determination of Uranium Isotopic Enrichments," Westinghouse Savannah River Company , Aiken , 2002.

[23] National Laboratory Henri Becquerel, "Library for gamma and alpha emissions," EDP Sciences, 3 March 2017. [Online]. Available: http://www.nucleide.org/Laraweb/.

[24] Nucleonica Wiki, "Decay Schemes," Nucleonica, 25 February 2015. [Online]. Available: http://www.nucleonica.net/wiki/index.php?title=Decay_Schemes.

[25] Echo, "Samples of CdTe and CdZnTe Detector Spectra," Kharkov Institute of Physics and Technology, 2017. [Online]. Available: http://www.kipt.kharkov.ua/kipt_sites/isspmst/nrdetectors/en/detectors/spectra/. [Accessed 27 February 2017].

[26] Nuclear Power , "Interaction of Gamma Radiation with Matter," [Online]. Available: http://www.nuclear-power.net/nuclear-power/reactor-physics/interaction-radiation-matter/interaction-gamma-radiation-matter/. [Accessed 21 March 2017].

[27] P. B. Rose and e. al., "Detection of Shielded Special Nuclear Material Using High Energy Gamma Ray".

[28] G. F. Knoll, Radiation Detection and Measurement, Hoboken: John Wiley & Sons, Inc., 2010.

[29] K. E. Nelson and e. al., "The Effect of Gamma-Ray Detector Energy Resolution on the Ability to Identify Radioactive Sources," Lawrence Livermore National Laboratry , Livermore, 2009.

[30] W. J. Price, Nuclear Radiation Detection, New York: McGraw-Hill Book Company , 1964.

[31] U. Lachish, "Semiconductor crystal optimmization of gamma detection," *Journal of Crystal Growth ,* vol. 225, pp. 114-117, 2001.

[32] Physics and Radio Electronics , "Extrinsic semiconductor," 2015. [Online]. Available: http://www.physics-and-radio-electronics.com/electronic-devices-and-circuits/semiconductor/extrinsic-semiconductor/n-type-semiconductor.html. [Accessed 4 April 2017].

[33] T. Takahashi and S. Watanabe, "Recent Progress in CdTe and CdZnTe Detectors," *IEEE Transaction on Nuclear Science ,* vol. 48, no. 4, 2001.

[34] S. Del Sordo and e. al., "Progress in the Development of CdTe and CdZnTe Semiconductor Radiation Detectors for Astrophysical and Medical Applications," Multidisciplinary Digital Publishing Institute, Basel, 2009.

[35] P. Franc and e. al., "CdTe and CdZnTe crystals for room temperature gamma-ray detectors," *Nuclear Insturments & Methods in Physics Research A,* vol. 434, pp. 146-151, 1999.

[36] T. Schlesinger and e. al., "Cadmium zinc telluride and its use as a nuclear radiation detector material," *Materials Science and Engineering,* vol. 32, pp. 103-189, 2001.

[37] Z. Szajnfarber, "The Cadmium Zinc Telluride (CZT) Detector Array Innovation Pathway," Massachusetts Institute of Technology , Cambridge , 2011.

[38] P. DeRego, "A model-based multiple pinhole synthetic iager for stand-off range gamma emitting objects," in *SPIE OPtics and PHotonics Conference* , San Diego , 2016.

[39] L. E. Wahl, "Environmental Radiation," Health Physics Society , McLean, 2010.

[40] Amptek, "X-ray Fluorescence (XRF): Understanding Characteristic X-rays," Amptek.

[41] L. A. Curie, "Limits for Qualitative Detection and Quantification Determination," *Analytical Chemistry* , vol. 40, pp. 586-593, 1968.

[42] Amptek, "XR-100T-CdTe X-ray & Gamma Ray Detector," Amptek, [Online]. Available: http://amptek.com/products/xr-100t-cdte-x-ray-and-gamma-ray-detector/#6. [Accessed 2013].

[43] J. H. Hubbell and S. m. Seltzer, "NIST Standard Reference Simulation Website," National Institute of Standards and Technology, July 2004. [Online]. Available: https://www.nist.gov/pml/x-ray-mass-attenuation-coefficients. [Accessed 2015].

[44] S. Dodds, "Pinhole Optics," Rice University , Houston, 2006.

[45] Nucleonica, "Decay Schemes," Karlsruhe Nuclide Chart, 25 February 2015. [Online]. Available: https://www.nucleonica.com/wiki/index.php?title=Decay_Schemes. [Accessed 1 March 2017].

[46] J. Taylor, An Introduction to Error Analysis, Sausalito: University Science Books , 1997.

[47] M. A. Askari, "Assessment of radiological hazard of NORM in Margalla Hills limestone, Pakistan," *Environmental Monitoring and Assessment* , 2011.

Appendix

Appendix A (Resolution Determination MCNP Code)

```
(50cm from detector, 4cm diam. disk) Collimator + Real CdTe
c Created on 02/15/15
c
c Made by: Phoenix Baldez
c For: Lab Experiemnts
c
c
=====================================================================
c ==================== Cell Cards ================================
c =====================================================================
c
1    1    -2.6989   -1:-3:-4 2          imp:p=1      $ Aluminum case
2    2    -3.667    -2               imp:p=1      $ CdTe crystal
c
3    3    -11.34    6 -7    imp:p=1               $ Tungsten collimator
c
4    4    -8.96     5 -6             imp:p=1      $ Copper Lining
c
10   100   -0.001205  -10 #1 #2 #3 #4      imp:p=1      $ Air fill
c
c -------------------- Dead Zone ----------------------------------------
c
11   0            10             imp:p=0      $ dead zone
c
c +++++++++++++++++++ Blank Line Follows +++++++++++++++++++++++++++

c ====================================================================
c ==================== Surface Cards ============================
c ====================================================================
c
c -------------------- Detector ----------------------------------------
c
1  1  RPP  -7.62 0      -1.4224 1.4224  -2.2225 2.2225   $ Detector case
2  1  RPP  4.5736 4.6736  -0.531 -0.231 -1.3565 -1.0565  $ Crystal
c
3  1  RCC 0   -0.381 -1.2065  3.81  0 0  0.889       $ First section of extender
4  1  RCC  3.81 -0.381 -1.2065  0.8636 0 0  0.6985    $ Second section of extender
c
5  1  RCC  3.81 -0.381 -1.2065  15.8636 0 0  0.6985    $ Inside Copper Layer
6  1  RCC  3.81 -0.381 -1.2065  15.8636 0 0  0.7985    $ Outside Copper Layer
```

```
7   1   RCC  3.81 -0.381 -1.2065   15.8636 0 0  0.8985     $ Outside Tungsten
c
c -------------------- Boundries --------------------------------------------
c
10    RPP -1000 1000   -1000 1000   -1000 1000
c
c ++++++++++++++++++++ Blank Line Follows ++++++++++++++++++++++++++

c =================================================================
c ==================== Data Cards =================================
c =================================================================
c
c -------------------- Tally ----------------------------------------------
c
F8:p 2
E8 1e-6 2047i 0.6
c
c -------------------- Transformation -------------------------------------
c      B (1-9) Rotation matrix
c
c  x y z  1 2 3  4 5 6  7 8 9  M
TR1 0 0 0  1 0 0  0 1 0  0 0 1  1            $ Detector
c
c -------------------- Disk Source ------------------------------------------
c
c Am-241 + U Nat (5cm Diameter Disk Source)
SDEF par=2 pos=50 -0.381 -1.2065 rad=d1 ext=0 axs=1 0 0 vec=-1 0 0
    dir=1 erg=0.086
si1   -2.0    2.0
sp1   -21     1
c
c -------------------- Physics ----------------------------------------------
c
mode p
phys:p 100 0 0 0 0
c
c 20uCi Source for 0.61min
nps 2.72e7
c
c -------------------- Material ----------------------------------------------
c
c Air
m100   6000      -0.000124    $ Carbon
      7000      -0.755288    $ Nitrogen 14
      8000      -0.231781    $ Oxygen 16
      18000     -0.012827    $ Argon
```

```
c
c Aluminum Casing
m1    13000    -1.0       $ Aluminum
c
c CdTe Crystal
m2    48000     -0.468355   $ Cd
      52000     -0.531645   $ Te
c
m3    74000     -1.0       $ W
c
m4    29000     -1.0       $ Cu
c
c +++++++++++++++++++ Blank Line Follows ++++++++++++++++++++++++++
```

Appendix B (Simulation MATLAB Code)

```
% 1D imaging simulation
% Point/line Source emitting rays which are either collimated (go to 0)
% or hit the detector (value of 1)
%      x
%   |-----       Detector
% y |             _____
%   |
%      ----------- -----------
%      Collimator
%
%
%                  *
%               Source
%       <---- (-)    (+) ---->
clear
clc

number = 110000; % number of gammas to be emitted
sourceSize = 0; % how wide the source is in cm, source size = 0 means
point source
gamAngle = 90; % +/- angle the gammas are to be randomly emitted over,
in degrees
% use gamAngle to decrease culculation time when you only care about a
% narrow angle

CT = 0.6; % Collimator thickness in cm
murho = 0.4862; % mu/rho for Cu at 40 keV from NIST database in cm^2/g
rho = 8.96; % density of Fe in g/cm^3
mu = murho*rho; % attenuation coefficient
PW = 2.54/8; % pinhole width in cm

SO = 0; % source offset from center of collimator in cm
SC = 1.5; % source to collimator distance in cm
```

```matlab
CD = 1.5; % colliamtor to detector distance in cm

detLocV = zeros([1 number]); % Creates a vector with correct number of
spaces for each particle

maxSO =  (PW/CT)*SC;   % max angle to have clear LOS to pinhole

count = 0;  %the count for determining efficiency

i=1;
for i = 1:number

    % Source size determination
    if sourceSize == 0
        gamStart = SO; % point source
    else
        gamStart = SO-(sourceSize/2)+sourceSize*rand; % line source,
emits
            %particles at random point along a line to simulate line
source
    end

    randAngle = -gamAngle+(2*gamAngle)*rand; % random angle in degrees


% h = length the particle must travel thru the collimator to pass thru
% prob = probability that particle gets thru the collimator material
% detLoc = the location on the detector that the particle impacts
%


%--------------------in pinhole---------------------------------------
----

    if gamStart > -PW/2 && gamStart < PW/2 % source is offset but not
beyond pinhole
        thetaA = atand((PW/2-gamStart)/(SC+CT)); % bottom right corner
        thetaB = -atand((PW/2+gamStart)/(SC+CT)); % bottom left corner
        thetaC = atand((PW/2-gamStart)/(SC)); % top right corner
        thetaD = -atand((PW/2+gamStart)/(SC)); % top left corner
% misses pinhole entirely
        if randAngle > thetaC || randAngle < thetaD
            h = CT/cosd(abs(randAngle)); % length to travel thru
collimator
            prob1 = exp(-mu*h); % probability of penetration
            if prob1 > rand
                detLoc = (SC+CD+CT)*tand(randAngle); % detector
location if ray gets thru
            else
                detLoc = 0;
            end

% gets thru and impact detector
        elseif randAngle > thetaB && randAngle < thetaA
            detLoc = (SC+CD+CT)*tand(randAngle);
```

```matlab
            count = count + 1;


% hits right side of pinhole
        elseif randAngle > thetaA && randAngle < thetaC
            h = ((abs(randAngle)/abs(thetaC))*CT)/cosd(abs(randAngle));
            prob2 = exp(-mu*h);
            if prob2 > rand
                detLoc = (SC+CD+CT)*tand(randAngle);
            else
                detLoc = 0;
            end

% hits left side of pinhole
        elseif randAngle > thetaD && randAngle < thetaB
            h = ((abs(randAngle)/abs(thetaD))*CT)/cosd(abs(randAngle));
            prob2 = exp(-mu*h);
            if prob2 > rand
                detLoc = (SC+CD+CT)*tand(randAngle);
            else
                detLoc = 0;
            end

        else
            detLoc = 0;
        end

%_____
____
% ---------------------positive----------------------------------------
----

    elseif gamStart > PW/2
        thetaA = -atand((gamStart-PW/2)/(SC+CT));
        thetaB = -atand((gamStart+PW/2)/(SC+CT));
        thetaC = -atand((gamStart-PW/2)/(SC));
        thetaD = -atand((gamStart+PW/2)/(SC));

%-------------Direct shine on detector
        if gamStart <= maxSO
% misses pinhole entirely
            if randAngle > thetaA || randAngle < thetaD
                h = CT/cosd(abs(randAngle));
                prob1 = exp(-mu*h);
                if prob1 > rand
                    detLoc = (SC+CD+CT)*tand(randAngle);
                else
                    detLoc = 0;
                end

% gets thru and impact detector
            elseif randAngle > thetaB && randAngle < thetaC
                detLoc = (SC+CD+CT)*tand(randAngle);
                count = count + 1;
```

152

```matlab
% hits thru right side of pinhole
            elseif randAngle > thetaC && randAngle < thetaA
                h = ((randAngle/abs(thetaC))*CT)/cosd(randAngle);
                prob2 = exp(-mu*h);
                if prob2 > rand
                    detLoc = (SC+CD+CT)*tand(randAngle);
                else
                    detLoc = 0;
                end

% hits left side of pinhole
            elseif randAngle > thetaD && randAngle < thetaB
                h = ((randAngle/abs(thetaD))*CT)/cosd(randAngle);
                prob2 = exp(-mu*h);
                if prob2 > rand
                    detLoc = (SC+CD+CT)*tand(randAngle);
                else
                    detLoc = 0;
                end

            else
                detLoc = 0;
            end

%-------------no direct shine on detector
        else
 % misses pinhole entirely
            if randAngle > thetaA || randAngle < thetaD
                h = CT/cosd(abs(randAngle));
                prob1 = exp(-mu*h);
                if prob1 > rand
                    detLoc = (SC+CD+CT)*tand(randAngle);
                else
                    detLoc = 0;
                end

% hits both sides of collimator
            elseif randAngle > thetaC && randAngle < thetaB
                h =
(((randAngle/abs(thetaC))*CT)/cosd(randAngle))+(((randAngle/thetaD)*CT)
/cosd(randAngle));
                prob2 = exp(-mu*h);
                if prob2 > rand
                    detLoc = (SC+CD+CT)*tand(randAngle);
                else
                    detLoc = 0;
                end

% hits thru right side of pinhole
            elseif randAngle > thetaB && randAngle < thetaA
                h = ((randAngle/abs(thetaC))*CT)/cosd(randAngle);
                prob2 = exp(-mu*h);
                if prob2 > rand
                    detLoc = (SC+CD+CT)*tand(randAngle);
                else
                    detLoc = 0;
```

153

```matlab
                end

% hits left side of pinhole
            elseif randAngle > thetaD && randAngle < thetaC
                h = ((randAngle/abs(thetaD))*CT)/cosd(randAngle);
                prob2 = exp(-mu*h);
                if prob2 > rand
                    detLoc = (SC+CD+CT)*tand(randAngle);
                else
                    detLoc = 0;
                end

            else
                detLoc = 0;
            end
        end

%_____
____
% ---------------------negative----------------------------------
----
    elseif gamStart <= -PW/2
        thetaA = atand((gamStart+PW/2)/(SC+CT));
        thetaB = atand((gamStart-PW/2)/(SC+CT));
        thetaC = atand((gamStart+PW/2)/(SC));
        thetaD = atand((gamStart-PW/2)/(SC));

%-------------Direct shine on detector
        if gamStart >= -maxSO
% misses pinhole entirely
            if randAngle > thetaC || randAngle < thetaB
                h = CT/cosd(abs(randAngle));
                prob1 = exp(-mu*h);
                if prob1 > rand
                    detLoc = (SC+CD+CT)*tand(randAngle);
                else
                    detLoc = 0;
                end

% hits both sides of collimator
            elseif randAngle > thetaD && randAngle < thetaA
                detLoc = (SC+CD+CT)*tand(randAngle);
                count = count + 1;

% hits thru right side of pinhole
            elseif randAngle > thetaA && randAngle < thetaC
                h = ((randAngle/abs(thetaC))*CT)/cosd(randAngle);
                prob2 = exp(-mu*h);
                if prob2 > rand
                    detLoc = (SC+CD+CT)*tand(randAngle);
                else
                    detLoc = 0;
                end

% hits left side of pinhole
```

154

```matlab
            elseif randAngle > thetaB && randAngle < thetaD
                h = ((randAngle/abs(thetaD))*CT)/cosd(randAngle);
                prob2 = exp(-mu*h);
                if prob2 > rand
                    detLoc = (SC+CD+CT)*tand(randAngle);
                else
                    detLoc = 0;
                end

            else
                detLoc = 0;
            end

%-------------No direct shine on detector
        else
% misses pinhole entirely
            if randAngle > thetaC || randAngle < thetaB
                h = CT/cosd(abs(randAngle));
                prob1 = exp(-mu*h);
                if prob1 > rand
                    detLoc = (SC+CD+CT)*tand(randAngle);
                else
                    detLoc = 0;
                end

% hits both sides of collimator
            elseif randAngle > thetaA && randAngle < thetaD
                h =
(((randAngle/abs(thetaD))*CT)/cosd(randAngle))+(((randAngle/thetaC)*CT)
/cosd(randAngle));
                prob2 = exp(-mu*h);
                if prob2 > rand
                    detLoc = (SC+CD+CT)*tand(randAngle);
                else
                    detLoc = 0;
                end

% hits thru right side of pinhole
            elseif randAngle > thetaD && randAngle < thetaC
                h = ((randAngle/abs(thetaC))*CT)/cosd(randAngle);
                prob2 = exp(-mu*h);
                if prob2 > rand
                    detLoc = (SC+CD+CT)*tand(randAngle);
                else
                    detLoc = 0;
                end

% hits left side of pinhole
            elseif randAngle > thetaB && randAngle < thetaA
                h = ((randAngle/abs(thetaD))*CT)/cosd(randAngle);
                prob2 = exp(-mu*h);
                if prob2 > rand
                    detLoc = (SC+CD+CT)*tand(randAngle);
                else
                    detLoc = 0;
                end
```

```matlab
            else
                detLoc = 0;
            end
        end
    end
detLocV(i) = detLoc;
end



fprintf('ADD AN IMAGE SIZE CALCULATION \n');
% efficiency calculated as the number of particles that pass thru the
% pinhole without interacting in the collimator and assumes that there
is a
% 360 degree emission of particles from the source (no matter what
gamAngle
% was chosen, gamAngle is only used to direct the particle emmision to
% decrease calculation time
eff = ((count/number)*100)*((gamAngle*2)/360);
fprintf('Efficiency: %.2f%% \n', eff);


detLocV = detLocV(detLocV~=0); % take out all 0 values
histogram(detLocV, -2:0.2:2);

% % First graph
% hold on
% xaxis = [-7.5:0.5:7.5];
% yaxis = [19, 29, 61, 89, 94, 125, 160, 197, 236, 229, 305, 275, 309,
317,...
%     387, 381, 434, 399, 388, 412, 359, 332, 351, 265, 281, 249, 194,
166,...
%     174, 116, 95];
% plot(xaxis, yaxis);
%
% title('1/4in Pinhole, Source On Collimator Face, 5mm Steps, Full
Scan')
% xlabel('Distance [cm]')
% ylabel('Counts')
% legend('Simulation','Experimental Data')
%
% % Second graph
% hold on
% xaxis = [-7.5:0.5:7.5];
% yaxis = [2, 11, 9, 10, 10, 7, 13, 15, 14, 21, 29, 29, 43, 60, 64, 85,
75,...
%     74, 67, 72, 71, 62, 45, 35, 28, 30, 19, 25, 22, 22, 13];
% plot(xaxis, yaxis);
%
% title('1/8in Pinhole, Source On Collimator Face, 5mm Steps, Full
Scan')
% xlabel('Distance [cm]')
% ylabel('Counts')
% legend('Simulation','Experimental Data')

% % Third graph
% hold on
```

```
% xaxis = [-6.5:0.5:8.5];
% yaxis = [7, 4, 3, 7, 5, 13, 3, 5, 9, 10, 10, 17, 35, 24, 7, 10, 6, 7,
10,...
%      9, 9, 8, 10, 8, 13, 8, 6, 7, 13 16, 14];
% plot(xaxis, yaxis);
%
% title('1/8in Pinhole, Source 16cm from Collimator, 5mm Steps, Full
Scan')
% xlabel('Distance [cm]')
% ylabel('Counts')
% legend('Simulation','Experimental Data')

% % Fourth graph
% hold on
% xaxis = [-1.5:0.1:1.5];
% yaxis = [4, 6, 11, 5, 5, 5, 9, 12, 33, 35, 90, 92, 96, 98, 124, 121,
115,...
%      100, 109, 95, 94, 57, 39, 24, 20, 5, 10, 8, 11, 3, 2];
% plot(xaxis, yaxis);
%
% title('1/4in Pinhole, Source 16cm from Collimator, 1mm Steps')
% xlabel('Distance [cm]')
% ylabel('Counts')
% legend('Simulation','Experimental Data')

% % Fifth graph
% hold on
% xaxis = [-1.5:0.1:1.5];
% yaxis = [4, 6, 11, 5, 5, 5, 9, 12, 33, 35, 90, 92, 96, 98, 124, 121,
115,...
%      100, 109, 95, 94, 57, 39, 24, 20, 5, 10, 8, 11, 3, 2];
% plot(xaxis, yaxis);
%
% title('1/4in Pinhole, Source 16cm from Collimator, 1mm Steps')
% xlabel('Distance [cm]')
% ylabel('Counts')
% legend('Simulation','Experimental Data')
```

Appendix C (MATLAB Energy Discrimination and Reconstruction Code)

```
% Program to sort the DMatrix data files
% By Phoenix Baldez
clear
clc

% loads raw data
filenameCSV = '/Users/Imaging/Dropbox/Public/School/Grad/Hecht
Lab/Gamma Spec
Project/Data/DMatrix/2017/113017_EuReDo/113017_Eu152_5cm_2hrs.csv';
data = csvread(filenameCSV, 1, 0); % data is full data matrix
data = data(:,5:6); % only names pixel and channel information

lines = length(data); % number of lines in data file
spectMat = zeros(484,4096); % empty matrix for spectrum data
```

157

```matlab
for i = 1:lines
    j = data(i,1);
    if j == 111 || j == 132 || j == 374 || j == 353 % bad pixels
        k = 1;
        spectMat(j,k) = 0; % setting bad pixels to 0 counts
    elseif j < 485
        k = data(i,2);
        if k == 4095 % this ch on every pixel has a lot of junk so set
to 0
            spectMat(j,k) = 0;
        end
        spectMat(j,k)=spectMat(j,k)+1; % spectrum of every pixel
    end
end

%% BG File Subtract
%loads raw BG data
filenameCSVBG = '/Users/Imaging/Dropbox/Public/School/Grad/Hecht
Lab/Gamma Spec
Project/Data/DMatrix/2017/10112017_PinholeOptimization/10112017_Pinhole
Optimization_BG_30min.csv';
BGdata = csvread(filenameCSVBG, 1, 0); % data is full data matrix
BGdata = BGdata(:,5:6); % only names pixel and channel information

BGlines = length(BGdata); % number of lines in data file
BGspectMat = zeros(484,4096); % empty matrix for spectrum data

for i = 1:BGlines
    j = BGdata(i,1);
    if j == 111 || j == 132 || j == 374 || j == 353 % bad pixels
        k = 1;
        BGspectMat(j,k) = 0; % setting bad pixels to 0 counts
    elseif j < 485
        k = BGdata(i,2);
        if k == 4095 % this ch on every pixel has a lot of junk so set
to 0
            BGspectMat(j,k) = 0;
        end
        BGspectMat(j,k)=BGspectMat(j,k)+1; % spectrum of every pixel
    end
end

% Subtracts every point of BG from every real data point
for i = 1:484
    for j = 1:4096
        spectMat(i,j) = spectMat(i,j)-(BGspectMat(i,j)*4); % THIS *4 IS
VERY IMPORTANT, TO GET SAME TIME (4hrs run with 1hr BG)
    end
end

%% Peak Find and Trapazoid Subtraction, HeatMap

% 800-900 Am-241
% 1200-1300 Co-57/Eu-152
```

```matlab
% 700-800 Eu-152
% 950-1050 Ba-133
maxMat = zeros(1,484); % array of all max ch #s
val = zeros(1,484); % the value of max
pos = zeros(1,484); % the position of max
chStart = 900; % start of peak finding channel
chStop = 1000; % end of peak finding channel
sumCount = zeros(1,484); % sum of counts in the peak in pixel #
pixelCount = zeros(22); % 22x22 representation of the detector
BGdif = 20; % number of channels above/below the peak value to count/
*THIS SHOULD STAY 20, Full Width Base
BGavgNum = 50; % The number of channels used to calc the avg of BG on
either side

for i = 1:484
    [val,pos] = max(spectMat(i,chStart:chStop)); % value and position of
the maximums from each pixel
%    maxMat(i) = pos; % fills array of max ch #s
    pos = pos+chStart; % add back the start ch value, +800
    lowLim = pos-BGdif; % lower limit of peak find ASSUMING 40ch total
base width
    upLim = pos+BGdif; % upper limit of peak find
    sumCount = sum(spectMat(i,lowLim:upLim)); % sum all counts between
lower and upper limit

    lowBGLow = lowLim-BGavgNum; % low limit that low avg will be calced
from
    lowBGHigh = lowLim; % high limit that low avg will be calced from
    highBGHigh = upLim+BGavgNum; % high limit that high avg will be
calced from
    highBGLow = upLim; % low limit that high avg will be calced from

    BGbase = BGdif*2; % width of base of trapazoid
    lowBG = mean(spectMat(lowBGLow:lowBGHigh)); % y1
    highBG = mean(spectMat(highBGLow:highBGHigh)); % y2

    trapazoid = .5*BGbase*(lowBG+highBG); % area of trapazoid to
subtract

    pixelCount(i) = sumCount - trapazoid; % subtracting the trapazoid
end

pixelCount = rot90(pixelCount,3); % rotates the matrix 270 degrees so
that it is properly oriented
pixelCount = fliplr(pixelCount); % flips for proper orientation

% Excel file to produce heatmap
% OUTPUT to the samae location as this program is located NOT to the
.csv location
filenameCSV = '10112017_PinholeOptimization_Co57_30min_CD3_CS5.csv';
csvwrite(filenameCSV,pixelCount);

% filenameXLS = 'C:\Users\Phoenix\Dropbox\Public\School\Grad\Hecht
Lab\Gamma Spec
```

```matlab
Project\Data\DMatrix\120116_Thin\120116_64th_Co57_SC5cm_CD5cm_30min_max
Mat.xls';
% xlswrite(filenameXLS,maxMat)


%% Simple HeatMap

% 800-900 Am-241
% 1200-1300 Co-57
% 950-1050 Ba-133
chStart = 950; % start of peak finding channel
chStop = 1050; % end of peak finding channel
val = zeros(1,484);
pos = zeros(1,484);
sumCount = zeros(22);

for i = 1:484
    sumCount(i) = sum(spectMat(i,chStart:chStop)); % sum all counts
between lower and upper limit
end

pixelCount = rot90(sumCount,3); % rotates the matrix 270 degrees so
that it is properly oriented
pixelCount = fliplr(pixelCount); % flips for proper orientation

filenameCSVheatmap =
'10112017_PinholeOptimization_Co57_30min_CD3_CS5.csv';
csvwrite(filenameCSVheatmap, pixelCount);



%% Image Reconstruction

imageMap = zeros(500);
dividerMap = zeros(500);
pixelDim = 10;
mappingStepSizeX = 55;
mappingStepSizeY = 55;

for q = 1:4
    for p = 1:4
        for i = 1:22
            for j = 1:22
                value = pixelCount(i,j);
                for k = 1: pixelDim
                    for l = 1: pixelDim
                        m = pixelDim * (i-1)+(k)+(p-
1)*mappingStepSizeX;
                        n = pixelDim * (j-1)+(l)+(q-
1)*mappingStepSizeY;
                        mm = m;
                        nn = n;
                        imageMap(m,n) = imageMap(m,n) + value;
                        if value > 0
                            dividerMap(mm,nn) = dividerMap(mm,nn) + 1;
                        end
```

```matlab
                    end
                end
            end
        end
    end
end

filenameCSV = ...
'10112017_PinholeOptimization_Co57_30min_CD3_CS5_ImageMap.csv';
csvwrite(filenameCSV, imageMap);


map = HeatMap(imageMap, 'Colormap', redbluecmap(64));
% map2 = HeatMap(dividerMap, 'Colormap', redbluecmap(64));


averageMap = imageMap./dividerMap;

% map3 = HeatMap(averageMap, 'Colormap', redbluecmap(64));
%
singleImage = zeros(mappingStepSizeX+10);
for r = 1:mappingStepSizeX
    for s = 1: mappingStepSizeY
        t = 3*mappingStepSizeX+r;
        u = 3*mappingStepSizeY+s; % 3 refers to the number of pinholes
minus one
        singleImage(r,s) = averageMap(t,u);
    end
end

filenameCSV = ...
'10112017_PinholeOptimization_Co57_30min_CD3_CS5_SingleImageMap.csv';
csvwrite(filenameCSV, singleImage);


HM = HeatMap(singleImage, 'Colormap', redbluecmap(64));
```

Appendix D (D-Matrix Full System Simulation)

```
Full DMatrix System Simulation
c Created on February, 2017
c
c Made by: Phoenix Baldez
c For: Comparison of experimental system with simulations
c
c ================================================================
c ==================== Cell Cards ================================
c ================================================================
c
c ------------------------ Detector ------------------------------
c
1   1  -6.2    -1    imp:p=1  u=1          $ CZT
c
```

```
6   100 -.001205   1    imp:p=1 u=1          $ Air
c
2   100 -0.001205 -1     imp:p=1 u=2 lat=1       $ Detector pixel fill
    fill= -10:11 -10:11 0:0
    1 1 1 1 1 1 1 1 1 1 1 1 1 1 1 1 1 1 1 1 1 1
    1 1 1 1 1 1 1 1 1 1 1 1 1 1 1 1 1 1 1 1 1 1
    1 1 1 1 1 1 1 1 1 1 1 1 1 1 1 1 1 1 1 1 1 1
    1 1 1 1 1 1 1 1 1 1 1 1 1 1 1 1 1 1 1 1 1 1
    1 1 1 1 1 1 1 1 1 1 1 1 1 1 1 1 1 1 1 1 1 1
    1 1 1 1 1 1 1 1 1 1 1 1 1 1 1 1 1 1 1 1 1 1
    1 1 1 1 1 1 1 1 1 1 1 1 1 1 1 1 1 1 1 1 1 1
    1 1 1 1 1 1 1 1 1 1 1 1 1 1 1 1 1 1 1 1 1 1
    1 1 1 1 1 1 1 1 1 1 1 1 1 1 1 1 1 1 1 1 1 1
    1 1 1 1 1 1 1 1 1 1 1 1 1 1 1 1 1 1 1 1 1 1
    1 1 1 1 1 1 1 1 1 1 1 1 1 1 1 1 1 1 1 1 1 1
    1 1 1 1 1 1 1 1 1 1 1 1 1 1 1 1 1 1 1 1 1 1
    1 1 1 1 1 1 1 1 1 1 1 1 1 1 1 1 1 1 1 1 1 1
    1 1 1 1 1 1 1 1 1 1 1 1 1 1 1 1 1 1 1 1 1 1
    1 1 1 1 1 1 1 1 1 1 1 1 1 1 1 1 1 1 1 1 1 1
    1 1 1 1 1 1 1 1 1 1 1 1 1 1 1 1 1 1 1 1 1 1
    1 1 1 1 1 1 1 1 1 1 1 1 1 1 1 1 1 1 1 1 1 1
    1 1 1 1 1 1 1 1 1 1 1 1 1 1 1 1 1 1 1 1 1 1
    1 1 1 1 1 1 1 1 1 1 1 1 1 1 1 1 1 1 1 1 1 1
    1 1 1 1 1 1 1 1 1 1 1 1 1 1 1 1 1 1 1 1 1 1
    1 1 1 1 1 1 1 1 1 1 1 1 1 1 1 1 1 1 1 1 1 1
    1 1 1 1 1 1 1 1 1 1 1 1 1 1 1 1 1 1 1 1 1 1
c
3   100 -0.001205 -2     imp:p=1   u=0 fill=2   $ Fill universe
c
c ------------------------- Carbon Fiber Mask --------------------------------
c
4   3  -1.184    -4    imp:p=1 u=0       $ PAN (carbon fiber)
c
c ------------------------- Lead Pinhole Collimator --------------------------
c
5   4  -11.35    -5  21 22 23 24 25 26 27 28 29 30 31 32 33 34 35 36
              imp:p=1  u=0        $ Pb pinhole collimator
c
c ------------------------- Lead Triangle Shaper ----------------------------
c
7   4  -11.35    -50 51  imp:p=1 u=0       $ Triangle source shaper
c
c ------------------------ Air/Void ----------------------------------------
c
10   100   -0.001205  -10 #1 #2 #3 #4 #5 #7 imp:p=1 u=0     $ air
c
```

```
11  0      10   imp:p=0      $ void
c
c ++++++++++++++++++ Blank Line Follows ++++++++++++++++++++++++
c
c ================================================================
c ==================== Surface Cards ============================
c ================================================================
c
c ------------------------- Detector -----------------------------------------
c
1 1 RPP    0.0 0.2     0.0 0.2    0.0 1.0     $ Single pixel
c
2 1 RPP   -2.0 2.4   -2.0 2.4     0.0 1.0       $ Full detector
c
c
c ------------------------ Carbon Fiber Mask -------------------------------
c
4  1 RPP -3.65 4.05   -3.65 4.05    3.0 3.15
c
c ------------------------ Lead Pinhole Collimator -------------------------
c
c  1/8th inch                    \/ offset provided in tr card
5  2 RPP    -4.25 4.25   -4.25 4.25     0.0 0.3175
c
c  1/32th inch
c 5  2 RPP    -4.25 4.25   -4.25 4.25     0.0 0.07938
c
c  1/64th inch
c 5  2 RPP    -4.25 4.25   -4.25 4.25     0.0 0.03969
c
c              Collimator Holes
c
21 3  RCC -1.5  1.5 0   0 0 0.3175  0.05
22 3  RCC -0.5  1.5 0   0 0 0.3175  0.05
23 3  RCC  0.5  1.5 0   0 0 0.3175  0.05
24 3  RCC  1.5  1.5 0   0 0 0.3175  0.05
25 3  RCC -1.5  0.5 0   0 0 0.3175  0.05
26 3  RCC -0.5  0.5 0   0 0 0.3175  0.05
27 3  RCC  0.5  0.5 0   0 0 0.3175  0.05
28 3  RCC  1.5  0.5 0   0 0 0.3175  0.05
29 3  RCC -1.5 -0.5 0   0 0 0.3175  0.05
30 3  RCC -0.5 -0.5 0   0 0 0.3175  0.05
31 3  RCC  0.5 -0.5 0   0 0 0.3175  0.05
32 3  RCC  1.5 -0.5 0   0 0 0.3175  0.05
33 3  RCC -1.5 -1.5 0   0 0 0.3175  0.05
34 3  RCC -0.5 -1.5 0   0 0 0.3175  0.05
```

```
35 3  RCC   0.5 -1.5 0   0 0 0.3175  0.05
36 3  RCC   1.5 -1.5 0   0 0 0.3175  0.05
c
c ------------------------- Lead Triangle Shaper ----------------------------
c
50 4  RPP    -4.25 4.25    -4.25 4.25      0.0 0.3175  $ Pb shield
c
c        A1          A2          B1          B2
51 4  ARB  -0.79 -0.5 0   -0.79 -0.5 0.3175   0.79 -0.5 0   0.79 -0.5 0.3175
c        C1       C2          unused
       0 0.89 0   0 0.89 0.3175   0 0 0   0 0 0
c
         1234 1256 3456 1350 2460 0000
c
c ------------------------- Problem Boundary --------------------------------
c
10  RPP   -1000 1000  -1000 1000  -1000 1000
c
c ++++++++++++++++++++ Blank Line Follows ++++++++++++++++++++++++++

c ===================================================================
c ==================== Data Cards ===================================
c ===================================================================
c
c ------------------------- Source ------------------------------------------
c
SDEF POS=0.2 0.2 11.3175 AXS=0 0 1 EXT=0 RAD=d1 PAR=2 ERG=0.12206065
SI1 0 1.6
SP1 -21 1
c
c ------------------------- Tally -------------------------------------------
c
F8:p 1           $ Tally of the spectrum
E8 1e-8 2047i 0.6      $ 2048 divisions to make 2048 channels from 1eV-600 keV
c
F4:p  1
FMESH14:p GEOM = xyz ORIGIN = -2.0 -2.0 0
     IMESH = 2.4  IINTS = 22
     JMESH = 2.4  JINTS = 22
     KMESH = 1    KINTS = 1
c
c ------------------------- Translation ------------------------------------
c    x y z
TR1   0  0  0    1 0 0 0 1 0 0 0 1  1     $ Detector/mask
TR2   0.2 0.2 3.175  1 0 0 0 1 0 0 0 1  1      $ Pb Pinhole Collimator
TR3   0.2 0.2 3.175  1 0 0 0 1 0 0 0 1  1      $ Pb pinholes
```

TR4   0.2 0.2 11   1 0 0 0 1 0 0 0 1 1 $ Pb triangle
c
c ------------------------ Physics ---
c
mode p
phys:p 100 0 0 0 0
nps 1e8
c
c ------------------------ Materials ---------------------------------------
c
c CZT Detector Material
m1   48000   0.8 $ Natural cadmium
      52000   1.0 $ Natural tellurium
      30000   0.2 $ Natural zinc
c
c Aluminum
m2   13000   1.0 $ Natural aluminum
c
c Carbon fiber (PAN)
m3   1000   -0.0571 $ Natural hydrogen
      6000   -0.6787 $ Natural carbon
      7000   -0.2641 $ Natural nitrogen
c
c Lead
m4   82000   1.0 $ Natural lead
c
c Air
m100   6000   -0.000124 $ Natural carbon
        7000   -0.755268 $ Natural nitrogen
        8000   -0.231781 $ Natural oxygen
      18000   -0.012827 $ Natural argon
c
c ++++++++++++++++++++ Blank Line Follows ++++++++++++++++++++++++++++

Appendix E (File Parser, Background Subtraction and Reconstruction MATLAB Code)

```
% Program to sort the DMatrix data files
% By Phoenix Baldez
clear
clc

% loads raw data
```

```matlab
filenameCSV = '/Users/Imaging/Dropbox/Public/School/Grad/Hecht
Lab/Gamma Spec
Project/Data/DMatrix/2017/121517_PointSourceSpacing/121517_Eu152_4hrs_1
6ph_MD3cm_SM10cm_a1mm_X8mm_-4mmOffset.csv';
% filenameCSV = 'C:\Users\Phoenix\Dropbox\Public\School\Grad\Hecht
Lab\Gamma Spec
Project\Data\DMatrix\2017\011217_UniformIrradiation_Am241\011317_Unifor
mIrradiation_Am241_12hrs_10cm.csv';
data = csvread(filenameCSV, 1, 0); % data is full data matrix
data = data(:,5:6); % only names pixel and channel information

lines = length(data); % number of lines in data file
spectMat = zeros(484,4096); % empty matrix for spectrum data

for i = 1:lines
    j = data(i,1);
    if j == 111 || j == 132 || j == 374 || j == 353 % bad pixels
        k = 1;
        spectMat(j,k) = 0; % setting bad pixels to 0 counts
    elseif j < 485
        k = data(i,2);
        if k == 4095 % this ch on every pixel has a lot of junk so set
to 0
            spectMat(j,k) = 0;
        end
        spectMat(j,k)=spectMat(j,k)+1; % spectrum of every pixel
    end
end

filenameCSV = '121517_Eu152_4hrs_16ph_MD3cm_SM10cm_a1mm_X8mm_-
4mmOffset_spectra.csv';
csvwrite(filenameCSV,spectMat);

%% BG File Subtract
%loads raw BG data
filenameCSVBG = '/Users/Imaging/Dropbox/Public/School/Grad/Hecht
Lab/Gamma Spec
Project/Data/DMatrix/2017/062317_Ba133_NukeLab/BG/062317_BG_NukeLab_1hr
.csv';
BGdata = csvread(filenameCSVBG, 1, 0); % data is full data matrix
BGdata = BGdata(:,5:6); % only names pixel and channel information

BGlines = length(BGdata); % number of lines in data file
BGspectMat = zeros(484,4096); % empty matrix for spectrum data

for i = 1:BGlines
    j = BGdata(i,1);
    if j == 111 || j == 132 || j == 374 || j == 353 % bad pixels
        k = 1;
        BGspectMat(j,k) = 0; % setting bad pixels to 0 counts
    elseif j < 485
        k = BGdata(i,2);
        if k == 4095 % this ch on every pixel has a lot of junk so set
to 0
            BGspectMat(j,k) = 0;
        end
```

```matlab
            BGspectMat(j,k)=BGspectMat(j,k)+1; % spectrum of every pixel
        end
end

% Subtracts every point of BG from every real data point
for i = 1:484
    for j = 1:4096
        spectMat(i,j) = spectMat(i,j)-(BGspectMat(i,j)*4); % THIS *4 IS
VERY IMPORTANT, TO GET SAME TIME (4hrs run with 1hr BG)
        if spectMat(i,j) < 0
            spectMat(i,j) = 0;
        end
    end
end

%% Peak Find and Trapazoid Subtraction, HeatMap

% 800-900 Am-241
% 1200-1300 Co-57/Eu-152
% 700-800 Eu-152
% 950-1050 Ba-133
maxMat = zeros(1,484); % array of all max ch #s
val = zeros(1,484); % the value of max
pos = zeros(1,484); % the position of max
chStart = 1200; % start of peak finding channel
chStop = 1300; % end of peak finding channel
sumCount = zeros(1,484); % sum of counts in the peak in pixel #
pixelCount = zeros(22); % 22x22 representation of the detector
BGdif = 20; % number of channels above/below the peak value to count/
*THIS SHOULD STAY 20, Full Width Base
BGavgNum = 50; % The number of channels used to calc the avg of BG on
either side

for i = 1:484
    [val,pos] = max(spectMat(i,chStart:chStop)); % value and position of
the maximums from each pixel
%    maxMat(i) = pos; % fills array of max ch #s
    pos = pos+chStart; % add back the start ch value, +800
    lowLim = pos-BGdif; % lower limit of peak find ASSUMING 40ch total
base width
    upLim = pos+BGdif; % upper limit of peak find
    sumCount = sum(spectMat(i,lowLim:upLim)); % sum all counts between
lower and upper limit

    lowBGLow = lowLim-BGavgNum; % low limit that low avg will be calced
from
    lowBGHigh = lowLim; % high limit that low avg will be calced from
    highBGHigh = upLim+BGavgNum; % high limit that high avg will be
calced from
    highBGLow = upLim; % low limit that high avg will be calced from

    BGbase = BGdif*2; % width of base of trapazoid
    lowBG = mean(spectMat(i,lowBGLow:lowBGHigh)); % y1
    highBG = mean(spectMat(i,highBGLow:highBGHigh)); % y2
```

```matlab
    trapazoid = .5*BGbase*(lowBG+highBG); % area of trapazoid to
subtract

    pixelCount(i) = sumCount - trapazoid; % subtracting the trapazoid
    if pixelCount(i) < 0
        pixelCount(i) = 0;
    end

end

pixelCount = rot90(pixelCount,3); % rotates the matrix 270 degrees so
that it is properly oriented
pixelCount = fliplr(pixelCount); % flips for proper orientation

% Excel file to produce heatmap
% OUTPUT to the samae location as this program is located NOT to the
.csv location
filenameCSV = '121517_Eu152_4hrs_16ph_MD3cm_SM10cm_a1mm_X8mm_-
4mmOffset_heatmap.csv';
csvwrite(filenameCSV,pixelCount);

% filenameXLS = 'C:\Users\Phoenix\Dropbox\Public\School\Grad\Hecht
Lab\Gamma Spec
Project\Data\DMatrix\120116_Thin\120116_64th_Co57_SC5cm_CD5cm_30min_max
Mat.xls';
% xlswrite(filenameXLS,maxMat)

%% Simple HeatMap

% 800-900 Am-241
% 1200-1300 Co-57
% 950-1050 Ba-133
chStart = 950; % start of peak finding channel
chStop = 1050; % end of peak finding channel
val = zeros(1,484);
pos = zeros(1,484);
sumCount = zeros(22);

for i = 1:484
    sumCount(i) = sum(spectMat(i,chStart:chStop)); % sum all counts
between lower and upper limit
end

pixelCount = rot90(sumCount,3); % rotates the matrix 270 degrees so
that it is properly oriented
pixelCount = fliplr(pixelCount); % flips for proper orientation

filenameCSVheatmap =
'10112017_PinholeOptimization_Co57_30min_CD6_CS10_heatmap.csv';
csvwrite(filenameCSVheatmap, pixelCount);


%% Image Reconstruction
```

168

```matlab
imageMap = zeros(500);
dividerMap = zeros(500);
pixelDim = 10;
mappingStepSizeX = 43;
mappingStepSizeY = 43;


for q = 1:4
    for p = 1:4
        for i = 1:22
            for j = 1:22
                value = pixelCount(i,j);
                for k = 1: pixelDim
                    for l = 1: pixelDim
                        m = pixelDim * (i-1)+(k)+(p-
1)*mappingStepSizeX;
                        n = pixelDim * (j-1)+(l)+(q-
1)*mappingStepSizeY;
                        mm = m;
                        nn = n;
                        imageMap(m,n) = imageMap(m,n) + value;
                        if value > 0
                            dividerMap(mm,nn) = dividerMap(mm,nn) + 1;
                        end


                    end
                end
            end
        end
    end
end

filenameCSV = '121517_Eu152_4hrs_16ph_MD3cm_SM10cm_a1mm_X8mm_-
4mmOffset_ImageMap.csv';
csvwrite(filenameCSV, imageMap);


map = HeatMap(imageMap, 'Colormap', redbluecmap(64));
% map2 = HeatMap(dividerMap, 'Colormap', redbluecmap(64));


averageMap = imageMap./dividerMap;

% map3 = HeatMap(averageMap, 'Colormap', redbluecmap(64));
%
% singleImage = zeros(mappingStepSizeX+10);
% for r = 1:mappingStepSizeX
%     for s = 1: mappingStepSizeY
%         t = 3*mappingStepSizeX+r;
%         u = 3*mappingStepSizeY+s; % 3 refers to the number of pinholes
minus one
%         singleImage(r,s) = averageMap(t,u);
%     end
% end
%
% filenameCSV = '121517_Eu152_4hrs_16ph_MD3cm_SM10cm_a1mm_X8mm_-
6mmOffset_SingleImageMap.csv';
% csvwrite(filenameCSV, singleImage);
%
```

```
% HM = HeatMap(singleImage, 'Colormap', redbluecmap(64));
```

```
% HM = HeatMap(singleImage, 'Colormap', redbluecmap(64));
```